To the Graduate Council:

I am submitting herewith a thesis written by David F. French entitled " Assessment of a Continuous Air Monitor for the Detection of Airborne Transuranics." I have examined the final copy of this thesis for form and content and recommend that it be accepted in partial fulfillment of the requirements for the degree of Master of Science, with a major in Nuclear Engineering.

Lawrence F Miller

Lawrence Miller, Major Professor

We have read this thesis

and recommend its acceptance:

Accepted for the Council:

Associate Vice Chancellor and

Dean of The Graduate School

ASSESSMENT OF A CONTINUOUS AIR MONITOR FOR THE DETECTION OF AIRBORNE TRANSURANICS

A Thesis
Presented for the
Master of Science
Degree
The University of Tennessee, Knoxville

David F. French
May 1995

DEDICATION

This thesis is dedicated to my parents

Mr. Johnny Franklin French

and

Mrs. Irene Aesque French.

ACKNOWLEDGMENTS

I would like to thank the faculty of the department of Nuclear Engineering for providing me with the opportunity to receive my Masters degree from their department. Thanks to my thesis committee Dr L. Miller , Dr. P. Groer, Dr. D. Simpson.

I would also like to thank the Instrumentation and Controls Division of Oak Ridge National Laboratory for their financial support of this work. Thanks to Ron Roseberry and Bill Bryan of the Instrumentation and Controls Division for their strong support.

Thanks to Bill Sutphin for a better understanding of designing C programs.

The greatest debt, however, is owed to Lorinda Seymore. Her continuous support and encouragement brought this moment to fruition.

ABSTRACT

A study was performed to evaluate current algorithms used for detecting airborne transuranics in a continuous air monitor sampler and to develop an original algorithm that offers an improvement over the existing algorithms. When radon progeny decay they emit α particles that interfere with the detection of α particles from airborne transuranics.

The algorithms designed for detection of airborne transuranics predict the number of counts due to radon daughter α particles and subtract this from the counts in the spectrum. Canberra Nuclear Instruments' ASM 1000 continuous air monitor was used for collecting data in this study, and the algorithm used by the ASM 1000 to detect airborne transuranics was simulated. Contamination was simulated for twelve transuranics (^{232}Th, ^{238}U, ^{235}U, ^{234}U, ^{237}Np, ^{242}Pu, ^{239}Pu, ^{243}Am, ^{232}U, ^{228}Th, ^{241}Am, and ^{238}Pu) and added to the radon daughter α particle spectrum collected by the ASM 1000.

The approach to detection of radioactive aerosols developed in this study models the radon progeny α particle spectrum as a superposition of gamma functions. When the spectrum was modeled with gamma functions, significant increases in instrument sensitivity were realized. A number of counts equal to a concentration equivalent to 8 derived air concentration (DAC) units of each transuranic was added to 131 radon progeny α particle spectra collected by the ASM 1000. The algorithm currently used in the instrument underestimates these counts by an average of 26% for ^{235}U to an average of 89% for ^{232}Th. The algorithm that describes the spectrum as a superposition of gamma functions underestimated these counts by an average of 13% for ^{232}Th to an average of 25% for ^{241}Am.

Additionally, the method employed by the ASM 1000 to determine the lower limit of detection inflated the lower limit of detection and decreased the alarm sensitivity of the instrument. However, statistical measures for the lower limit of detection in the algorithm developed in this study improved the alarm sensitivity over that currently employed by the instrument.

This study also addresses the factors that influence α particle detection in continuous air monitor samplers. These factors include radon reduction screens, filter medium, source to detector distance, and relative size of source and detector.

TABLE OF CONTENTS

CHAPTER		PAGE
1.	INTRODUCTION	1
1.1.	Techniques for Detection of Radioactive Aerosols	3
1.2.	Goals of the Project	6
1.3.	Organization of Thesis	7
2.	DESCRIPTION OF EQUIPMENT	9
2.1.	Overview of ASM 1000	9
2.2.	Description of Detector	11
2.3.	Operation of Instrument	13
3.	ALPHA PARTICLE DETECTION	16
3.1.	Radon Interference	16
3.2.	Unattached Particles	20
3.3.	Radon Reduction Screen	20
3.4.	Filter Medium	21
3.5.	Effect of Source to Detector Distance	24
3.6.	Effect of Relative Size of Source And Detector	25
4.	METHODS OF ANALYSIS	27
4.1.	Determination of Each Radionuclide's Spectrum	29
4.2.	Calculation of Working Levels	32
4.3.	Current Background Estimation Algorithms	38
4.4.	Representation of Spectrum As A Superpositoin of Gamma Funcitons	58
4.5.	Statistics Used to Evaluate Chronic Release	73
5.	RESULTS AND DISCUSSION	75
5.1.	Results of Working Level Determination	75
5.2.	Results of the Acute Release Algorithm	75

5.3. Results of the Chronic Release Algorithms 78

6. CONCLUSION 98

BILIOGRAPHY 100

APPENDICES 102

VITA 132

LIST OF TABLES

TABLE		PAGE
4.4.1.	Parameter estimation using Table Curve	65
4.4.2.	Parameter estimation using iterative technique	65
5.2.1.	Mean ratio and 99% confidence limits (CL) for each transuranic (acute release)	77
5.3.1.	Residual mean, 95% CI, and standard deviation of the predicted counts for spectra that contain only background counts (Canberra's chronic release algorithm)	85
5.3.2.	Residual mean, 95% CI, and standard deviation of the predicted counts for spectra that contain only background counts (spectra are described by a superposition of gamma functions)	86
5.3.3.	Residual mean, 95% CI, and standard deviation produced by Canberra's chronic release algorithm (concentration = 8 DAC)	89
5.3.4.	Residual mean, 95% CI, and standard deviation produced when the spectra are described as a superposition of gamma functions (concentration = 8 DAC)	90
5.3.5.	Percentage of the actual activity that each chronic release algorithm predicts	91
5.5.6.	Alarms produced by Canberra's algorithm for a concentration equal to 8 DAC	96
5.3.7.	Alarms produced when spectra are described as a superposition of gamma functions for a concentration equal to 8 DAC	97

LIST OF FIGURES

FIGURE		PAGE
2.1.1.	Cross Section of CAM sampler head	10
2.3.1.	Data reduction unit's user interface	14
2.3.2.	Equipment assembly used for data collection	15
3.1.1.	^{222}Rn decay series originating from ^{238}U	16
3.1.2.	^{220}Rn decay series originating from ^{232}Th	17
3.1.3.	Fate of radon progeny	18
3.1.4.	Typical background spectrum produced by the decay of radon daughter products	19
3.4.1.	Exploded view of filter assembly	24
4.1.1.	Simulation of ^{232}Th spectrum using ^{239}Pu spectrum	31
4.3.1.	Regions 1 and 2 used to determine the ratio of the ROI to the ^{212}Bi/^{218}Po peak	40
4.3.2.	Representative background and associated meaningful regions	44
4.3.3.	Fit of exponential tails to each background peak	50
4.3.4.	Residual count distribution in ^{239}Pu ROI following removal of background counts in ROI (Canberra)	51
4.4.1.	Gamma function for different values of c	60
4.4.2.	Gamma function for different values of d	61
4.4.3.	Fit of gamma function to ^{239}Pu spectrum	63
4.4.4.	Fit of gamma function to ^{212}Po peak	66
4.4.5.	Fit of gamma function to ^{214}Po peak	67
4.4.6.	Fit of gamma function to ^{212}Bi/^{218}Po peak	68

4.4.7. Activity distribution in ^{239}Pu ROI following removal of each peak using a gamma function 69

4.4.8. Activity distribution in ^{239}Pu ROI (superposition of gamma functions) 71

5.1.1. Working levels for each chronic release analysis 76

5.3.1. Residual distribution in ^{239}Pu ROI followng application of Canberra's algorithm 80

5.3.2. Residual distribution in ^{239}Pu ROI following application of gamma functions to describe each peak 81

5.3.3. Residual distribution in ^{232}Th ROI following application of Canberra's algorithm 83

5.3.4. Residual distribution in ^{232}Th ROI following application of gamma functions to describe each peak 84

5.3.5. Residual distribution in ^{239}Pu ROI following application of Canberra's algorithm (concentration = 8 DAC of ^{239}Pu)..... 87

5.3.6. Residual distribution in ^{239}Pu ROI following application of algorithm that describes each background peak as a gamma function (concentration = 8 DAC of ^{239}Pu) 88

5.3.7. Critical level (L_c) and exposure produced by Canberra's algorithm (^{239}Pu ROI) 93

5.3.8. Critical level (L_c) and exposure for the chronic release algorithm that describes the spectrum as a superposition of gamma functions (^{239}Pu ROI) 94

1. INTRODUCTION

Air monitoring programs are designed to evaluate workplace air for the presence of radioactive aerosols. Two basic types of air monitoring programs exist, retrospective air monitoring programs and real-time air monitoring programs. Sampling workplace air for long periods of time and then later evaluating the sample in a laboratory constitutes a retrospective air monitoring program. Collecting samples representative of the workplace air and immediately analyzing the sample constitutes a real-time air monitoring program.

Title 10 of the code of federal regulations (CFR), 10 CFR, part 835, requires Department of Energy (DOE) facilities to measure workplace air for airborne radioactive contamination. However, to simply state that a facility has an air monitoring program is inadequate at maintaining exposures as low as reasonably achievable (ALARA). Maintaining exposures ALARA requires justification and documentation of all aspects of the air monitoring program including justification and documentation of the choice between retrospective air monitoring or real-time air monitoring.

Title 10 CFR, part 835, also requires air monitoring in any area where an employee may potentially exceed two percent of the annual limit on intake (ALI). Additionally, the code specifies that air monitoring programs are to measure dose rates for the purpose of controlling radiation exposure, not for assigning internal dose. Passive devices such as thermoluminescent dosimeters or film badges are incapable of such performance and therefore unsuited for this application. Particular site characteristics, including type, quantity, and level of hazardous material present, influence the sensitivity levels attainable with any air monitoring program. Retrospective air monitoring programs achieve levels of sensitivity unmatched by real-time air monitoring programs because of the controlled laboratory environment used

for analyzing the samples. But the capabilities of real-time air monitoring to control internal exposure by quickly detecting radioactive aerosols, when they are present in sufficient quantities, necessitates the use of this type of air monitoring. The consideration of time-to-detection for real-time air monitoring and sensitivity levels of retrospective air monitoring suggests that a combination of the two programs may provide greater overall employee protection than the use of a single type of air monitoring program.

A continuos air monitor (CAM) sampler performs the function of real-time air monitoring by detecting and quantifying radioactive aerosols in workplace air. Currently, CAM samplers that detect α particle radiation at Oak Ridge National Laboratory (ORNL) alarm when the amount of radiation detected exceeds a preset level. This preset level defines a constant level of discrimination and represents the expected counts due to background α particle radiation. Given the fact that the level of background α particle radiation is constantly changing, a constant level of discrimination causes an overall decrease in the average sensitivity of the instrument. However, recent technological advances in CAM sampler technologies are providing methods that enable CAM samplers to estimate the constantly changing background radiation levels. With the ability to estimate the true level of background radiation comes the opportunity to increase instrument sensitivity.

Microprocessor based CAM samplers implement sophisticated algorithms that apportion the detected radiation between naturally occurring background radiation and hazardous radioactive aerosols. These CAM samplers periodically evaluate the collection medium using electronics contained within the CAM head or within associated electronic control units. Ideally, periodic evaluation in these real-time air monitors will contain separate algorithms for acute release situations versus longer

term or chronic release situations. Current designs almost exclusively perform both evaluations while the CAM is still sampling air containing naturally occurring radioactive particulates, and this complicates the analysis algorithm. One purpose of this study is to evaluate the performance of Canberra Nuclear Instruments' microprocessor based CAM sampler for the application in areas potentially containing radioactive aerosols. Another is to provide an alternative algorithm that increases the instrument's capabilities for the detection of radioactive aerosols.

Avoiding and minimizing internal exposures due to inhalation of radioactive material requires a complete knowledge of the control mechanisms in place. Techniques used for workplace monitoring must collect representative samples of ambient air and this requires strategic location of each air monitor. Operators of CAM samplers need a full knowledge of the aerosols sampled, type of radioactive particulates present and an understanding of CAM technologies. Canberra Nuclear Instruments produces the ASM 1000 and this study directly assess this CAM sampler's performance. The goal of this assessment is to provide benchmark results that aide in developing a basic understanding of the performance expected from this CAM sampler.

1.1 Techniques for Detection of Radioactive Aerosols

The basic unit of a CAM sampler consists of an air pump, filter medium, radiation detector and electronic circuitry. The air pump pulls air through the filter medium which is located beneath the radiation detector. The filter medium removes airborne particulates from the air stream as the air passes through the filter medium. The radiation detector monitors for radiation emitted from the particulates collected on the filter medium. The electronic circuitry converts the charge produced by the interaction of radiation with the radiation detector into an electronic signal. If the

CAM sampler detects a level of radiation exceeding acceptable background radiation levels, the CAM sampler initiates an alarm.

The ASM 1000 uses algorithms designed for detection of airborne ^{239}Pu. The instrument stores events resulting from background α particle radiation and ^{239}Pu α particle radiation in a 256 channel multichannel analyzer (MCA). Periodic data analysis applies mathematical algorithms to the collected data to separate the data into two parts, counts due to background α radiation and counts due to ^{239}Pu α radiation. If the counts due to ^{239}Pu radiation are greater than the acceptable levels defined by the CAM sampler operator the instrument initiates an alarm. Otherwise, the instrument discards the data and another analysis cycle begins.

There are at least two major problems in this approach to detection of α particles that originate from hazardous radioactive aerosols. The first is that dust collects on the filter paper and gradually covers the material previously deposited on the filter. Alpha particles emitted by aerosols imbedded in the dust on the filter lose energy as they emerge from beneath the dust. Alpha particles that lose energy as they leave the filter paper contribute a continuum of counts to the spectrum collected by the MCA. This energy straggling of the α particles depends on the amount of dust in the air and on the filter paper.

The second and most fundamental problem to α particle detection is the presence of naturally occurring α emitting radon daughter products in the environment. These background α emitting isotopes originate from the decay of ^{238}U and ^{232}Th into isotopes of radon. Since radon is a gas it readily diffuses through the earth's crust and into the atmosphere. When radon decays it produces daughter products that collect on the filter paper. As these daughter products decay they emit α particles that interfere with detection of other radioactive aerosols. Radon daughter products contribute

higher energy α particles than does ^{239}Pu or any other transuranic in this study. However, energy attenuation of radon daughter α particles contributes a continuum of counts to the channels of the MCA. This continuum of counts extends from the energy channel that corresponds to the α particle energy to the lowest energy channel of the MCA. Since ^{239}Pu α particles are lower in energy than the α particles of radon daughter products, the continuum of counts contributes counts that interfere with the detection of ^{239}Pu.

Presently the instrument employs two algorithms that determine if ^{239}Pu is present. One algorithm simply compares counts in two regions of the MCA. The channels that contain the majority of ^{239}Pu α's define one region and the channels that contain only radon daughter alphas define the other region. Note that one region contains counts due to both ^{239}Pu alphas and radon daughter α particles, due to α particle energy straggling, and that the other region contains only counts due only to radon daughter α particles. This algorithm relies on a consistent characteristic attenuation of radon daughter α particles and develops a ratio of one region to the other. Determination of a positive ^{239}Pu concentration occurs when this ratio becomes larger than expected.

The second algorithm predicts the number of attenuated radon daughter alphas in one region by modeling the attenuation of radon daughter α particles from another region. Again, the channels containing the majority of ^{239}Pu α particles define one region and the channels containing only radon daughter α's define the other region. Modeling the attenuated α particles requires fitting equations to the spectrum produced by the MCA. This spectrum contains varying amounts of each daughter product and the equations describe the attenuation of α particles from each daughter. Determination of a positive ^{239}Pu concentration occurs when the number of attenuated

α counts predicted by the model significantly underestimates the total number of counts in the ^{239}Pu region. Significant underestimation of the counts in the ^{239}Pu region implies that there are more counts in the ^{239}Pu region than can be explained by errors in the model. Thus, the counts remaining are from ^{239}Pu α particles.

This study extends the current algorithms to perform for transuranics with energies different than that of ^{239}Pu. Additionally, this study provides a simulation of the current algorithms using many data sets collected by the CAM sampler. The purpose of simulating the current algorithms is to asses their performance for detecting the presence of ^{239}Pu and other transuranics. This study also provides an alternative technique for predicting radon daughter alphas in the one region based on the radon daughter alphas in another region. This technique models the radon daughter products with a series of gamma functions. Gamma functions deconvolve the spectrum and predict the attenuation of radon daughter α particles. Deconvolving the spectrum and predicting the attenuation of radon daughter α particles allows estimation of the number of α particles present in the spectrum from ^{239}Pu and other transuranics.

1.2 Goals of the Project

Primary objectives of this study are as follows:

1) identify and evaluate affects of instrument configuration on the background spectrum, including the affects of filter materials, radon reduction screen, physical air flow through the instrument and source to detector distance,

2) implement methods for detecting the following 12 transuranics in the presence of naturally occurring background radiation: ^{232}Th, ^{238}U, ^{235}U, ^{234}U, ^{237}Np, ^{242}Pu, ^{239}Pu, ^{243}Am, ^{232}U, ^{228}Th, ^{241}Am, and ^{238}Pu,

3) generate a simulation of actual detector response to each of the 12 transuranics studied, and

4) demonstrate methods for increasing sensitivity to radioactive aerosols using the microprocessor based CAM technologies.

The two techniques that mathematically model the data from the MCA produce significantly different results. Modeling the data with a series of gamma functions produces results that more accurately predict the attenuated radon daughter α particles than do the algorithms designed by Canberra. However, both algorithms demonstrate that sensitivity levels increase by modeling the data as opposed to using a constant level of discrimination.

1.3 Organization of Thesis

To facilitate the understanding of the methods of detecting radioactive aerosols, chapter 2 provides an overview of the ASM 1000. Included in this description of the instrument is a description of the associated electronics used for α particle detection, a physical description of the CAM sampler head, discussion of the solid state detector used for detecting α particle radiation, and instructions on operation of this CAM sampler.

Chapter 3 addresses issues considered in detecting α particle radiation. These issues include naturally occurring interference from radon daughter products and the nature of these radon daughter products. Additionally, physical design issues that influence α particle detection are addressed, including: radon reduction screens, filter medium, source to detector distance, and relative size of source and detector.

A description of the methods used in the analysis follows the discussion on factors influencing α particle detection. This section is chapter 4 and it describes the

methods used to simulate each transuranic and outlines the methods used to quantify each data set. Both the current methods used by Canberra for detecting radioactive aerosols and the method used to describe each data set as a series of gamma functions are presented in this section.

Chapter 5 presents the results and discussion of the analysis. The discussion presents results obtained using both the current Canberra algorithms and the algorithm that describes the spectrum as a series of gamma functions. Statistical comparisons between each algorithm are interpreted and the merit in each technique is examined.

Finally, chapter 6 summarizes the results and conlcusions of the analysis. This chapter also makes recommendations for continued work in the area of detecting airborne transuranics.

2. DESCRIPTION OF EQUIPMENT

2.1 Overview of ASM 1000

Canberra Industries Incorporated manufactures the ASM 1000 and this is the only CAM sampler available for this study. This instrument consists of three electronic subassemblies: a preamplifier board, a multichannel analyzer, and a data reduction unit. The mechanical assemblies consist of a CAM head and an enclosure for the data reduction unit. The CAM head contains the detector, preamplifier board, filter media, radon reduction screen, flow regulator and MCA. Figure 2.1 is a cross section of the CAM head and it illustrates the location of the two electronic subassemblies, all head components and the air flow through the head. A radon reduction screen surrounding the sampling inlet provides physical removal of fresh or unattached radon progeny. Air is drawn into the head through the radon reduction screen and through the filter by way of the air pump connection. The detector is located above the filter paper, and air flows around the passivated implanted planer silicon (PIPS) detector.

The preamplifier board consists of a charge amplifier (preamplifier), a fast peak detector, and pulse shaping electronics. The charge amplifier functions as an integrator that converts charge to voltage. The fast peak detector captures and holds the peak signal resulting from α particles striking the detector. And, the pulse shaping electronics shape the signal into a more Gaussian response than would be seen otherwise.

The MCA board contains a Motorola 68HC11 eight bit microcontroller. The 68HC11 microcontroller runs at 8 MHz and contains an on-chip analog-to-digital converter (ADC) with a resolution of eight bits. The fast peak detector circuitry issues an interrupt to the microcontroller when a peak is detected. This interrupt initiates

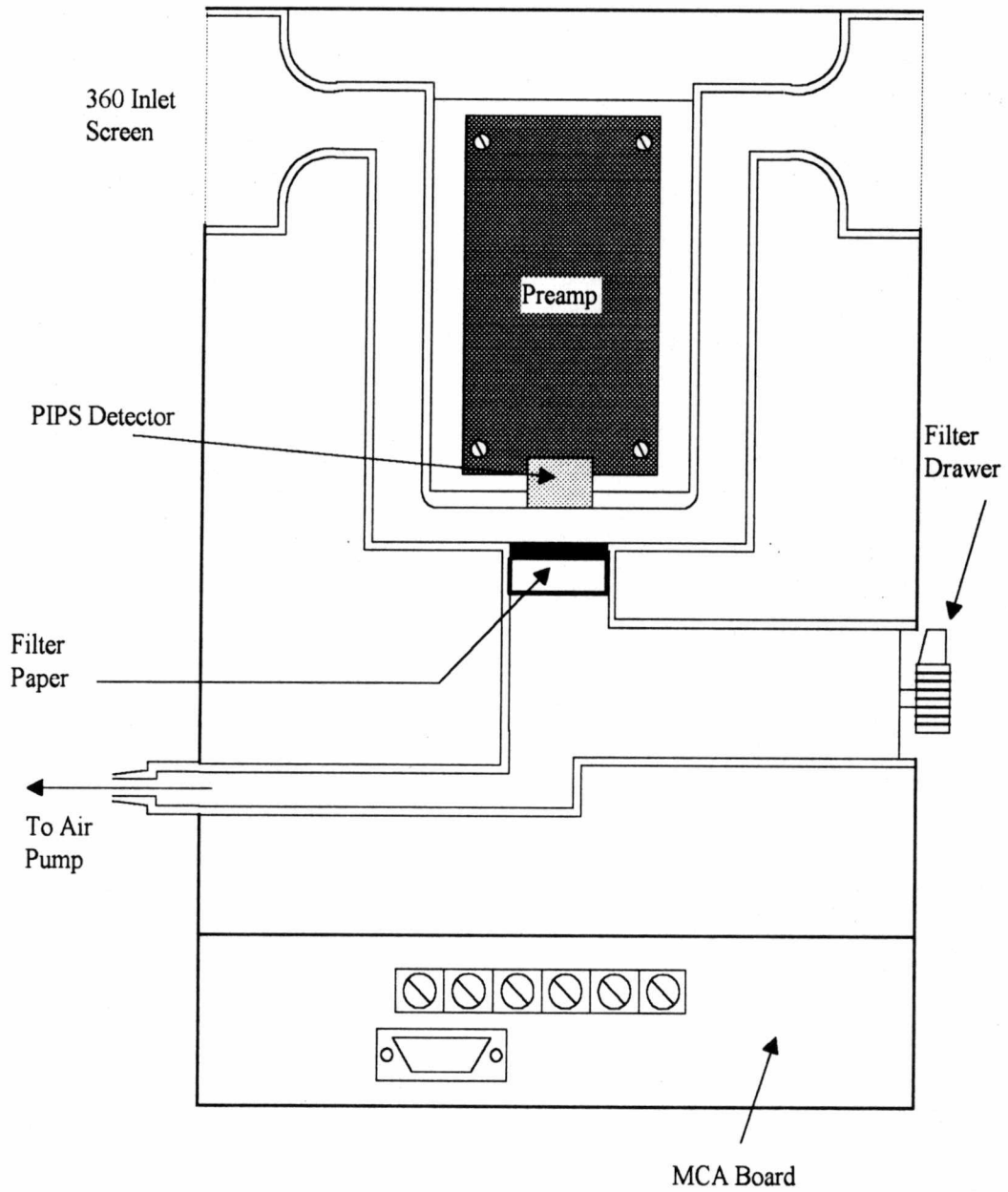


Figure 2.1. Cross section of CAM sampler head. (Adapted from ASM 1000 technical documentation) (Canberra 1992).

an analog-to-digital conversion. Upon completion of the analog-to-digital conversion, the microcontroller stores the results in the MCA and resets the fast peak detector. Resetting the fast peak detector enables detection of the next α particle that strikes the detector.

The 68HC11 contained in the CAM head communicates with the data reduction assembly through a serial port according to the RS-485 protocol (Canberra 1994). This configuration allows the control of up to thirty-two heads from a single host computer. The data reduction unit contains a second 68HC11 microcontroller, memory, operator interface and all necessary software to perform the data analysis and initiate an alarm.

2.2 Description of Detector

The detector is a 1700 mm^2 passivated implanted planer silicon (PIPS) detector manufactured by Canberra Industries, Inc.. Fabrication techniques for producing these detectors are proprietary, but the process of producing passivated silicon detectors is widely understood. Passivated detectors originate from oxidized silicon. When silicon oxidizes, a layer SiO_2 forms on the surface of the silicon. This silicon is usually n+ type material (donor material) (Knoll 1989). Photographic processes selectively remove areas of the oxide and determine the location of the entrance windows. Accelerating acceptor ions such as boron or phosphorous and targeting these ions at the entrance windows produces p-n junctions. Planting these acceptor ions within each window forms p+ material and results in a p-n junction. The energy of the incident ions dictates the concentration profile. As one would expect, this process does produce a significant amount of radiation damage, but an annealing process alleviates radiation induced damages. The annealing temperature is considerably lower than the thermal diffusion

of the dopants (Knoll 1989). Additional photographic processing leaves a thin layer of aluminum on the detector's front and rear surfaces producing the ohmic contacts required for signal collection.

When a voltage is applied to the two aluminum contacts such that the junction is reversed biased, a depletion region forms and a small current (less than 10^{-6} amperes) flows. The depletion region simply describes the region of the detector over which a charge imbalance exits, and this depletion region increases with increasing voltage. In traditional silicon surface barrier (SSB) detectors the junction extends to the edge of the wafer and large leakage currents flow. Contrary with the SSB detectors the oxide passivated surface of the PIPS detectors maintain very high electrical resistivity that aides in reducing leakage currents.

When radiation strikes the detector it imparts some or all of its energy into the depletion region and produces electron-hole pairs inside the depletion region. The applied voltage produces an electric field that sweeps the electrons out of the depletion region and into the associated electronic circuitry. Charge sensitive electronic circuitry collects the charge produced by the flow of electrons and produces a voltage pulse that is proprotional to the collected charge.

Use of the PIPS detector for α particle detection provides the following benefits over traditional SSB detectors:

1) buried junction edges,

2) ion-implanted contacts that form thin abrupt junctions,

3) a rugged entrance window - easily cleaned with mild solvents,

4) leakage currents that are one to two orders of magnitude less than that of traditional SSB detectors and

5) a dead layer that is less than that of most surface barrier detectors (Canberra 1994).

One major benefit of the buried junction edges in the PIPS detector is that the device stability is not dependent on epoxy sealant which is used in many other solid state detectors (Canberra 1994). Another is that leakage currents remain small in comparison to that of traditional SSB detectors and diffused junction (DJ) detectors. With the decrease in leakage currents, electronic noise is reduced improving the signal-to-noise ratio in the electronics.

Thin entrance windows provide greater α particle energy resolution over that of traditional SSB or of DJ detectors. As a result PIPS detectors obtain better energy resolution than typical SSB or DJ detectors. Passivated implanted planer silicon detectors have entrance windows on the order of 500 angstrom, compared to entrance windows from 800 to 2000 angstrom for typical surface barrier detectors (Canberra 1994). At close source to detector distances, alpha particles that strike the detector at an acute angle will lose a greater amount of energy in the entrance window than the alpha particles that enter perpendicular to the window. Dead layer losses result in peak broadening and reduce the resolution of the instrument. Therefore, an entrance window that is as thin as possible is desired to improve instrument resolution.

2.3 Operation of Instrument

The user interface of the data reduction unit contains a keypad with soft-touch keys for entering parameters and for navigating through system information. It contains a liquid crystal display (LCD) capable of displaying spectrum data and analysis results. Figure 2.3.1 represents the data reduction unit's user interface. The user

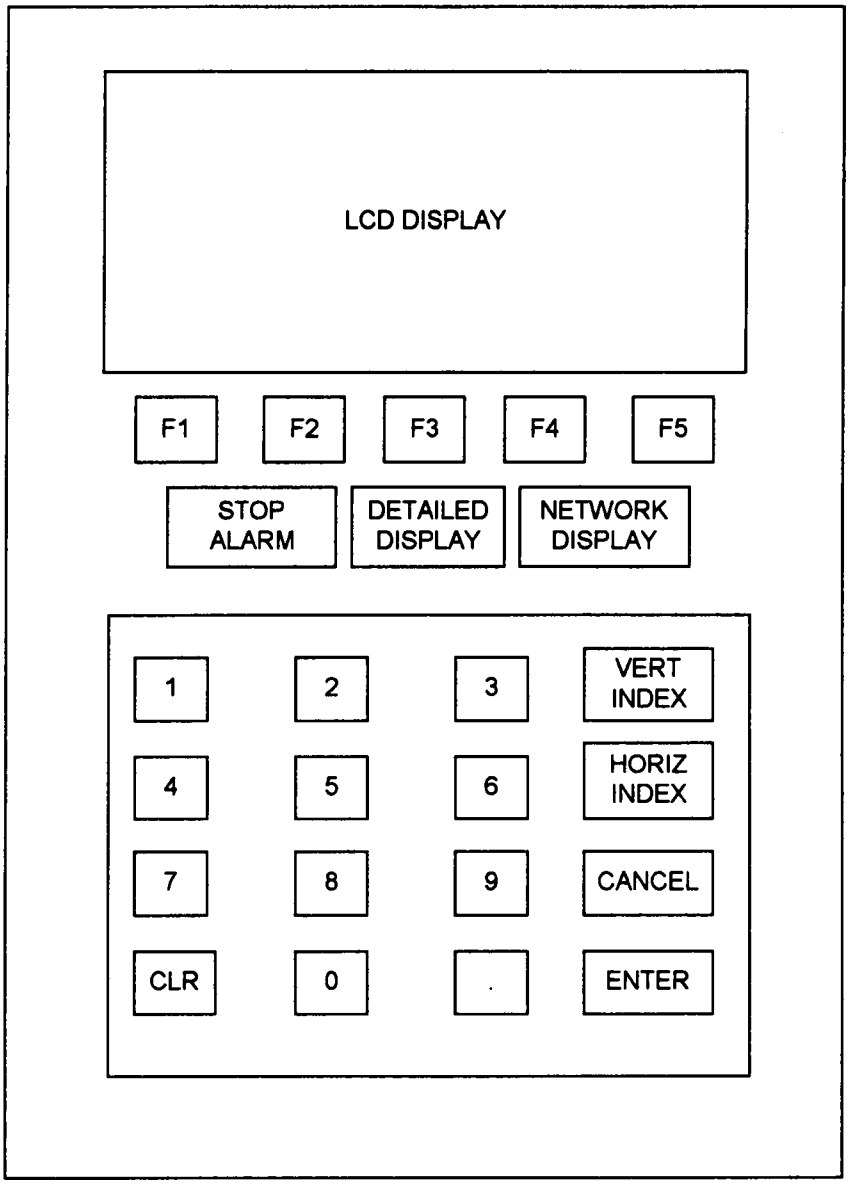


Figure 2.3.1. Data reduction unit's user interface.

interface allows the operator to view current CAM sampler data including exposure, concentration, CPM, alarm status, efficiency, calibration date and alarm status. All information is available for each CAM sampler of the network. Accessing and storing system information is available through serial port communication with a personal computer. Figure 2.3.2 illustrates the setup used to collect data from the CAM head. It is possible to perform all system operation from a single computer without the data reduction unit, however protocol and source code for such a setup is currently unavailable.

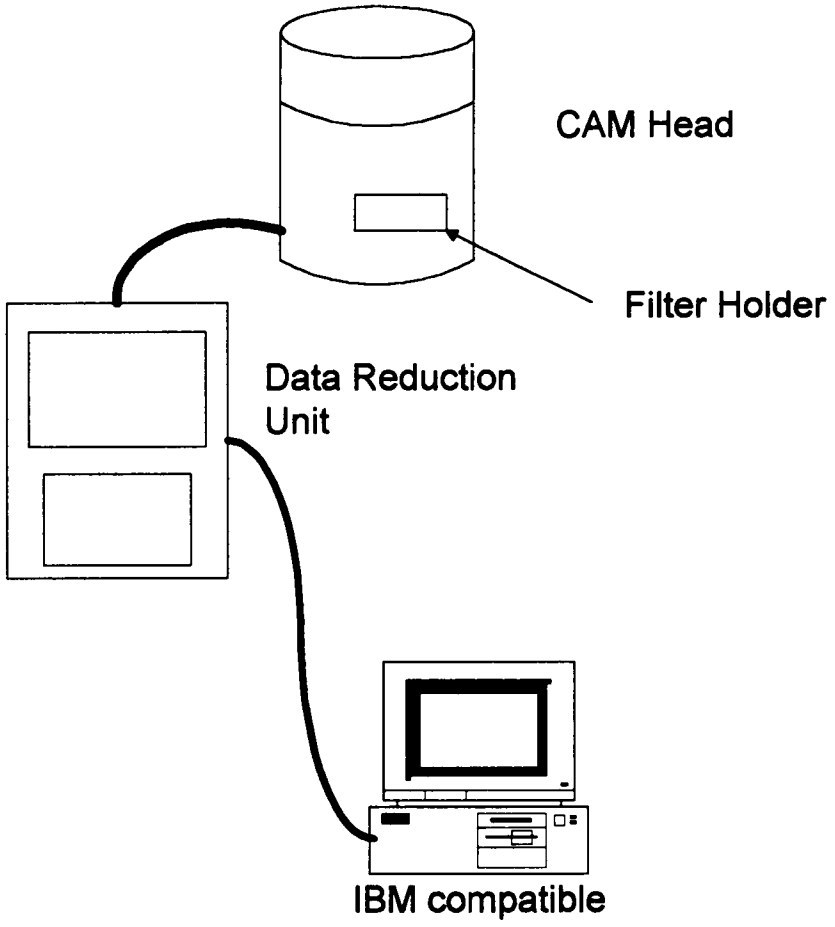


Figure 2.3.2. Equipment assembly used for data collection.

3. ALPHA PARTICLE DETECTION

3.1 Radon Interference

The ^{238}U decay chain results in the production of ^{222}Rn, which is the immediate decay product of ^{226}Ra and is the heaviest member of the noble gas family. Radon exits as a gas at ordinary ambient temperature and diffuses into the atmosphere through soils and fractured rock. Fry (1976) estimates the average outdoor concentration of radon as 0.1pCi/L. Figure 3.1.1 illustrates the ^{222}Rn decay series that originates from ^{238}U.

$$^{222}Rn \xrightarrow{5.49\,MeV\,\alpha} {}^{218}Po \xrightarrow{6.0\,MeV\,\alpha} {}^{214}Pb \xrightarrow{0.73\,MeV\,\beta} {}^{214}Bi \rightarrow$$
$$\xrightarrow{1.51\,MeV\,\beta} {}^{214}Po \xrightarrow{7.69\,MeV\,\alpha} {}^{210}Pb$$

Figure 3.1.1. ^{222}Rn decay series originating from ^{238}U.

During operation of the CAM, these radon daughters interfere with detection of transuranics. However, the energy resolution of the CAM permits differentiation among ^{218}Po (6.00 MeV), ^{214}Po (7.68 MeV) and ^{212}Po (8.77 MeV) with the 1700 mm^2 PIPS detector. Note that ^{212}Po is part of the ^{232}Th decay series, which is illustrated by Fig. 3.1.2

The fate of each radon daughter product in an indoor environment includes inhalation, ventilation, and surface plate out. Inhalation involves the removal of radon daughter products from the atmosphere by individuals in the immediate vicinity of the

decay products. Through the act of breathing, radon daughters deposit in the lung of the individual. Ventilation, usually caused by a heating, ventilation, or air conditioning

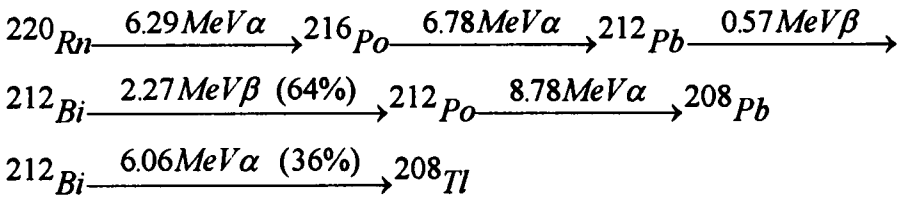


Figure 3.1.2. ^{220}Rn decay series originating from ^{232}Th.

(HVAC) system, removes radon daughters from the immediate environment. But just as ventilation removes radon daughters from the immediate environment, it also brings radon daughters into the immediate environment. Still another possible fate for radon daughter products is that they will become attached to a surface and no longer be airborne; however these particles can emerge from their surface due to the recoil action when the daughter product emits an α particle. Fig. 3.1.3 is a graphical representation of the possible fate of each radon progeny

Figure 3.1.4 illustrates a typical background caused by the decay of radon daughter products. The figure shows the spectral location of each background isotope and the α particle energy straggling. There are two α particles that contribute to the peak around 6.0 MeV. The decay of ^{212}Bi (6.06 MeV) contributes one α particle and the decay of ^{218}Po (6.0 MeV) contributes the other.

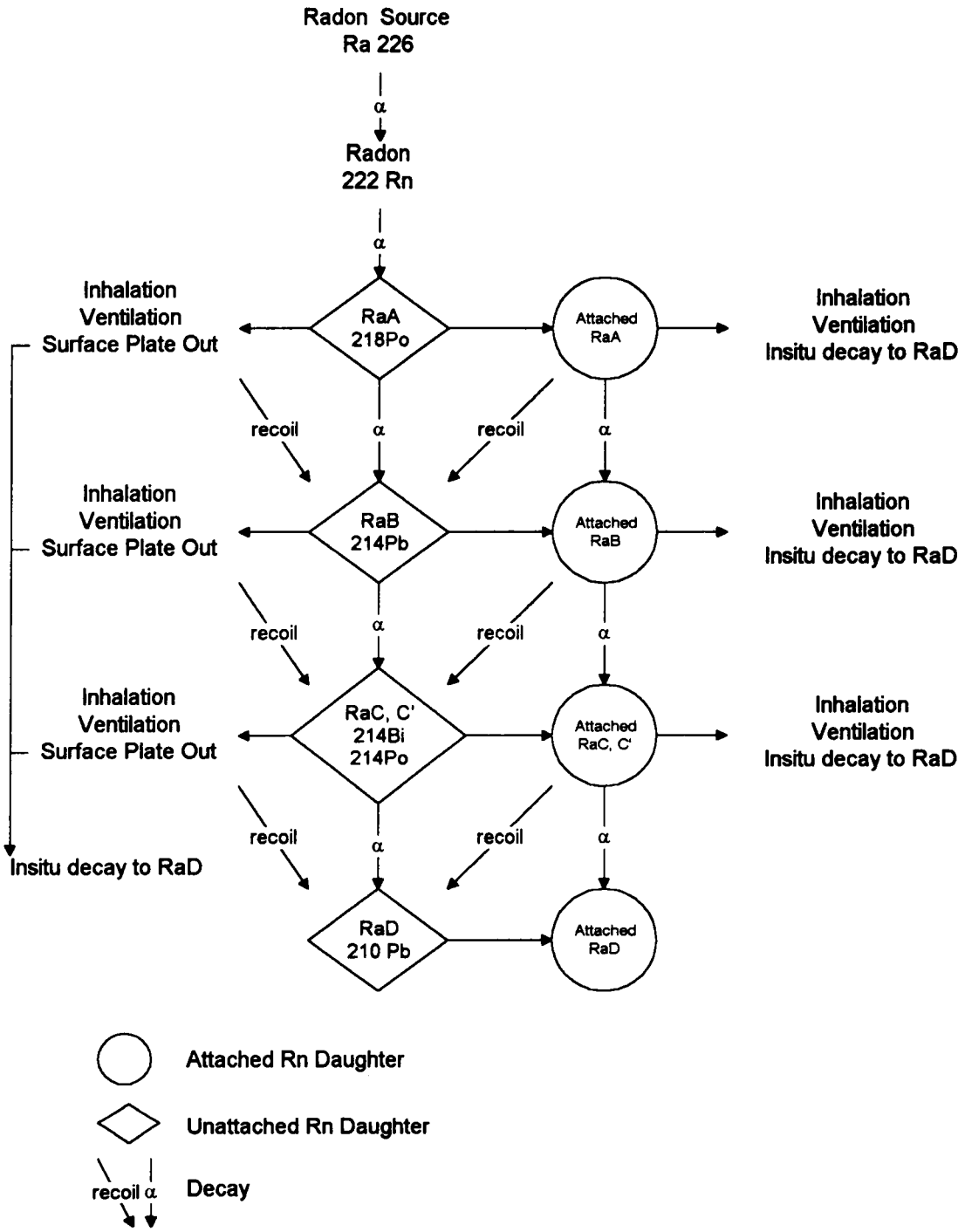


Figure 3.1.3. Fate of radon progeny (Adapted from Busigin 1981).

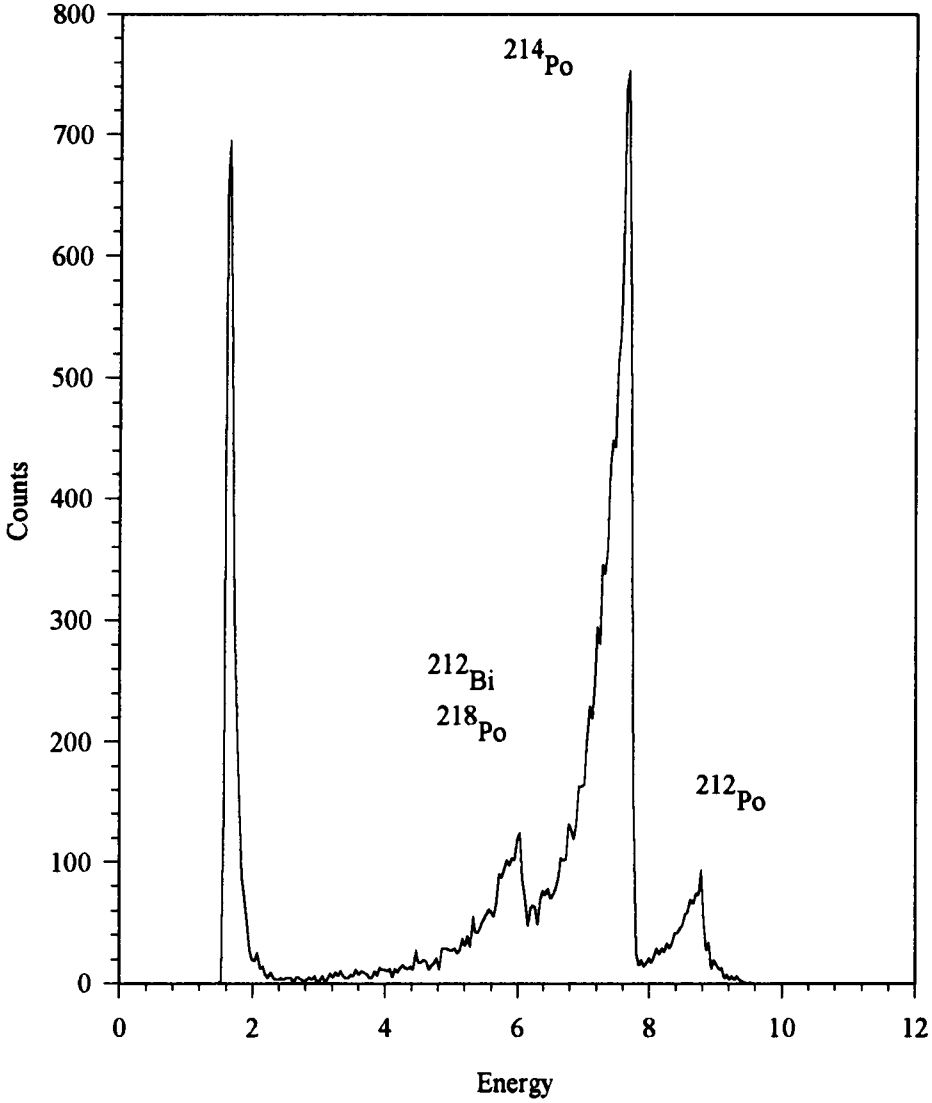


Figure 3.1.4. Typical background spectrum produced by the decay of radon daughter products.

3.2 Unattached Particles

Radon daughters that are not attached to ambient aerosols are widely referred to as either free ions or unattached radon daughters (Reineking 1990). Stripping of orbital electrons leaves unattached RaA positively charged and results from either a departing α particle or the recoil motion of the atom upon emission of an α particle. Radium A (^{218}Po), B (^{214}Pb) and C (^{214}Bi) are in a highly excited state at birth and react quickly with oxygen or trace gases such as sulphur dioxide and sulphur trioxide (Busigin 1981). Investigations into the true nature of these unattached particles is minimal, but Busigin (1981) suggests that these particles may not be of a single chemical species. The diffusion coefficient of radon in air at room temperature is estimated to be about 0.1cm^2 sec^{-1} (Busigin 1981). However, Raabe (1969) determined that the diffusion coefficient of RaA decreased with increasing humidity. Although a limited understanding of the nature of unattached radon daughters exist, this information is not very useful. An understanding of the quantity of unattached radon progeny is of direct benefit. The difficulty arises in attempting to estimate the unattached fraction of radon progeny in an operating environment. Published data for the unattached fraction of radon progeny range from 0.49 to less than 0.01 for ^{218}Po, from 0.067 to less than 0.01 for ^{214}Pb and from 0.032 to less than 0.01 for ^{214}Po (Reineking 1990). However, recently published calculations suggest an unattached fraction for all radon daughters of 0.03 for indoor environments (ICRP 1987; NEA 1983).

3.3 Radon Reduction Screen

Radon reduction screens are designed to physically remove unattached radon progeny through coulombic interactions. If the effectiveness of the screen is known

and if an accurate estimate of the unattached fraction exists, uncertainties in the measurement are easily calculated. The radon reduction screen surrounding the sampling inlet physically removes fresh radon progeny from the sampling stream. As the positively charged daughter products attempt to pass through the screen, coulombic interactions cause the particles to attach to the screen. The screen is 60 mesh (60 wires per inch) with a wire diameter of 191 μm and this screen is optimized for flow rates from 28 to 57 L/min. McFarland (1992) indicates that the radon reduction screen is effective in removing greater than 90% of unattached radon progeny.

Alternately, penetration of attached radon daughters through the mesh screen is high and is estimated to be greater than 80% (McFarland 1992). The coulombic forces that affect unattached radon progeny have little affect on attached particles. Due to the large size of the particles, the mesh screen permits penetration of both attached radon progeny and airborne transuranic material.

Both removal efficiency and concentration of the unattached fraction influence the effectiveness of the radon reduction screen. The overall reduction in background contribution to the spectrum is the product of the efficiency of the radon reduction screen and the unattached fraction. If one assumes 90% percent effectiveness for removing unattached particles and an unattached fraction of 3%, the overall benefit of using the radon reduction screen is a 2.7% reduction in total detected background.

3.4 Filter Medium

CAM samplers use many types of filter medium and these include fibrous and membrane filters. The filter surface serves as the primary plane for deposition of airborne particles. The most efficient filters for maintaining deposition on the surface

(while minimizing the interference caused by allowing particles to become embedded beneath the surface) are membrane filters. Fibrous filters (such as cellulose filters) offer a greater opportunity for interference with the emitted alpha particles than do the membrane filters. These filters allow deep penetration into the fiber matrix and ultimately increase the probability of obstructing an alpha particle's path before detection.

Several characteristics are useful for classifying the performance of the filter material. These include: typical flow rate, FWHM (full width at half max) of ^{218}Po peak, relative radon progeny counts in the Pu region of interest (ROI), and relative radon progeny collection efficiency. Choice of the filter material and of its characteristics depends on the desired flow rate through the filter. Since flow rate is usually controlled by the CAM, use of a filter material that produces a high flow impedance is not recommended.

Hoover and Newton (1993) performed a series of tests to evaluate the performance of various commercially available filters which were carried out using a proportional counter. They demonstrated that the full-width at half max of the ^{218}Po peak associated with the 3μm pore size Fluoropore filter produced by Millipore Corporation is less than any other cellulose or membrane filter in their study. The 3 μm pore size Fluoropore filter exhibited less relative radon progeny counts in the ^{239}Pu ROI than any other filters evaluated in their study. However, this filter exhibits an undesireably high radon progeny collection efficiency which results in the collection of most of the interfering radon progeny. Ideally, a filter medium would allow the passage of the small particles that are more likely to contain radon progeny and collect only the large particles that are more likely to contain contamination.

A cellulose fiber filter manufactured by Whatman Labsales exhibited the worst performance of any filter in Hoover and Newton's study (Hoover 1993). Measurements performed with this filter indicate an average ^{218}Po FWHM of greater than 1500 keV which indicates extreme α particle interference.

Pore size is the specification of choice and ranges from 0.6μm to 5μm. Hoover and Newton (1993) state that the typical FWHM for the 3 μm pore size Fluoropore filter is 350 keV. Conversely, the cellulose filters studied under the same conditions all exhibited FWHM values ranging from 520 to greater than 1500 keV. This wide range of FWHM's reveals that the cellulose filters interfere with the emerging α particles more than membrane filters do. Spectra collected using the cellulose filters showed more relative radon progeny counts in the ^{239}Pu ROI than did spectra collected using the membrane filters. Of the two types of filters, the membrane filters produce the least spectral energy degradation . However, the superior resolution of the membrane filters does come at a price. The 3μm pore size filter is 2 to 20 times more expensive than other available filters for CAM samplers.

Millipore Corporation manufactures the Fluoropore 5 μm filter used for this study. The surface area of the filter is 17,349 mm^2 and an exploded view of the filter and filter assembly is illustrated in Fig. 3.4.1. Typical full-width at half max of the ^{218}Po peak obtained during operation was 360 keV. Recognizing that the energy resolution of the on board MCA is 39 keV per channel, an estimation of the true FWHM is accurate to about 80%. The ^{218}Po FWHM is between 321 keV and 399 keV. Hoover and Newton (1993) obtained a typical FWHM for ^{218}Po of 460 keV using a gas proportional counter and the 5μm pore size filter. Even with the error bounds on the FWHM, the resolution of the PIPS detector is still better than those achieved with the gas proportional counter. Results indicate that energy resolution

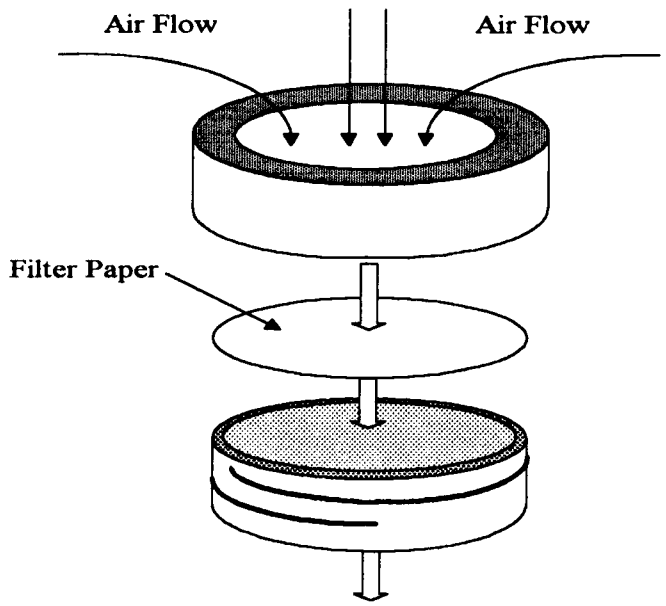


Figure 3.4.1. Exploded view of filter assembly.

with the 5 μm pore size filter and the PIPS detector is nearly identical to results Hoover and Newton obtained using the 3 μm pore size filter and a gas proportional counter.

3.5 Effect of Source to Detector Distance

Due to the charge and size of the α particles, attenuation increases rapidly as source to detector distance increases. The geometrical configuration of a planer filter and planer detector attenuates many alpha particles before they reach the detector which leads to dispersions on the low energy side of the emission (Moore 1992). Thus, it is necessary to use as small a source to detector distance as possible. However, if the source to detector distance is too small, the gap spacing interferes with air flow and impedes collection of alpha emitting aerosols which implies that a tradeoff exists between flow rate and efficiency.

A wide source to detector distance decreases energy straggling by collimating the α particle path. Collimation occurs since more alpha particles strike the detector normal to the entrance window. Disadvantages to wide source to detector spacing include a broadening effect on the FWHM and α peak shifting in the spectrum due to energy losses in the gap. Moore (1992) demonstrated, using a 450 mm^2 PIPS detector, that as the source to detector gap increases from 3.2 mm to 6.2 mm, the detector efficiency decreases from approximately 0.31 cpm/dpm to 0.23 cpm/dpm. Moore also demonstrated that the resolution (FWHM) of the detector increased from 260 keV to 320 keV for this same increase in gap distance.

3.6 Effect of Relative Size of Source and Detector

Relative size of the filter media and detector impacts the performance of the CAM. Moore (1992) demonstrated that efficiency drops from 0.25 to 0.10 as the source diameter increases from 24 mm diameter to 44 mm diameter with a 24 mm diameter PIPS detector and a 5 mm source-to-detector gap. Under these same conditions efficiency using a 47 mm PIPS detector falls from 0.35 to 0.30. Additionally, the FWHM using the 47 mm diameter PIPS detector remains nearly constant while the FWHM using the 24 mm diameter PIPS detector increases greater than 10%. Since the lower limit of detection is largely a function of efficiency, maintaining a source diameter that is less than or equal to the detector diameter increases the CAM's sensitivity over other geometrical configurations.

Considering the factors that influence the quantification of radon in the atmosphere, the designer of a CAM is faced with a formidable challenge in optimizing the system for detection of alpha particles. In a particular operating environment, it would be beneficial to estimate the true fraction of unattached radon progeny.

However, for an instrument intended to operate in the majority of indoor environments, the extensive testing necessary to determine the unattached radon progeny for every case is prohibitive. In the event that several environmental operating conditions were evaluated, it is difficult to correctly interpret how the algorithms employed in the instrument should handle this information. The use of physical removal mechanisms such as radon reduction screens is promising, but currently, the net benefit from these devices seems minimal. Filter medium and source to detector distance have the greatest impact on alpha particle detection efficiency. Use of the best filter medium , correct relative size of filter paper and source diameter (along with a source to detector distance that optimizes the flow rate through the instrument) impacts the collection of meaningful spectrum data as much or more than any variable in the CAM sampler design. Designing the instrument to maximize the benefit from each factor influencing the detection of airborne transuranics increases the ability of the CAM to discriminate against background. Since the limiting factor on detection is efficiency, every effort should be employed in the device to maximize this critical parameter.

4. METHODS OF ANALYSIS

This chapter contains detailed descriptions of three algorithms used for detecting airborne transuranics. Each of these algorithms detects airborne transuranics by accurately predicting the counts in the spectrum due to radon daughter α particles. Canberra designed two of the algorithms, one for a chronic release of radioactive aerosols and one for an acute release of radioactive aerosols. The third algorithm is an original approach to detecting a chronic release of radioactive aerosols.

The technical documentation supplied with the ASM 1000 outlines both of Canberra's algorithms, but it fails to define all parameters used by each algorithm. Since the documentation is incomplete, several parameters are approximated based on the points in the spectrum that each parameter represents. Section 4.3 describes, in detail, each of Canberra's algorithms along with the assumptions required to simulate these algorithms.

The original approach used in this analysis predicts counts in the spectrum due to radon daughter α particles based on the height and width of each radon daughter peak (^{212}Po, ^{214}Po, and ^{212}Bi/^{218}Po). This technique of predicting counts due to radon daughter α particles uses a series of gamma functions to model the natural appearance of the spectrum. By modeling each peak with a gamma function, each spectrum is considered to consist of a superposition of gamma functions. Section 4.4 describes, in detail, how gamma functions accurately predict the number of counts in the spectrum due to radon daughter α particles.

The analysis of the three algorithms uses two sets of data collected by the ASM 1000 CAM sampler. Since the counts in each spectrum of the data sets are due only to the decay of radon daughter products, these spectra are often referred to as

background spectra. One data set contains 131 spectra, that were each collected for one hour, and the other contains 600 spectra that were each collected for six minutes. Both chronic release algorithms are simulated using the set of 131 background spectra and the acute release algorithm is simulated the set of 600 background spectra.

Spectral data that describe the activity distribution of each transuranic are not available. Therefore, this study assumes each transuranic is correctly represented by modifying the CAM sampler's response to a single isotope. Since the only radioactive source available that would fit in the filter holder of the CAM sampler was a disk source of ^{239}Pu, its activity distribution is used to model the activity distribution of the eleven other transuranics studied. Section 4.1 provides both the details of implementing this technique and the estimation of the errors produced by this technique.

The final assumption used in this analysis is that the radon concentration in the atmosphere is in equilibrium. To estimate the working level in the analysis, radon and radon progeny are assumed to be in equilibrium. This assumption simplifies the set of differential equations describing the relative concentration of each radon daughter into a series of algebraic equations.

The programs that perform the simulation of each algorithm were written in C language and compiled under Borland C++ 4.0. Each program executes under a standard DOS environment and processes the entire data set for each of the twelve transuranics. Each program generates an output file that contains the counts predicted by the algorithm for each transuranic's ROI and the actual counts in each transuranic's ROI. In addition to predicted and actual counts in each ROI, the programs designed to simulate Canberra's algorithms also generate statistical measures of uncertainty using the methods outlined in the ASM 1000 technical documentation.

4.1 Determination of Each Radionuclide's Spectrum

Each radionuclide's spectrum and subsequent ROI is based on detector response to ^{239}Pu. Detector response to a ^{239}Pu source (activity = 1800 disintegrations per minute) located in the CAM sampler filter holder forms the bases for each radionuclide's spectrum. By moving the location of the 5.16 MeV ^{239}Pu peak along with its activity distribution to the corresponding peak energy of the radionuclide of interest, each radionuclide's activity distribution is simulated. This is accomplished in the computer code by placing the activity distribution of ^{239}Pu, based on location of the peak (5.16 MeV), in the area of the radionuclide of interest based on the location of the radionuclide's peak energy. Simply, each spectrum is simulated by shifting the activity distribution of ^{239}Pu to correspond to the area containing the radionuclide of interest based on the location of the peak energies. Figure 4.1.1 illustrates how this technique of shifting the ^{239}Pu spectrum simulates a ^{232}Th spectrum. Each channel in the ^{239}Pu spectrum is shifted downward twenty-nine channels (twenty-nine channels is the difference between the peak energies of the two isotopes divided by the channel width = $\frac{5.16MeV - 4.01MeV}{.0392MeV}$). In this manner each isotope of interest is simulated from the single ^{239}Pu spectrum. In order to obtain different quantities of activity the counts in each channel are multiplied by an appropriate scaling factor.

Approximating each isotope from a single ^{239}Pu spectrum produces minimal errors. Neglecting the difference in stopping powers in air between 5.16 MeV α particles and 4.01 MeV α particles assumes that each particle losses energy in air at the same rate and that the effects of air attenuation are the same for both particles. Since air attenuation is essentially negligible, a ^{239}Pu spectrum should accurately model a true spectrum produced from 4.01 MeV ^{232}Th α particles. The difference in resolution

in the spectrum produced by a 5.16 MeV α particle and a 4.01 MeV α particle is the difference between the number of charge carriers produced in the silicon. Typical silicon used in solid state detectors produces approximately one electron-hole pair for each 3 eV deposited in the silicon detector. Using this factor, the mean number of charge carriers for a 5.16 MeV α particle (^{239}Pu) is 1.72×10^6 and the mean number of charge carriers for a 4.01 MeV α particle (^{232}Th) is 1.33×10^6. Since the mean number of charge carriers dictates the resolution of the detector, due to statistical fluctuations in the Poisson process, detector resolution is (Knoll 1989)

$$R = \frac{FWHM}{H_O} = \frac{2.35}{\sqrt{n}}, \tag{4.1.1}$$

where

$FWHM$ = full width at half max of the peak height,

H_O = average pulse amplitude,

R = resolution, and

n = mean number of charge carriers.

Using the definition for detector resolution, $R_{5.16}$ represents the resolution for 5.16 MeV α particles and $R_{4.01}$ represents the resolution for 4.01 MeV α particles. Based on the approximation for the number of charge carries for both energies, $R_{5.16} = 1.79 \times 10^{-3}$ and $R_{4.01} = 2.04 \times 10^{-3}$. The difference in resolution between $R_{5.16}$ and $R_{4.01}$ is fourteen percent. From Fig. 4.1.1, the FWHM of a ^{239}Pu spectrum is 360 keV and a fourteen percent degradation in the FWHM of this spectrum is 50 keV. Simulating the ^{232}Th spectrum from a ^{239}Pu spectrum underestimates the true FWHM of a ^{232}Th spectrum by 50 keV. But, the difference is insignificant since the resolution of the detector is 256 channels of 39 keV each. The maximum variability produced using this method to approximate each isotope's spectrum is 2 channels or less, because the

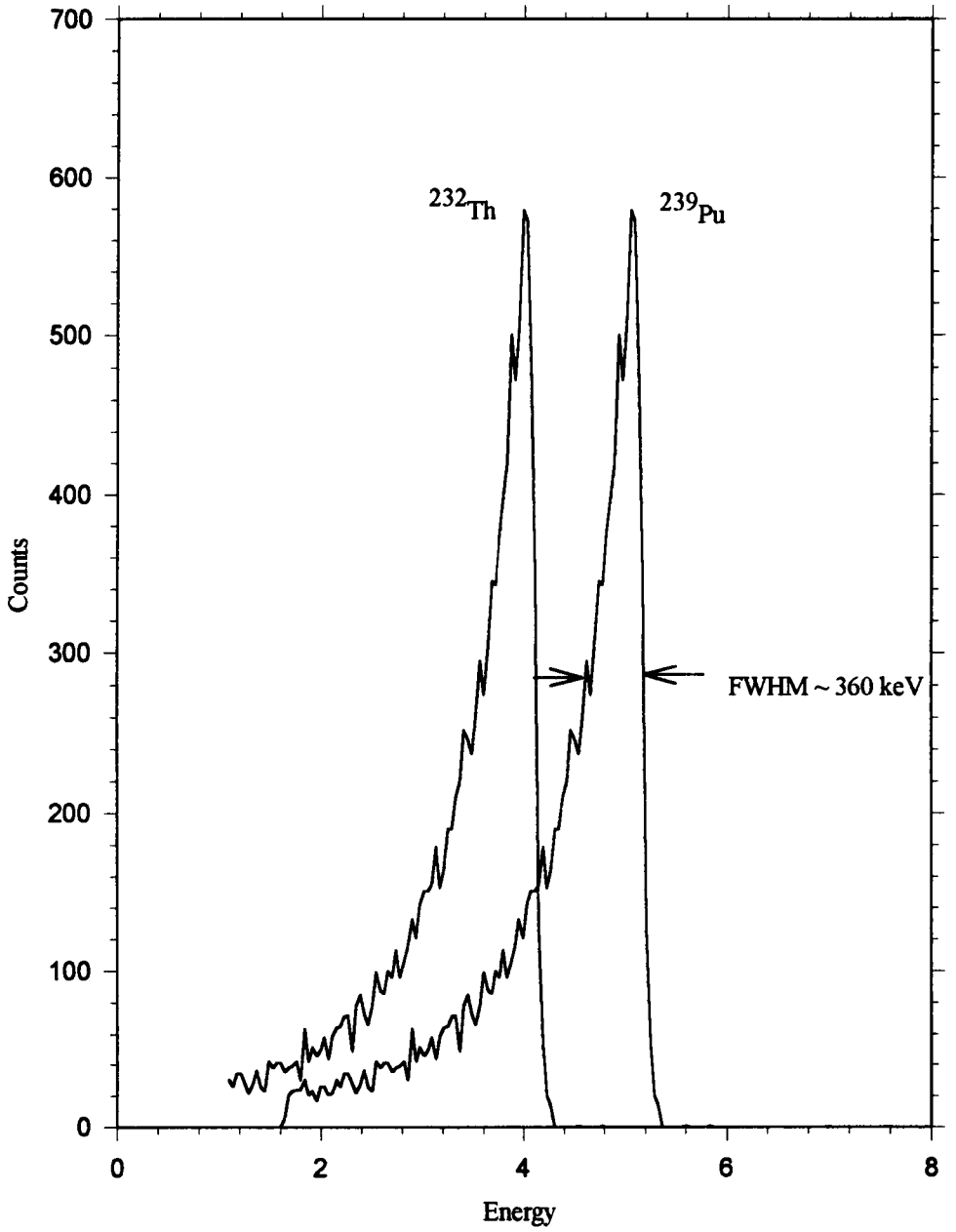


Figure 4.1.1. Simulation of ^{232}Th spectrum using ^{239}Pu spectrum.

energy difference between ^{232}Th α particles and ^{239}Pu α particles is greater than the energy difference between ^{239}Pu α particles and the α particles of any other isotope in this study.

4.2 Calculation of Working Levels

A working level is defined as

> *" any combination of short-lived radon daughters in one liter of air that will result in the ultimate emission of 1.3 x 10^5 MeV of potential alpha particle energy"* (Shleien 1986).

Working levels are dependent on the ventilation rate (age of air) and on radon concentration (Kawaji 1980). Each radon daughter contributes to the working level. For this reason, the concentration of radon is usually assumed to be in equilibrium. Equilibrium implies that the age of the air, and hence the age of ^{222}Rn, is constant and does not change over the course of the analysis. Equilibrium does not imply that the concentration of ^{222}Rn is constant, but instead that the age of the air containing ^{222}Rn is unchanging. In an atmosphere where the age of the air varies, ^{222}Rn and its progeny are present in different quantities and the assumption of equilibrium is invalid. Since each progeny contributes to the working level it is necessary to know the concentration of each progeny over the entire analysis period in order to calculate the working level. Dynamics of a fluctuating radon concentration require complex system modeling which is beyond the scope of this study. However, by assuming that the ^{222}Rn concentration is in equilibrium, each progeny is present in proportional quantities based on the total α, β or α + β activity in the atmosphere.

A CAM sampler is relatively insensitive to a changing radon concentration because the filter medium is affected in the same manner as the local atmosphere in the

presence of a changing radon concentration. As long as the radon concentration is in equilibrium the activity of each radon daughter on the filter medium varies directly with the atmospheric concentration of radon daughter products. Therefore, the total α, β or $\alpha + \beta$ activity collected during an analysis period is a direct measure of the working level during the analysis period.

The buildup and collection of radon and radon daughter atoms on the filter medium is described by

$$\frac{dN_i}{dt} = Q_i V + \lambda_{i-1} N_{i-1} - \lambda_i N_i, \qquad (4.2.1)$$

where

N_i = number of atoms of member i of the radon decay series,

Q_i = concentration of member i (atoms/liter),

V = flow rate (liters/min),

i = 1 for ^{222}Rn, 2 for ^{218}P0, 3 for ^{214}Pb ,4 for ^{214}Bi,

λ_i = decay constant of element i of the decay series, and

λ_0 and $N_0 = 0$.

The activity of any member of the ^{238}U decay series (Fig. 3.1.1) is described as

$$\frac{dA_i}{dt} = \lambda_{i-1} A_{i-1} - \lambda_i A_i, \qquad (4.2.2)$$

where A = activity

i = 1 for ^{222}Rn, 2 for ^{218}Po, 3 for ^{214}Pb ,4 for ^{214}Bi,

λ_i = decay constant of element i of the decay series,and

λ_0 and $A_0 = 0$.

Integrating Eq. 4.2.2 yields the activity of each member of the decay series at any time t and is given by,

$$A_2 = \frac{\lambda_1 A_1}{\lambda_2}(1 - e^{-\lambda_2 t}), \tag{4.2.3}$$

$$A_3 = \frac{\lambda_1 A_1}{\lambda_3}(1 - e^{-\lambda_3 t}) + \frac{\lambda_1 A_1}{\lambda_3 - \lambda_2}(e^{-\lambda_3 t} - e^{\lambda_2 t}), \tag{4.2.4}$$

$$\begin{aligned} A_4 = {} & \frac{\lambda_1 A_1}{\lambda_4}(1 - e^{-\lambda_4 t}) + \frac{\lambda_4 A_1}{\lambda_4 - \lambda_3}(e^{-\lambda_4 t} - e^{-\lambda_3 t}) \\ & + \frac{\lambda_1 \lambda_3 A_1}{(\lambda_3 - \lambda_2)(\lambda_4 - \lambda_3)}(e^{-\lambda_3 t} - e^{-\lambda_4 t}) \\ & + \frac{\lambda_1 \lambda_3 A_1}{(\lambda_3 - \lambda_2)(\lambda_4 - \lambda_2)}(e^{-\lambda_4 t} - e^{-\lambda_2 t}) \end{aligned} \tag{4.2.5}$$

where A_2, A_3 and A_4 are the activities of ^{218}Po, ^{214}Pb and ^{214}Bi, respectively. The atmospheric concentration of each daughter is described in the same manner that activity is in Eq. 4.2.2. That is, the concentration of any daughter is described as

$$\frac{dQ_i}{dt} = \lambda_{i-1} Q_{i-1} - \lambda_i Q_i. \tag{4.2.6}$$

The change in radon progeny concentration on the filter paper during an analysis period depends on the length of an analysis period and on the rate of change of the atmospheric radon concentration during the analysis period. If the atmospheric radon concentration varies only slightly during an analysis period the change in radon concentration can be considered negligible. To apply this assumption correctly it is necessary to design sampling periods based on the rate of change in atmospheric radon concentration such that the change in radon concentration during the analysis period is small. There are no exact guidelines for how much change in the concentration is tolerable and the experimentalist exercises judgment that determines the sampling period.

Experiments in this study were designed without consideration to the change in radon concentration during the analysis period, however, to solve Eq. 4.2.6, it is necessary to assume that the radon concentration is unchanging. For a constant radon concentration, integrating Eq. 4.2.6 yields the concentration of each daughter at any time t as

$$Q_2 = \frac{\lambda_1 Q_1}{\lambda_2}(1 - e^{-\lambda_2 t}), \tag{4.2.7}$$

$$Q_3 = \frac{\lambda_1 Q_1}{\lambda_3}(1 - e^{-\lambda_3 t}) + \frac{\lambda_1 Q_1}{\lambda_3 - \lambda_2}(e^{-\lambda_3 t} - e^{\lambda_2 t}) \tag{4.2.8}$$

and

$$\begin{aligned} Q_4 = {} & \frac{\lambda_1 Q_1}{\lambda_4}(1 - e^{-\lambda_4 t}) + \frac{\lambda_4 Q_1}{\lambda_4 - \lambda_3}(e^{-\lambda_4 t} - e^{-\lambda_3 t}) \\ & + \frac{\lambda_1 \lambda_3 Q_1}{(\lambda_3 - \lambda_2)(\lambda_4 - \lambda_3)}(e^{-\lambda_3 t} - e^{-\lambda_4 t}) \\ & + \frac{\lambda_1 \lambda_3 Q_1}{(\lambda_3 - \lambda_2)(\lambda_4 - \lambda_2)}(e^{-\lambda_4 t} - e^{-\lambda_2 t}) \end{aligned}, \tag{4.2.9}$$

where Q_2, Q_3 and Q_4 of ^{218}Po, ^{214}Pb and ^{214}Bi, respectively.

For steady state in the air and on the filter, Eq. 4.2.1 simplifies to $\frac{dN_1}{dt} = 0$. Eq. 4.2.1 becomes

$$\lambda_i N_i = Q_i V + \lambda_{i-1} N_{i-1} \tag{4.2.10}$$

for the steady state condition. For the steady state atmospheric condition the activities of radon daughters on the filter paper from Eq. 4.2.10 becomes

$$C_2 = \lambda_2 N_2 = Q_2 V, \tag{4.2.11}$$

$$C_3 = \lambda_3 N_3 = Q_3 V + \lambda_2 N_2 = (Q_2 + Q_3)V \qquad (4.2.12)$$

and

$$C_4 = \lambda_4 N_4 = Q_4 V + \lambda_3 N_3 = (Q_2 + Q_3 + Q_4)V. \qquad (4.2.13)$$

.

Being a gas ^{222}Rn does not collect on the filter paper. Therefore, the term describing ^{222}Rn ($\lambda_0 N_0$) is neglected by Eq. 4.2.11.

Kawaji (1980) defines the ratios of α *activity*, β *actvity* and $\alpha+\beta$ *activity* to the working level concentration (WL) and demonstrates that the

$\frac{\alpha \text{ activity}}{WL}$, $\frac{\beta \text{ activity}}{WL}$ and $\frac{(\alpha+\beta) \text{ activity}}{WL}$ ratios are independent of the radon concentration but dependent on the in-growth time. Using this method, it is possible to derive the working level from the integrated α, β, or α+β activity. All that is necessary is determination of a conversion factor based on sampling time, detector efficiency, volume of air through the filter and the $\frac{\alpha \text{ activity}}{WL}$, $\frac{\beta \text{ activity}}{WL}$ or $\frac{(\alpha+\beta) \text{ activity}}{WL}$ ratio. If the α+β counts are used it is necessary to have equal counting efficiencies for both particles. For this reason, this analysis uses α activity to evaluate the working level.

Total α activity is $C_2 + C_4$. This assumption groups the β^- decay of ^{214}Bi (RaC) to ^{214}Po (RaC') and the α decay of ^{214}Po to ^{210}Pb (RaD) as one event - the total activity contributed by the third radon daughter. Since the half-life of ^{214}Po is 163.7μs, while that of ^{214}Bi is 19.9 minutes, this assumption is valid. Therefore, from Eqs. 4.2.11 and 4.2.13 the total α activity is given by

$$A_\alpha = (2Q_2 + Q_3 + Q_4)V. \qquad (4.2.14)$$

After approximately five half-lives, of the longest lived daughter (134 min.), ^{214}Pb, the concentration of radon daughters on the filter paper is in equilibrium. At this point or as $t \rightarrow \infty$ substitution of Eqs. 4.2.7, 4.2.8 and 4.2.9 into Eq. 4.2.14 reveals the total α activity of the radon daughters as a time independent algebraic expression. This concentration of radon daughter α activity on the filter medium is

$$\alpha \ activity = Q_1 V\left(2\frac{\lambda_1}{\lambda_2}+\frac{\lambda_1}{\lambda_3}+\frac{\lambda_1}{\lambda_4}\right). \tag{4.2.16}$$

With the working level defined as

$$WL=\frac{13.68Q_2+7.68(Q_3+Q_4)}{130{,}000}, \tag{4.2.17}$$

it is possible to solve for the working level in the same manner as the α activity (Kawaji 1980). After five half- lives of ^{214}Pb, the working level becomes a time independent expression. Substituting the concentration of each radon daughter (Eqs. 4.2.7, 4.2.8 and 4.2.9) into Eq. 4.2.17 reveals the working level as

$$WL=Q_1\left(13.68\frac{\lambda_1}{\lambda_2}+7.68\left(\frac{\lambda_1}{\lambda_3}+\frac{\lambda_1}{\lambda_4}\right)\right)\frac{1}{130{,}000}. \tag{4.2.18}$$

The $\frac{\alpha \ \ actvity}{WL}$ ratio defined by dividing Eq. 4.2.16 by Eq. 4.2.18 reveals that the $\frac{\alpha \ \ actvity}{WL}$ ratio is independent of the radon concentration but instead dependent on the detector efficiency and sampling rate. The ratio becomes

$$\frac{\alpha \ \ actvity}{WL} = 17146*V. \tag{4.2.19}$$

To determine the WL for each analysis period it is necessary to account for α particle detection efficiency of the detector. The term *α activity* of Eqs. 4.2.16 and 4.2.19 is the α counts in the spectrum corrected for detector efficiency. Accounting for detector efficiency results in an expression that calculates the WL based on α counts collected by the CAM sampler. Taking into account the flow rate through the CAM sampler along with detector efficiency results in the following expression for calculating the WL,

$$WL = (\alpha \text{ counts})/(17146*\text{efficiency}*V). \qquad (4.2.20)$$

The α counts in Eq. 4.2.20 are the sum of the total counts in the spectrum from 2.5 MeV to 7.68 MeV. Below approximately 2.5 MeV there are counts due to high energy β particles from the decay of ^{214}Bi ,which is part of the ^{238}U decay series (Fig. 3.1.1) and from the decay of ^{212}Bi, which is part of the ^{232}Th decay series (Fig. 3.1.2). Above 7.68 MeV there are counts contributed by the ^{232}Th decay series. These counts are due to an 8.78 MeV α particle originating from the decay of ^{212}Po to ^{208}Pb. The counts between 2.5 MeV and 7.68 MeV are the counts necessary to calculate the WL and are described by the activity Eqs. 4.2.3, 4.2.4, and 4.2.5.

4.3 Current Background Estimation Algorithms

Canberra employs two algorithms that determine the presence of radioactive aerosols. Although Canberra designed the algorithms for detection of ^{239}Pu, the application of each algorithm in this study references the ROI as the transuranic ROI. The first algorithm applies a count ratio technique and is the bases for the acute release determination. This algorithm separates the spectrum into two regions, the transuranic ROI and the ^{212}Bi/^{218}Po ROI. By comparing the counts in the transuranic ROI to the

counts in the $^{212}Bi/^{218}Po$ ROI, the algorithm determines the presence of the transuranic. The second algorithm models the counts in the transuranic ROI by describing the attenuated radon progeny α particles as a set of exponential equations and is the bases for the chronic release determination. Counting statistics dictate the necessity for two detection algorithms.

During short time intervals, (less than 5 min.), the channels of the MCA contain fewer counts than are necessary to accurately describe the background spectrum. To accurately describe the background spectrum, each radon daughter must contribute a sufficient number of counts to develop an identifiable peak (Fig. 3.1.2). The curve fitting algorithm fails when the spectrum contains fewer counts than are necessary to describe each radon daughter peak. Therefore, the count ratio technique is probably the best alternative method to detect the presence of radioactive aerosols in low background situations. When the spectrum develops a distinct peak that describes each radon daughter product, as in Fig. 3.1.2, the mathematical representation of the attenuated α particles provides more accurate predictions to the counts in the transuranic ROI than the count ratio technique.

Possible settings for a chronic release count cycle range from five minutes to sixteen hours with a default value of thirty minutes. The acute release setting is thirty seconds and is not changeable. These preset time intervals represent typical count times for the two alarms. However, the atmospheric concentration of radon daughter products dictates whether or not the default settings are adequate.

Figure 4.3.1 illustrates the two regions used in determining the count ratio and is the ratio of the counts in region 1 to the counts in region 2. Region 1 is the ROI for each isotope and region 2 extends from the end of the ROI to the top of the

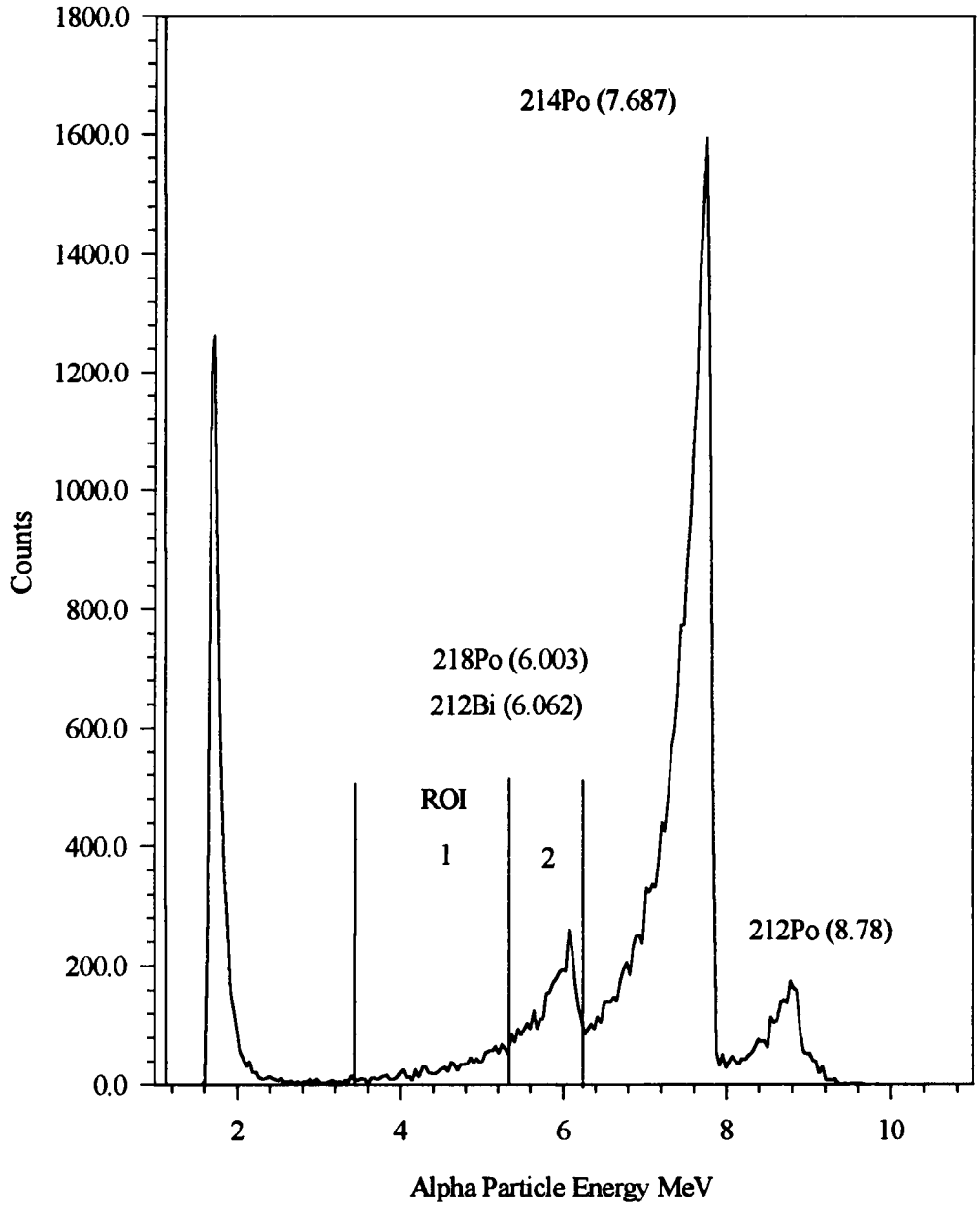


Figure 4.3.1. Regions 1 and 2 used to determine the ratio of the ROI to the $^{218}Po/^{212}Bi$ peak.

$^{218}Po/^{212}Bi$ peak. The data for determining the count ratio are 600 six minute counts and 131 one hour counts. The six minute counts were taken consecutively for a period spanning 3.5 days. The one hour counts were collected from two count cycles, one spans 60 hours and the other spans 71 hours. Results from the application of this technique are based on a mean ratio and confidence interval (CI) for each ROI. Each confidence interval is calculated from the formula

$$C.I. = \bar{x} \pm 2.58\frac{s}{\sqrt{n}}, \qquad (4.3.1)$$

where

s = the sample standard deviation,

n = the sample size, and

$\bar{x}$ = the sample mean.

Upon power up or after a filter change, the instrument defaults to a present energy calibration. Before each chronic release determination the instrument performs an energy calibration to determine if a peak shift has occurred. Since energy calibration is based on the location of the 7.68 MeV ^{214}Po peak, the location of this peak determines if a peak shift has occurred. The location of this peak is determined by searching 5 channels above and 10 channels below the expected location of the peak. Determination of the location of the ^{214}Po peak is as follows:

1) The instrument sums the counts in a three channel region containing channel 169 as the center channel (channel 169 is the default channel for an energy of 7.68 MeV).

2) The instrument moves the center channel of the three channel region one channel and then sums the counts in this center channel, one channel above and

one channel below. This process continues for 10 channels below channel 169 and 5 channels above channel 169.

3) The three-channel region with the most counts is considered to contain the peak channel if the sum is 10 counts or more greater than the default three channel region.

Peak shifts are usually the result of dust loading of the filter. Energy calibration of the MCA takes the form $y = .0392x + b$, where y is the energy in MeV, and x is the channel number. The default setting for b is 1.055, which occurs when the ^{214}Po peak is at channel number 169. Energy calibration proceeds as follows:

1) the instrument sums the counts in a three channel region composed of the location of the ^{214}Po peak from the previous count cycle and the two channels adjacent to this peak,

2) the instrument sums the counts in the three channel region composed of one channel down from the location of the ^{214}Po peak and the two channels adjacent to it,

3) this iterative process continues above and below the current location of the ^{214}Po peak,

4) if a three channel region contains 10 more counts than the region currently assumed to contain the ^{214}Po peak, the peak is considered to have shifted.

The new location of the ^{214}Po peak is the center channel of this three channel region. If the location of the ^{214}Po peak is different than the previous calibration, the instrument performs an energy calibration before applying the chronic release algorithm.

The instrument defines several meaningful points in the spectrum for the purpose of determining a chronic or acute release. Figure 4.3.2 identifies the meaningful regions for the analysis. These regions include:

1) X_0, the beginning of the meaningful spectrum,

2) X_1, the valley channel between the transuranic ROI and the $^{218}Po/^{212}Bi$ peak,

3) X_2, the valley channel between the $^{218}Po/^{212}Bi$ peak and the ^{214}Po peak,

4) X_3, the valley channel between the ^{214}Po peak and the ^{212}Po peak,

5) X_4, the end of the spectrum, channel 255.

These points, or channel numbers, divide the spectrum into five meaningful regions :

1) region 0, the area below the beginning of the meaningful spectrum,

2) region 1, the area between X_0 and X_1 defining the plutonium region of interest,

3) region 2, the area between X_1 and X_2, which includes the $^{218}Po/^{212}Bi$ peak,

4) region 3, the area between X_2 and X_3, which includes the ^{214}Po peak,

5) region 4, the area between X_3 and X_4, which includes the ^{212}Po peak.

Additionally, the following points are defined:

1) Y_0 as the counts at point X_0,

2) Y_1 as the counts at point X_1,

3) Y_2 as the counts at point X_2,

4) Y_3 as the counts at point X_3.

The technical manual fails to identify the exact locations of X_1, X_2 and X_3.

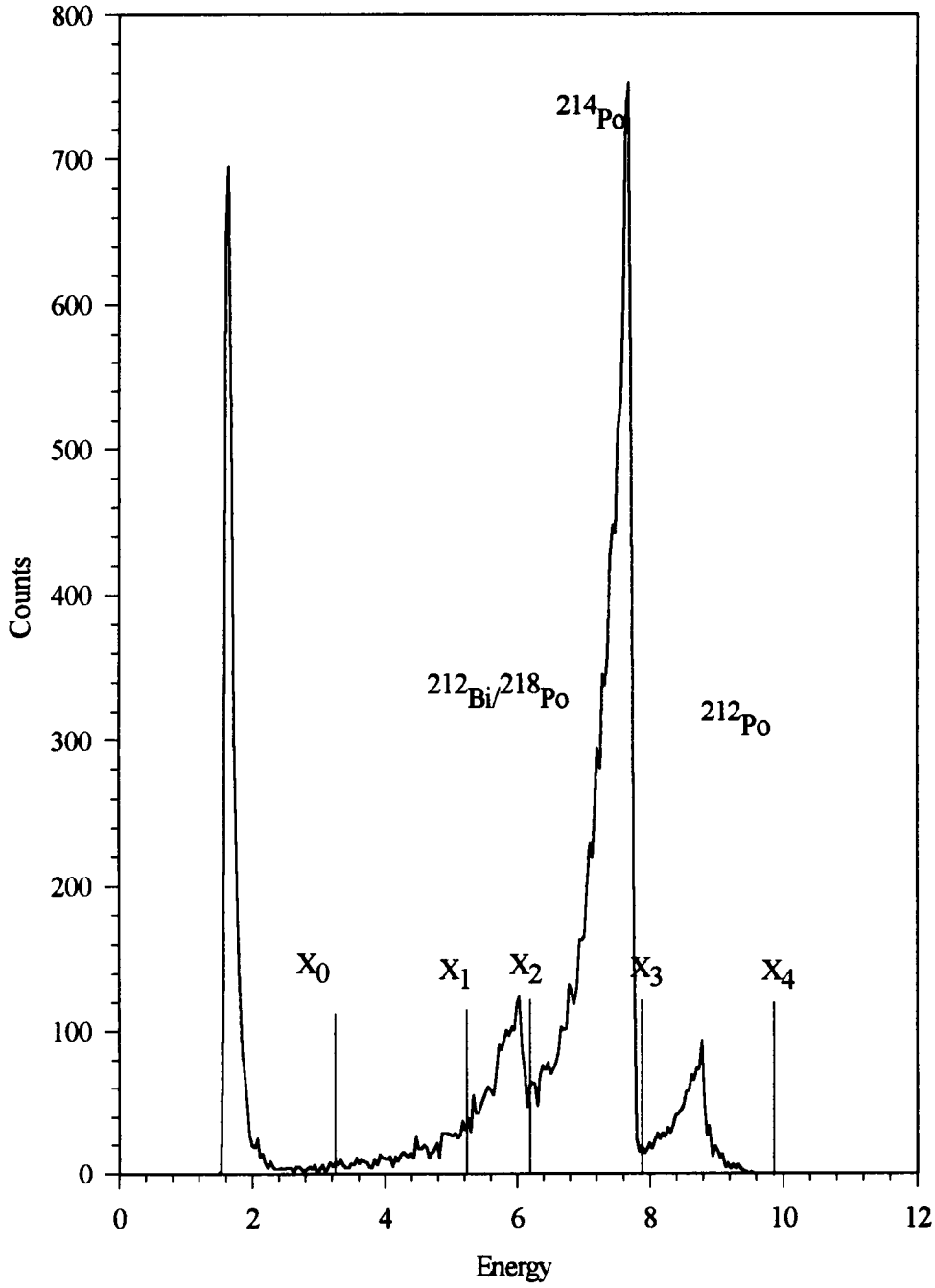


Figure 4.3.2. Representative background spectrum and associated meaningful regions.

However, close inspections of several spectra reveal that the following locations are the most appropriate :

X_1 is the end of the ROI - five channels above the peak energy of the isotope of interest,

X_2 is thirty-eight channels below the channel containing the 7.68 MeV ^{214}Po peak, and

X_3 is five channels above the channel containing the 7.68 MeV ^{214}Po peak.

X_0 defaults to 3.4 MeV upon power up, but it is a parameter the operator may change. X_4 is the last channel in the spectrum. Energy calibration designates the location of X_0 through X_4. The chronic release determination uses both the X_n and Y_n values to determine background contribution from each peak.

Attenuated alpha particle energies contribute long tails to the regions below the peak energy value. These tails begin at the valley point (X_n) below each peak alpha energy. From the spectrum, all alpha energies contribute to the counts at X_0. The naturally occurring background alphas from ^{218}Po (6.003 MeV), ^{212}Bi (6.062 MeV), ^{214}Po (7.687 MeV) and ^{212}Po (8.78 MeV) contribute to the counts at X_1. The ^{214}Po and ^{212}Po alpha particles contribute to the counts at X_2, and the only contribution to the counts at X_3 is from the ^{212}Po alpha particles.

The ratio of counts from the plutonium region of interest ($X_0 \rightarrow X_1$-1) to the sum of counts contained in the $^{218}Po/^{212}Bi$ peak establishes the criteria for an acute release condition. Technical documentation suggests an empirical value of two for this ratio. Additionally, the acute alarm condition does not occur if the total counts in the transuranic ROI are less than eighty. The required minimum number of counts prevents false alarms from occurring when the total counts in the spectrum are low. However, this is an easily changed soft parameter.

In order to estimate the true counts in region 1 (between X_0 and X_1, the transuranic ROI), equations model the attenuated α particles and remove their contribution to the ROI. A curve of the form

$$Y = e^{mX+b} \tag{4.3.2}$$

describes the attenuated α particles that contribute a tail to each peak. The first tail is contributed by the attenuated ^{212}Po α particles between points X_0 and X_3. The second tail is contributed by attenuated ^{214}Po α particles between points X_0 and X_2. The third and final tail is contributed by attenuated ^{218}Po/^{212}Bi α particles between points X_0 and X_1. The mathematical curve fit subtracts the contribution from the attenuated ^{212}Po, ^{214}Po and ^{212}Bi/^{218}Po α particles from each channel. After the attenuated a particles are removed between points X_0 and X_1, the counts between points X_0 and X_1 are due only to counts from contamination.

The equation for the curve fit to each tail in the spectrum is represented as

$$T_{i,j} = e^{m_j X_i + b_j}$$

where X_i is the channel number and $j = 3$ for the 8.78 MeV (^{212}Po) alphas, $j = 2$ for the 7.68 MeV (^{214}Po) alphas, and $j = 1$ for the 6.003 and 6.062 MeV (^{218}Po/^{212}Bi) alphas. The m_n's and b_n's are the respective slope and intercept value for each curve fit and X_i are the channel numbers. The curve for the ^{212}Po tail passes through points X_0 and X_3 representing the contribution of the attenuated ^{212}Po α particles. The counts at channel X_0 are based on the average of five channels,

$$Y_{0(av)} = \frac{1}{5}\sum_{i=X_0-2}^{X_0+2} Y_i, \tag{4.3.3}$$

where Y_i are the counts at channel X_i. This averaging around channel number X_0 aids in preventing spikes or zeros in the spectrum at X_0 from corrupting the curve fit. The counts at X_3, which are all contributed by attenuated ^{212}Po α particles, is given by

$$Y_{3(av)} = \frac{1}{5}\sum_{i=X_3-2}^{X_3+2} Y_i, \tag{4.3.4}$$

The contribution that the attenuated ^{212}Po α particles provide to the counts at Y_0 is given by

$$Y_{0(8.78)} = \frac{\sum_{i=X_3}^{X_4} Y_i}{\sum_{i=X_0}^{X_4} Y_i} Y_{0(av)}. \tag{4.3.5}$$

The numerator in Eq. 4.3.5 is the sum of counts in the 8.78 MeV peak exclusive of the tail and the denominator in Eq. 4.3.5 is the integral of the meaningful spectrum.

Once $Y_{0(av)}$, $Y_{3(av)}$ and $Y_{0(8.78)}$ are determined, the solution of Eq. 4.3.2 for $Y_{0(8.78)}$ at X_0 and for $Y_{3(av)}$ at X_3 yield the values for m_3 and b_3. That is, the solution to the following equations yield the solution for m_3 and b_3: $Y_{0(8.78)} = e^{m_3 X_0 + b_3}$ and $Y_{3(av)} = e^{m_3 X_3 + b_3}$.

The second curve fit, describing the tail of ^{214}Po, passes through points X_0 and X_2. The critical parameters for solving the slope (m_2) and intercept (b_2) are

$$Y_{2(av)} = \frac{1}{5}\sum_{i=X_2-2}^{X_2+2} Y_i \tag{4.3.6}$$

and $$Y_{0(7.68)} = \frac{\sum_{i=X_2}^{X_3} Y_i}{\sum_{i=X_0}^{X_4} Y_i} Y_{0(av)}. \quad (4.3.7)$$

The equations used to solve for m_2 and b_2 are: $Y_{0(7.68)} = e^{m_2 X_0 + b_2}$ and $Y_{2(av)} = e^{m_2 X_2 + b_2}$. The curve fit describing the attenuated $^{218}Po/^{212}Bi$ alpha particles passes through points X_0 and X_1. The critical parameters for determination of m_1 and b_1 are

$$Y_{1(av)} = \frac{1}{5} \sum_{i=X_1-2}^{X_1+2} Y_i \quad (4.3.8)$$

and $$Y_{0(6.05)} = \frac{\sum_{i=X_1}^{X_2} Y_i}{\sum_{i=X_0}^{X_4} Y_i} Y_{0(av)}. \quad (4.3.9)$$

The equations used to determine m_1 and b_1 are: $Y_{0(6.05)} = e^{m_1 X_0 + b_1}$ and $Y_{1(av)} = e^{m_1 X_3 + b_1}$. After determination of the parameters describing each tail in the spectrum, each exponential is extended through the ROI and counts are removed. The counts in the ROI are defined as

$$A_{ROI} = \sum_{i=X_0}^{X_i - 1} Y_i - e^{m_{8.78} X_i - b_{8.78}} - e^{m_{7.68} X_i - b_{7.68}} - e^{m_{6.05} X_i - b_{6.05}}, \quad (4.3.10)$$

where A_{ROI} is the activity in the plutonium region of interest, and Y_i are the counts at each channel in the plutonium region of interest before background compensation. This equation is also represented as

$$A_{ROI} = \sum_{i=X_0}^{X_i-1} Y_i - T_{8.78} - T_{7.68} - T_{6.05}, \qquad (4.3.11)$$

where the T_n's represent the activity integral for each radon progeny in the ROI.

Figure 4.3.3 illustrates the fit of each tail as it extends through the ^{239}Pu ROI. The data in this figure are from a one hour count cycle. The ROI extends from channel 56 to channel 109. The ^{218}Po/^{212}Bi tail begins at channel 56 and extends to channel 110. The ^{214}Po tail begins at channel 56 and extends to channel 133. The ^{212}Po tail begins at channel 56 and extends to channel 178. Figure 4.3.4 illustrates the counts remaining after the chronic release algorithm subtracts each tail from the spectrum.

Note that, this chronic release algorithm biases the results due to the method of determining the contribution from each radon daughter to the lower channel of the ROI. From Eqs 4.3.5, 4.3.7 and 4.3.9 it is evident that the sum of the proportions defining the contribution at X_0 is always less than unity. Closer inspection of Eqs. 4.3.5, 4.3.7 and 4.3.9 reveals that the sum of the numerators is the sum of counts from X_1 to X_4. However, the denominator is the sum of the counts from X_0 to X_4. The effect of this bias is a tendency for the algorithm to fit a curve below the existing background at X_0 when only background counts are present. Further scrutiny of this technique yields an increase in the bias as counts from contamination enter the ROI. As contamination contributes counts to the ROI, the denominator increases, but the numerator stays constant. This tendency to reduce the background contribution at channel X_0 is offset by the counts added to X_0 from contamination. Note from Eq. 4.3.4 that as the counts increase at X_0, the value of $Y_{0(av)}$ increases. If an increase in counts at X_0 is not offset by the increase in the denominator in Eqs. 4.3.5, 4.3.7 and 4.3.9 from the counts contributed by the contamination, the bias will move in the

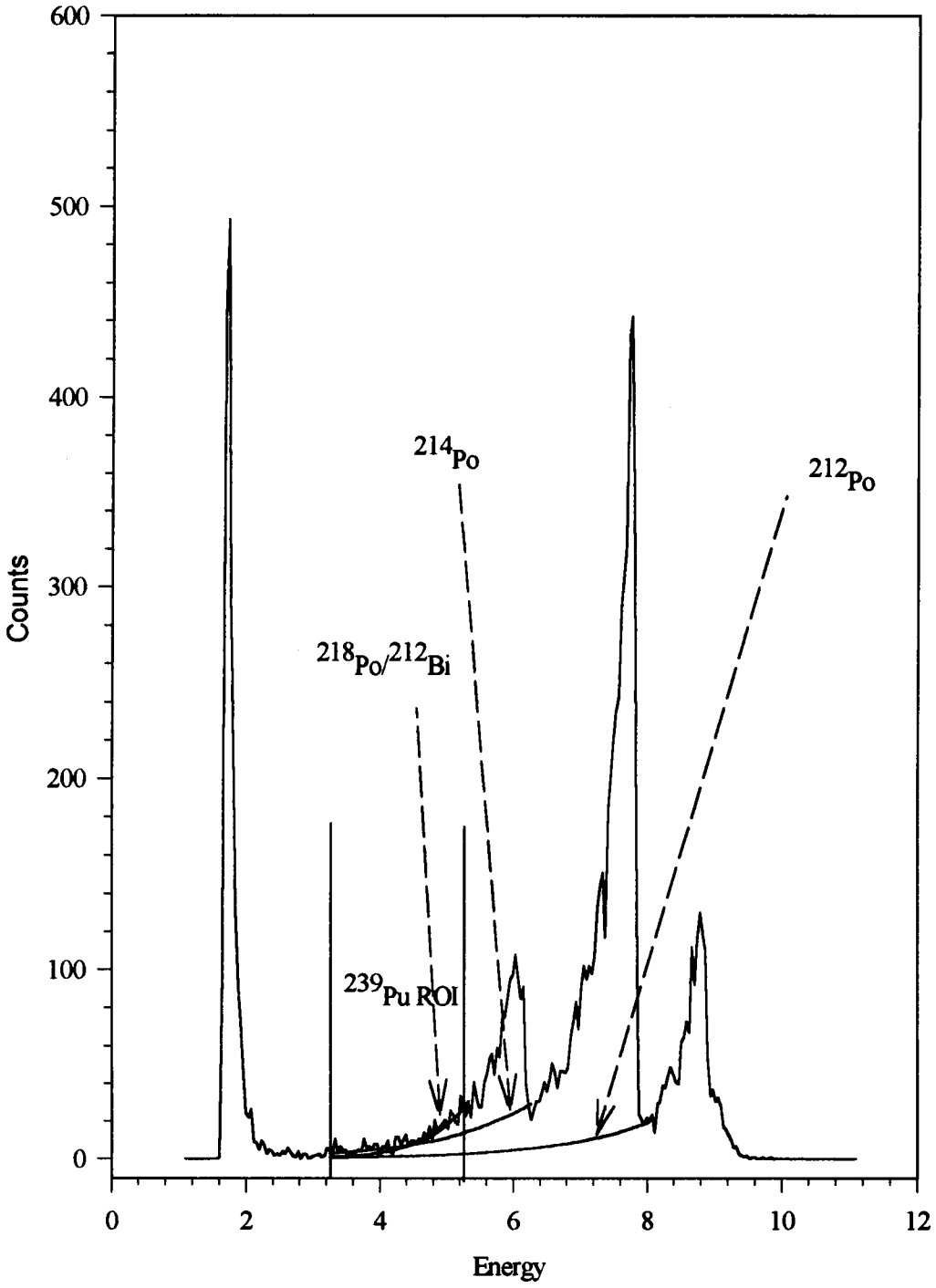


Figure 4.3.3. Fit of exponential tails to each background peak.

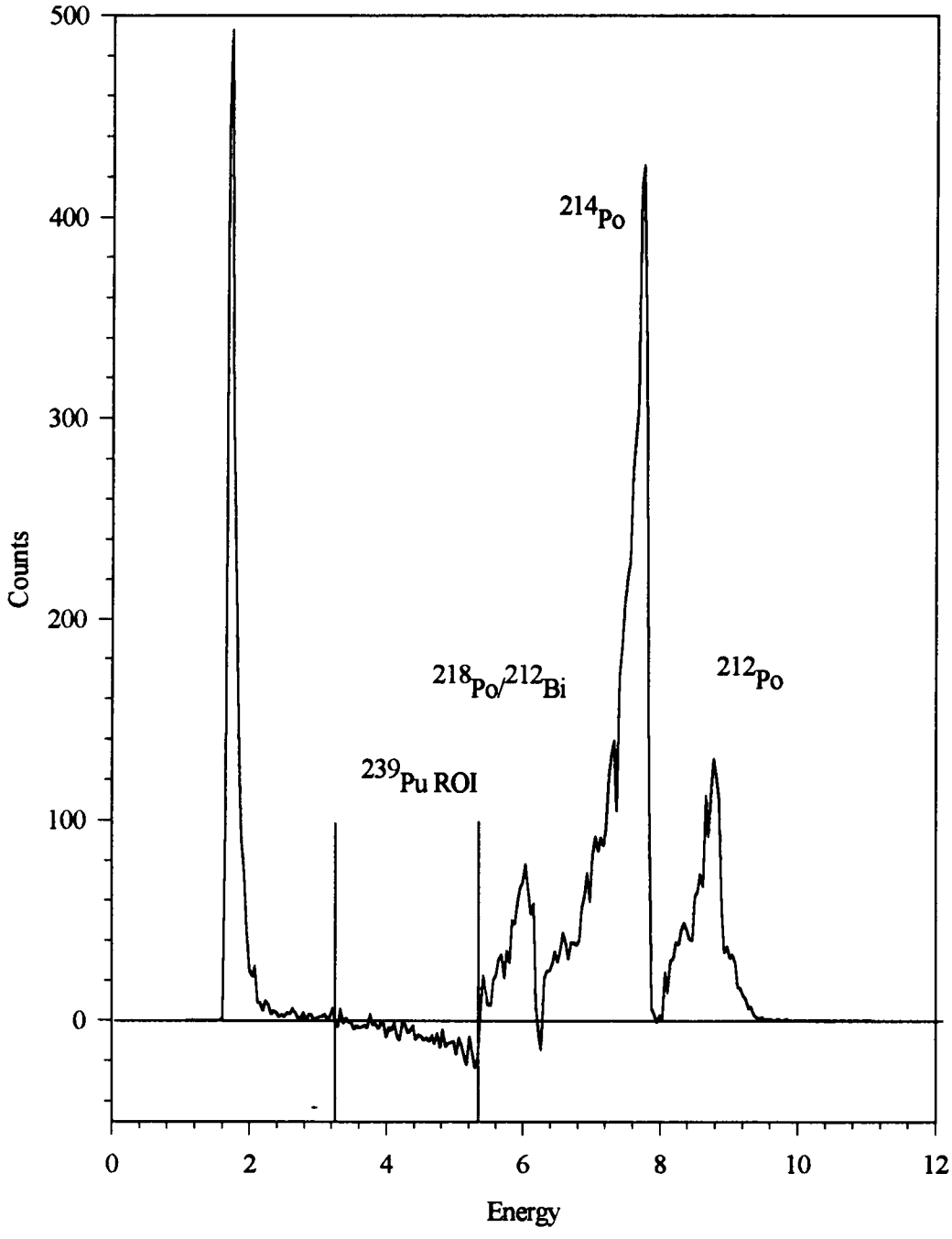


Figure 4.3.4. Residual count distribution in ^{239}Pu ROI following removal of background counts in ROI (Canberra).

opposite direction and the algorithm fits a curve above the true background. This could lead to not detecting contamination when it is present. The total counts in each peak are a Poisson distributed quantity and Canberra uses the formula

$$\sigma_{A_{ROI}} = \sqrt{A_{ROI} + N_{8.78} + N_{7.68} + N_{6.00}} \qquad (4.3.12)$$

to determine the plutonium net area uncertainty (Canberra 1992). The quantities $N_{8.78}$, $N_{7.68}$, and $N_{6.00}$ are the net area of each radon progeny. That is, each N_j equals the sum of counts in peak j plus the integrated counts in tail j. Technical documentation claims that the true measure of uncertainty is given by

$$\sigma_{A_{ROI}} = \sqrt{A_{ROI} + 2T_{8.78} + 2T_{7.68} + 2T_{6.00}} \qquad (4.3.13)$$

where the quantities $T_{8.78}$, $T_{7.68}$, and $T_{6.00}$ are the integral of each radon progeny's tail in the ROI. But the authors state that Eq. 4.3.11 is a more conservative estimate of the statistical uncertainty (Canberra 1992). However, the use of Eq. 4.3.12 as a measure of statistical uncertainty serves to invalidate the underlying statistical principles for determining the uncertainty in the measurement. Altschuler and Pasternack (1962) state that the standard deviation of a measurement, when the background is not accurately known beforehand, is $\sigma_{A_{ROI}} = \sqrt{2 * BKGD + S}$. For this analysis the $BKGD$ should be represented by the sum of $T_{8.78}$, $T_{7.68}$, and $T_{6.00}$. And, S is the number of counts in the ROI after each background contribution is removed.

The critical level, L_c, is the minimum detectable true activity that is measurable with a given degree of confidence (Mayer 1992). The CAM initiates a positive chronic release alarm when the counts in the transuranic ROI exceed the uncertainty estimate multiplied by the desired confidence factor. This level at which the instrument initiates an alarm is the critical level (L_c) and is defined as

$$L_C = \frac{T_i k \sigma_{AROI}}{T_c \varepsilon Z_{DAC} K_1 V}, \quad (4.3.14)$$

where

T_i = time since last filter change (hours),

T_c = spectrum collect time (hours),

V = volume of air that has gone through the filter (liters),

ε = counting efficiency,

Z_{DAC} = DAC factor in (Bq/m^3) from appendix C,

σ_{AROI} = Eq. 4.3.11,

K_1 = conversion factor (3.6 hr*DAC* L), and

k = confidence level.

The conversion factor in the denominator forces the units to match. The net radioactive aerosol concentration is

$$C_{ROI} = \frac{T_i [A_{ROI}(T_i) - A_{ROI}(T_{i-1})]}{T_c^2 \varepsilon K_{xx} V}, \quad (4.3.15)$$

where

C_{ROI} = the net contamination concentration in the region of interest,

$A_{ROI}(T_i)$ = the contamination net area from the current count cycle,

$A_{ROI}(T_{i-1})$ = the contamination net area from the previous count cycle,

T_i = the elapsed time since the last filter change (hours),

i = the total number of collection intervals since the last filter change,

T_c = the spectrum collect time (hours),

V = the total volume of air that has gone through the filter since the last filter change (Liters),

ε = the detector efficiency, and

K_{xx} = a unit conversion factor so the results are presented in the desired output units.

For this analysis, K_{xx} equals 1.332 x 10^2 hr^{-1} pCi^{-1} so that the units of concentration are pCi/L.

Since the instrument discards each spectrum after an analysis, activity in the ROI at time T_i is the change in net counts in the ROI from time T_{i-1} to T_i. If the instrument does not discard the spectrum after each analysis the integral would extend from 0 to T_i, but the instrument does discard the spectrum after each analysis and activity at time T_i is given by

$$A_{ROI}(T_i) = \int_{t_{i-1}}^{t_i} \varepsilon K_{xx} C_{ROI} F \, t \, dt \qquad (4.3.16)$$

where

ε = the detector efficiency,

K_{xx} = the unit conversion factor for the desired units of pCi/L,

C_{ROI} = the concentration of the radionuclide of interest, and

F = the flow rate of the instrument.

Note that Eq. 4.3.16 breaks the volume component of Eq. 4.3.15, V, into two components, flow rate and time. Solution of the integral in Eq. 4.3.17 is

$$A_{ROI}(T_i) = \frac{\varepsilon K_{xx} C_{ROI} F t^2}{2}\Bigg|_{t_{i-1}}^{t_i} \qquad (4.3.17)$$

and

$$A_{ROI}(T_i) = \varepsilon K_{xx} C_{ROI} F \frac{(t_i^2 - t_{i-1}^2)}{2}. \qquad (4.3.18)$$

Activity at time T_{i-1} is

$$A_{ROI}(T_{i-1}) = \int_{t_{i-2}}^{t_{i-1}} \varepsilon K_{xx} C_{ROI} F t \, dt \tag{4.3.19}$$

and

$$A_{ROI}(T_{i-1}) = \varepsilon K_{xx} C_{ROI} F \frac{({t_{i-1}}^2 - {t_{i-2}}^2)}{2}. \tag{4.3.20}$$

The net change in activity between sampling times is then:

$$A_{ROI}(T_i) - A_{ROI}(T_{i-1}) = \varepsilon K_{xx} C_{ROI} F \left[\frac{{t_i}^2 - {t_{i-1}}^2}{2} - \frac{{t_{i-1}}^2 - {t_{i-2}}^2}{2} \right]. \tag{4.3.21}$$

Solving for C_{ROI} yields:

$$C_{ROI} = \frac{A_{ROI}(T_i) - A_{ROI}(T_{i-1})}{\varepsilon K_{xx} F \left[\frac{{t_i}^2 - {t_{i-1}}^2}{2} - \frac{{t_{i-1}}^2 - {t_{i-2}}^2}{2} \right]}. \tag{4.3.22}$$

Factoring the difference of two squares in the denominator, Eq. 4.3.22 becomes

$$C_{ROI} = \frac{A_{ROI}(T_i) - A_{ROI}(T_{i-1})}{\frac{\varepsilon K_{xx} F}{2} \left[(t_i - t_{i-1})(t_i + t_{i-1}) - (t_{i-1} - t_{i-2})(t_{i-1} + t_{i-2}) \right]} \tag{4.3.23}$$

Since all sampling intervals are the same, $t_i - t_{i-1}$ and $t_{i-1} - t_{i-2}$ are equal to the spectrum collection time which is ΔT. Also, $t_i + t_{i-1}$ equals $2t_i - \Delta T$ and $t_{i-1} + t_{i-2}$ equals $t_i - \Delta T + t_i - 2\Delta T$ or $2t_i - 3\Delta T$. Substitution into Eq. 4.3.23 yields

$$C_{ROI} = \frac{A_{ROI}(T_i) - A_{ROI}(T_{i-1})}{\frac{\varepsilon K_{xx} F}{2} \left[(\Delta T)(2t_i - \Delta T) - (\Delta T)(2t_i - 3\Delta T) \right]} \tag{4.3.24}$$

Simplifying Eq. 4.3.24,

$$C_{ROI} = \frac{A_{ROI}(T_i) - A_{ROI}(T_{i-1})}{\frac{\varepsilon K_{xx} F}{2}\left[(\Delta T)(2t_i - \Delta T) - (\Delta T)(2t_i - 3\Delta T)\right]} \tag{4.3.25}$$

Further simplification of Eq. 4.3.24:

$$C_{ROI} = \frac{A_{ROI}(T_i) - A_{ROI}(T_{i-1})}{\varepsilon K_{xx} F \Delta T^2}. \tag{4.3.26}$$

In Eq. 4.3.26 ,where $\Delta T = T_c$, the total volume of air that passes through the filter is the flow rate F multiplied by the time since the last filter change. By substituting $\frac{V}{T_i}$ for F in Eq. 4.3.26 yields Eq. 4.3.15.

The contamination exposure in DAC-hrs (appendix C) is

$$E_{ROI} = \frac{T_i A_{ROI}(T_i)}{T_c \varepsilon K_1 Z_{DAC} V}, \tag{4.3.27}$$

where

T_i = time since last filter change (hours),

T_c = spectrum collect time (hours),

V = volume of air that has gone through the filter (liters),

ε = counting efficiency,

Z_{DAC} =DAC factor in (Bq/m^3) from appendix C, and

K_1 = unity conversion factor (3.6 hr*DAC* L).

The instrument alarm logic for a chronic release is set TRUE for the following conditions:

1) if $(L_C < L_A)$ and $\left(E_{ROI} - L_A\right) > 0$ or (4.3.28)

2) if $(L_C > L_A)$ and $(A_{ROI} - L_C) > 0$ (4.3.29)

where L_A is the user selected alarm threshold in DAC-hrs. The first condition defines an alarm condition if the calculated critical level is less than the user defined exposure limit and the exposure is greater than the user defined exposure limit. The second condition initiates an alarm when the calculated critical level is greater than the user defined alarm limit and activity in the ROI is greater than the critical level.

Technical documentation suggests a value of 2.0 MeV for the width of the ^{239}Pu ROI. Provided that the lower channel of the ROI is not less than 2.6 MeV, each of the other transuranics uses 2.0 MeV as the width of its ROI. If the lower channel of the ROI is less than 2.6 MeV for a width of 2.0 MeV, the lower channel is set at 2.6 MeV. As Fig. 4.3.3 illustrates, below approximately 2.6 MeV the background begins to escalate due to high energy β decay from ^{214}Bi and ^{212}Bi (Figs. 3.1.1 and 3.1.2).

Analysis of the data for the chronic release algorithm includes spectrum data from 131 spectra. A computer collects spectrum data each hour with the chronic release count cycle set at 999 minutes. The collected data is the integrated total of 999 minutes, that is, the first spectrum is the total background for sixty minutes, the second spectrum collected is the total background for one hundred twenty minutes, and so on for a total of 999 minutes. When the count cycle reaches 999 minutes the instrument discards the data and the cycle starts again with the same filter paper. This method is necessary since it is difficult to synchronize the data collection between computer and instrument. The computer defines the cycle of each spectrum since the instrument is collecting data for 999 minutes. Once all the spectra are collected, the counts in each spectrum are subtracted from the previous spectrum yielding net one hour counts.

A filter paper remained in place for 60 hours during the collection of the first data set and another filter remained in place for 71 hours during the collection of the second data set. A program written in C separates the data into individual data files of

equal count time. This code functions for all count times, provided that the data collected from computer is in the same increments of time, i.e., for six minute counts, data collection from the computer is in six minute increments. Appendix A contains the code that simulates actual CAM operation using the present Canberra algorithm. The simulation performs an energy calibration on each of the 131 spectra and performs the stripping routine for each transuranic.

Activity is added to each region of interest based on the particular transuranic simulated. Adding activity consists of adding counts in the ROI equivalent to a concentration of 8 DAC. Section 4.1 outlines the technique employed for distributing the activity of an isotope.

Appendix A also contains the C source code that determines the ratio of the ROI to the top of the ^{218}Po/^{212}Bi peak. This analysis is performed on six hundred six minute counts and on 131 one-hour counts. This ratio determines the level of detection for the acute release algorithm. The ROIs' for this determination are the same as the ROIs' for the chronic release determination.

4.4 Representation of Spectrum as a Superposition of Gamma Functions

The second method of determining a chronic release represents the background spectrum as a superposition of gamma functions. The data for this analysis consists of the same 131 one hour counts used for the previous methods. This approach assumes that each background peak, ^{218}Po (6.003 MeV)/ ^{212}Bi (6.062 MeV), ^{214}Po (7.687 MeV) and ^{212}Po (8.78 MeV), is represented by a gamma function of the form:

$$Y = ae^{-(x-b)/c}((((x-b)/c)+d-1)/(d-1))^{d-1}, \qquad (4.4.1)$$

where

x = the channel number,

Y = the number of counts in channel number x,

a = the peak value of the gamma function,

b = the location of the peak of the gamma function or where $dY/dx = 0$,

c = a width parameter related to the FWHM, and

d = a width parameter related to the FWHM.

Both c and d control the FWHM of the function. Figures. 4.4.1 and 4.4.2 represent the general shape of the function and includes the physical representation of each parameter in the function.

Development of a method to define the most appropriate fit is based partially on an empirical observation regarding parameters a, b, c and d. Parameter a is the number of counts in the peak and parameter b is the location of the peak channel. Directly identifying values for parameters a and b simplifies the curve fit calculation so that only parameters c and d must be identified. From an empirical evaluation of several curve fits performed with Table Curve (1994), the value for parameter d is always less than 1.1 and always greater than 1.0001. From these same evaluations, the value for parameter c is always between 6 and 30. The value of these estimations lies in the ability to limit a search algorithm by applying upper and lower bounds. This greatly reduces computation time and aides in removing errors associated with an erroneous fit.

Reversing the spectrum results in a correspondence between the natural shape of the gamma function and the attenuated alpha particles allowing the gamma function to correctly represent the background α particles. Reversing the data set involves transposing the channel numbers so the counts in channel 0 are assigned to channel 255, counts in channel 1 are assigned to 254 and so on until each channel. This method

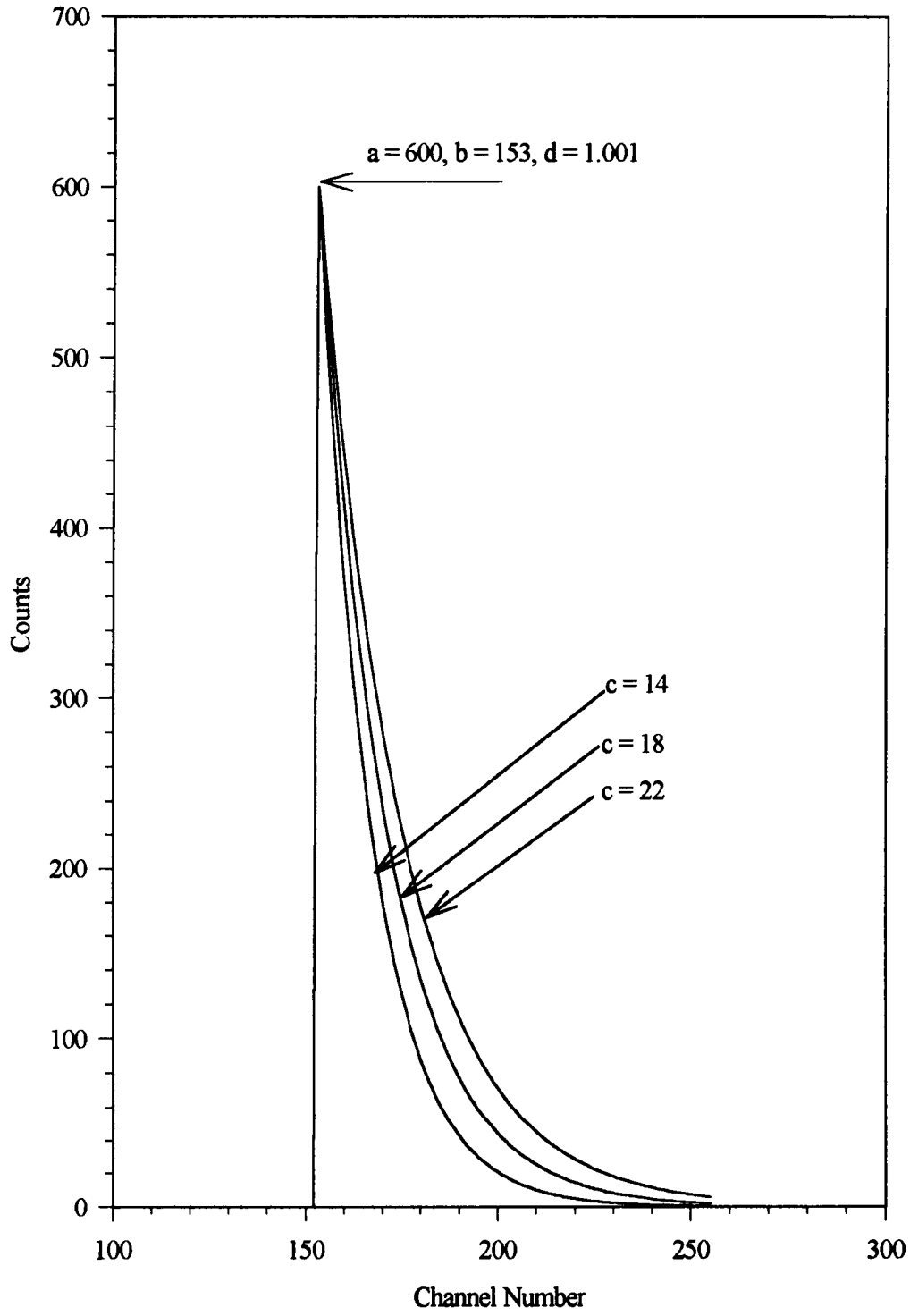


Figure 4.4.1. Gamma function for different values of parameter *c*.

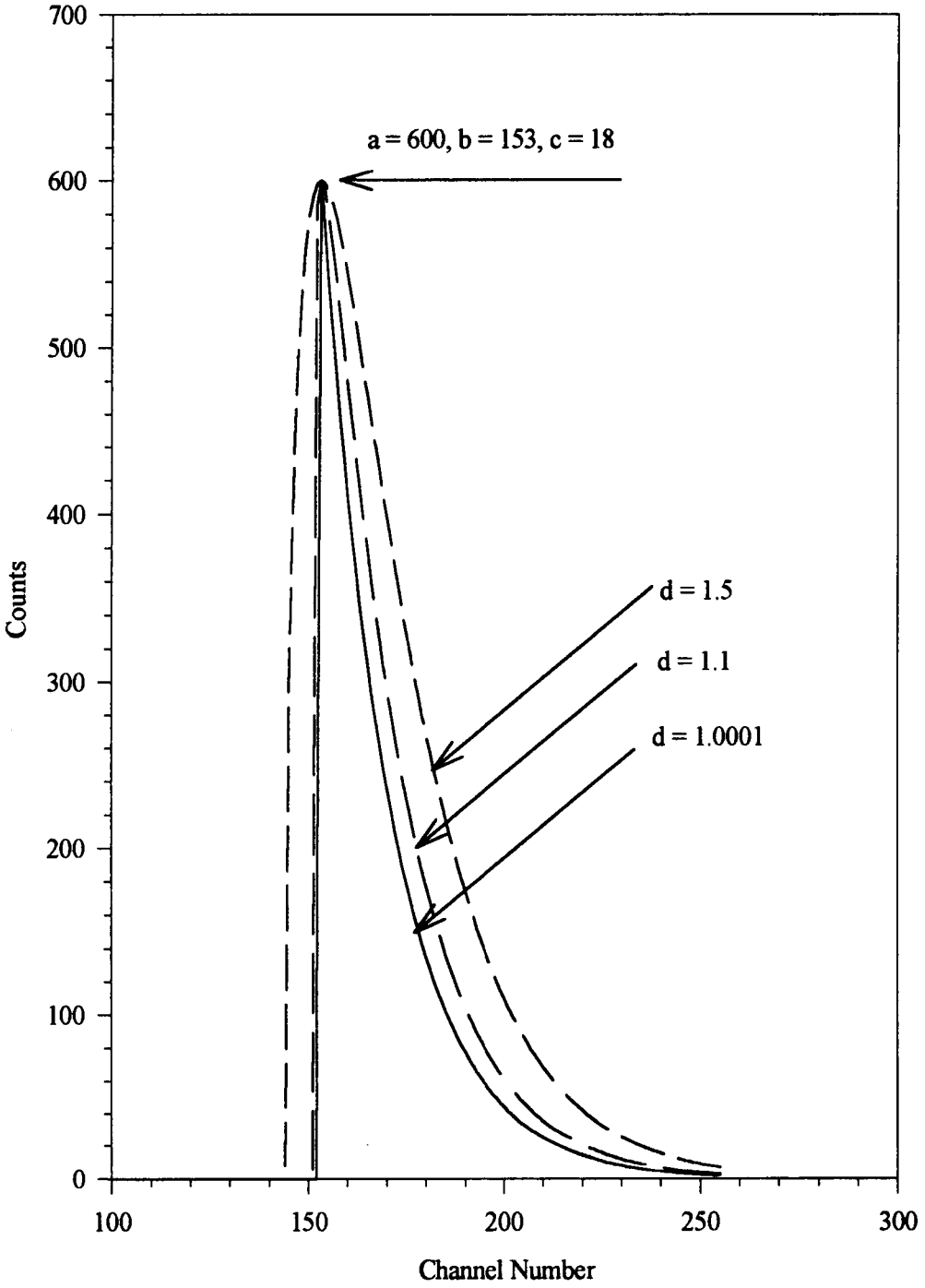


Figure 4.4.2. Gamma function for different values of parameter *d*.

of transforming the data does not influence the validity of the analysis since each mathematical operation is performed on this transposed spectrum. The correspondence between the background spectrum and the gamma function permits a prediction of the number of background α counts that lie in the ROI and the subsequent removal of these α counts. Appendix B contains the C language source code used to perform this analysis.

In order to evaluate this method, a series of spectra collected from a ^{239}Pu disk source placed in the filter holder assembly were evaluated by fitting a gamma function (Eq. 4.4.1) to each spectrum. Figure 4.4.3 consists of a ^{239}Pu spectrum and the corresponding gamma function that describes the data. This curve fit and all others for this analysis is based on an iterative search for parameters *c* and *d*. The best fit is defined by the set of parameters that return the smallest value for the following equation:

$$R = \sum_{x=X_0}^{x=X_1} |Y(x) - Data(x)| \qquad (4.4.2)$$

where

X_0 and X_1 are the channel numbers defining the upper and lower bounds of the ROI (Fig. 4.3.2),

R is the sum of the absolute value of the residuals,

Y(x) is the value of the gamma function at channel *x*, and

Data(x) is the number of counts at channel *x*.

The gamma function is determined over all values of *i* and *j* for each ROI and is represented as:

$$Y_{i,j} = ae^{-(x-b)/c_i}(((x-b)/c_i)+d_j-1)/(d_j-1)^{d_j-1}\ , \qquad (4.4.3)$$

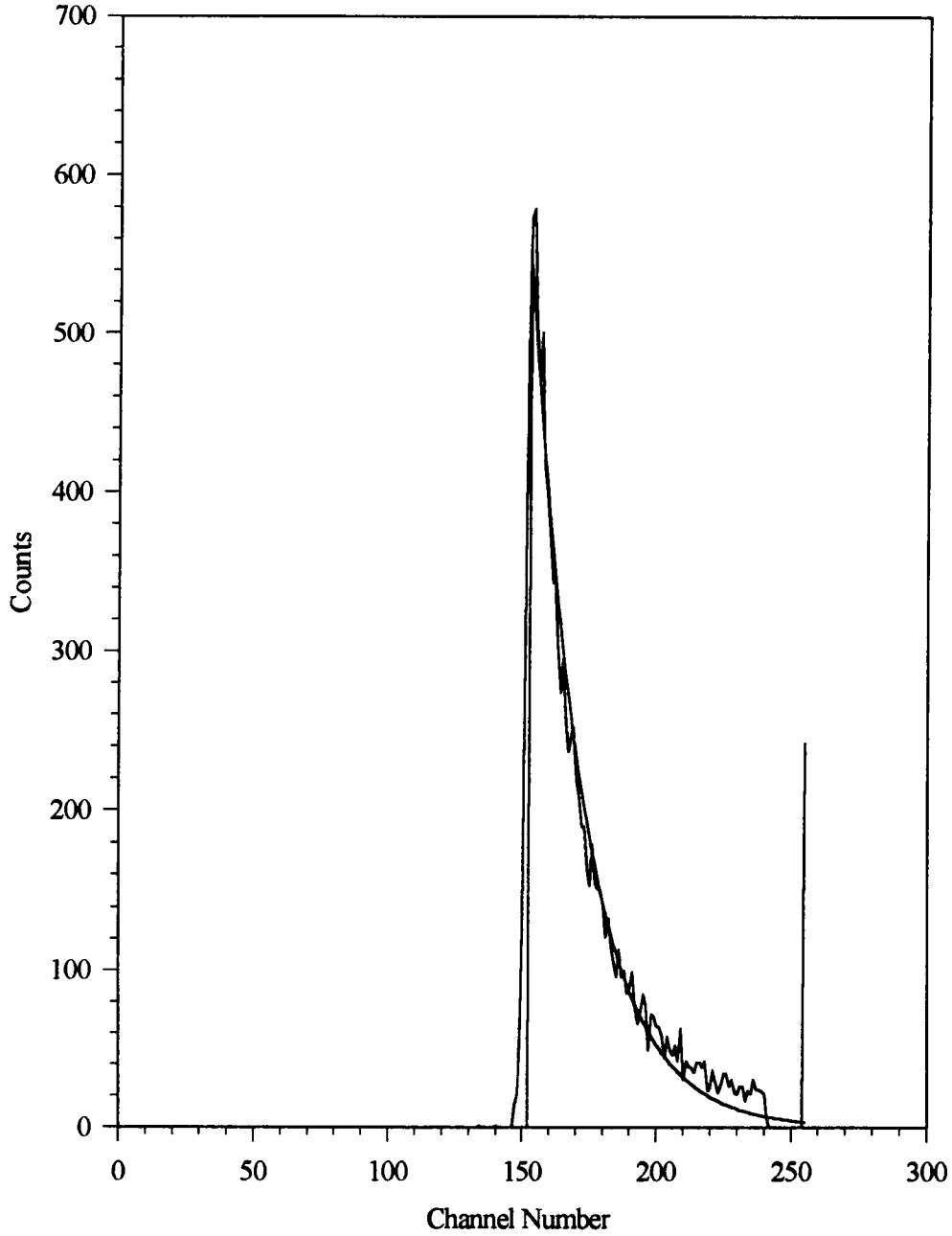


Figure 4.4.3. Fit of gamma function to ^{239}Pu spectrum.

where i = 1 to 100 and j = 1 to 100. Parameter c is evaluated for 100 even increments between 6 and 30 and parameter d is evaluated for 100 even increments between 1.0001 and 1.1.

To determine the accuracy of the algorithm used in this analysis, both this algorithm and Table Curve were used to fit a gamma function to seven ^{239}Pu spectra. Tables 4.4.1 and 4.4.2 compare the results obtained from each technique of fitting the same gamma function to each ^{239}Pu spectrum. The quantity $\sum$ |R/n| in tables 4.4.1 and 4.4.2 is the sum of the residuals divided by the number of points in the fit. From tables 4.4.1 and 4.4.2 it is evident that this iterative algorithm evaluates to approximately the same parameter estimation as the more complex algorithm used by Table Curve.

Even though the spectrum in Figs. 4.4.4 through 4.4.7 was reversed for the analysis, Figs. 4.4.4 through 4.4.7 have the natural appearance of a spectrum collected by the MCA. Each radon progeny α particle creates a peak in the spectrum and contributes a continuum of counts to the lower energy channels of the spectrum. The α particles from ^{212}Po contribute counts to the channels containing ^{214}Po α particles and ^{218}Po/^{212}Bi α particles and the α particles from ^{214}Po contribute counts to the channels containing ^{218}Po/^{212}Bi α particles. To estimate and remove radon daughter counts in the ROI each peak is fit with the gamma function of Eq. 4.4.1 and subtracted from the spectrum. This operation of removing background counts begins with the highest energy peak (^{212}Po) and proceeds to the lowest energy peak (^{218}Po/^{212}Bi).

The process of removing radon progeny counts with the gamma function proceeds as follows:

1) The highest energy peak ^{212}Po (8.78 MeV) is fit with a gamma function and the counts are removed from each channel of the spectrum. Data defining the

Table 4.4.1. Parameter estimation using Table Curve.

Observation	Parameter *a*	Parameter *b*	Parameter *c*	Parameter *d*	$\sum$ |R/n|
1	504.483	152.762	19.287	1.00001	14.0
2	557.94	152.047	20.193	1.002	15.3
3	557.978	152.763	14.246	1.01	37.3
4	688.661	152.271	18.946	1.014	20.0
5	728.853	151.945	18.335	1.052	16.9
6	793.805	152.029	18.009	1.057	21.6
7	872.250	151.87	15.353	1.01	42.0

Table 4.4.2. Parameter estimation using iterative technique.

Observation	Parameter *a*	Parameter *b*	Parameter *c*	Parameter *d*	$\sum$ |R/n|
1	498.67	153	19.4	1.001	15.3
2	552.00	153	19.7	1.002	16.7
3	621.67	153	19.1	1.002	17.7
4	688.33	153	19.1	1.001	20.1
5	763.33	153	19.1	1.002	22.5
6	840.67	153	18.8	1.002	25.0
7	920.00	153	18.8	1.001	27.6

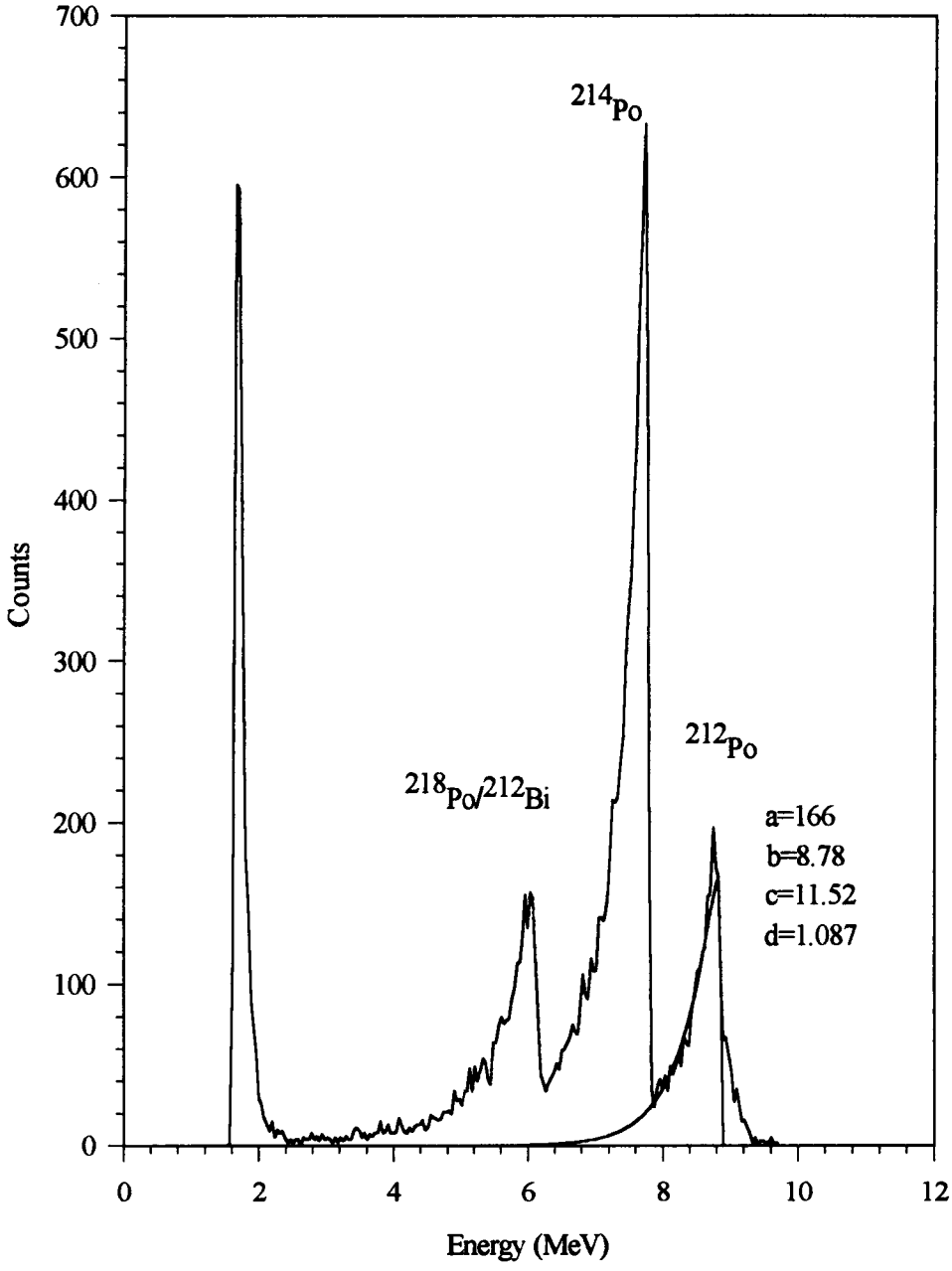


Figure 4.4.4. Fit of gamma function to ^{212}Po peak.

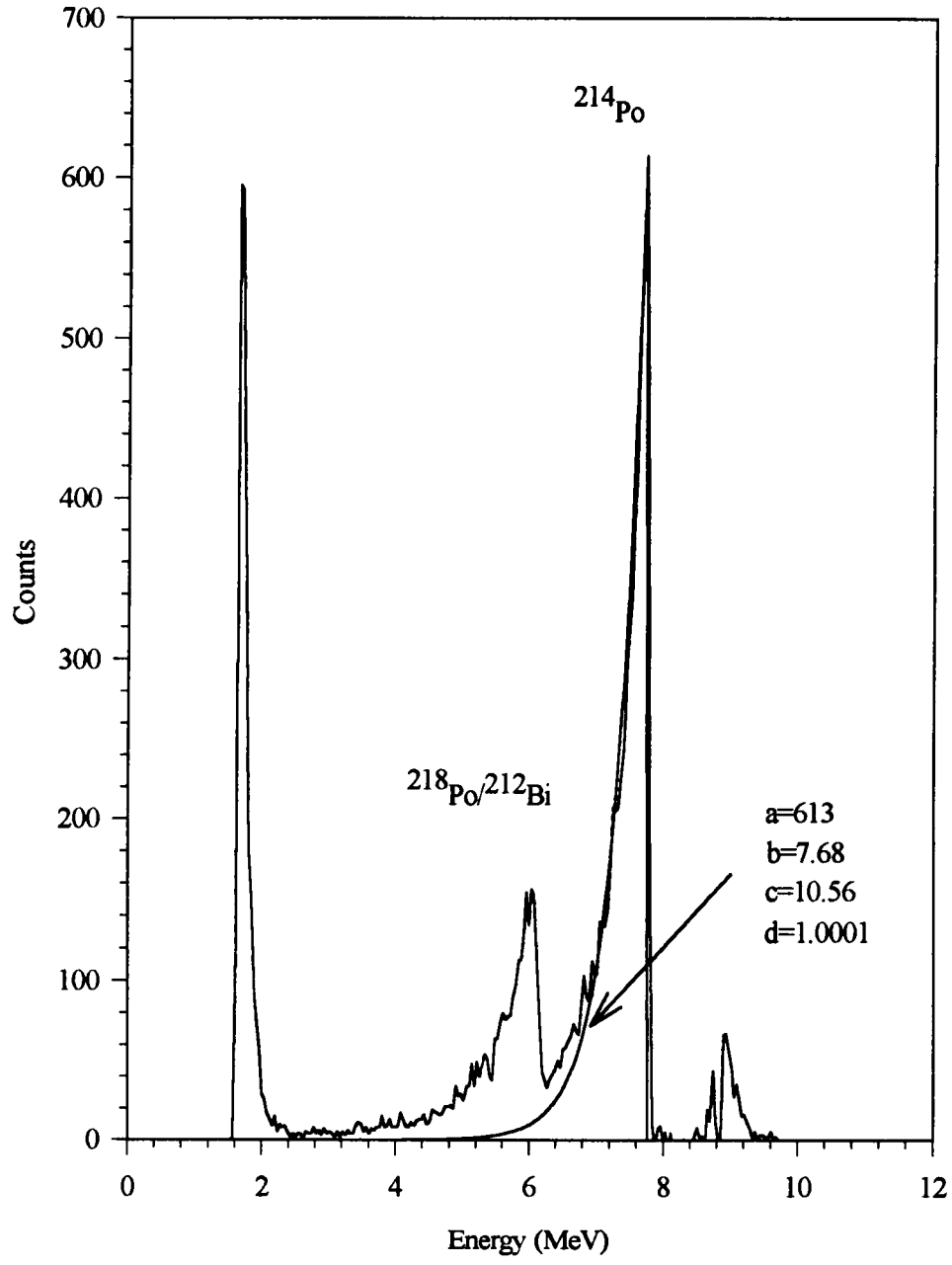


Figure 4.4.5. Fit of gamma function to ^{214}Po peak.

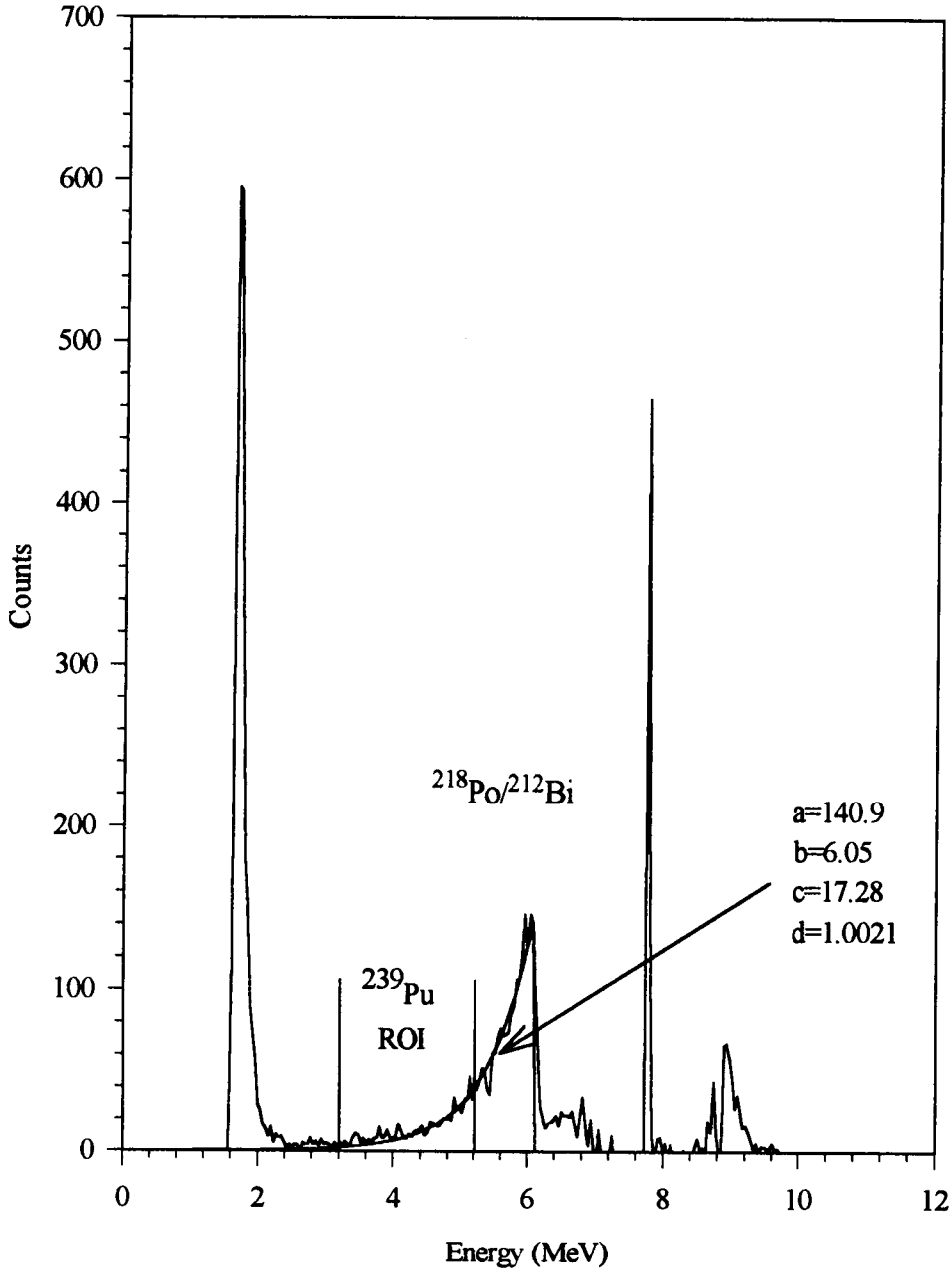


Figure 4.4.6. Fit of gamma function to $^{218}Po/^{212}Bi$ peak.

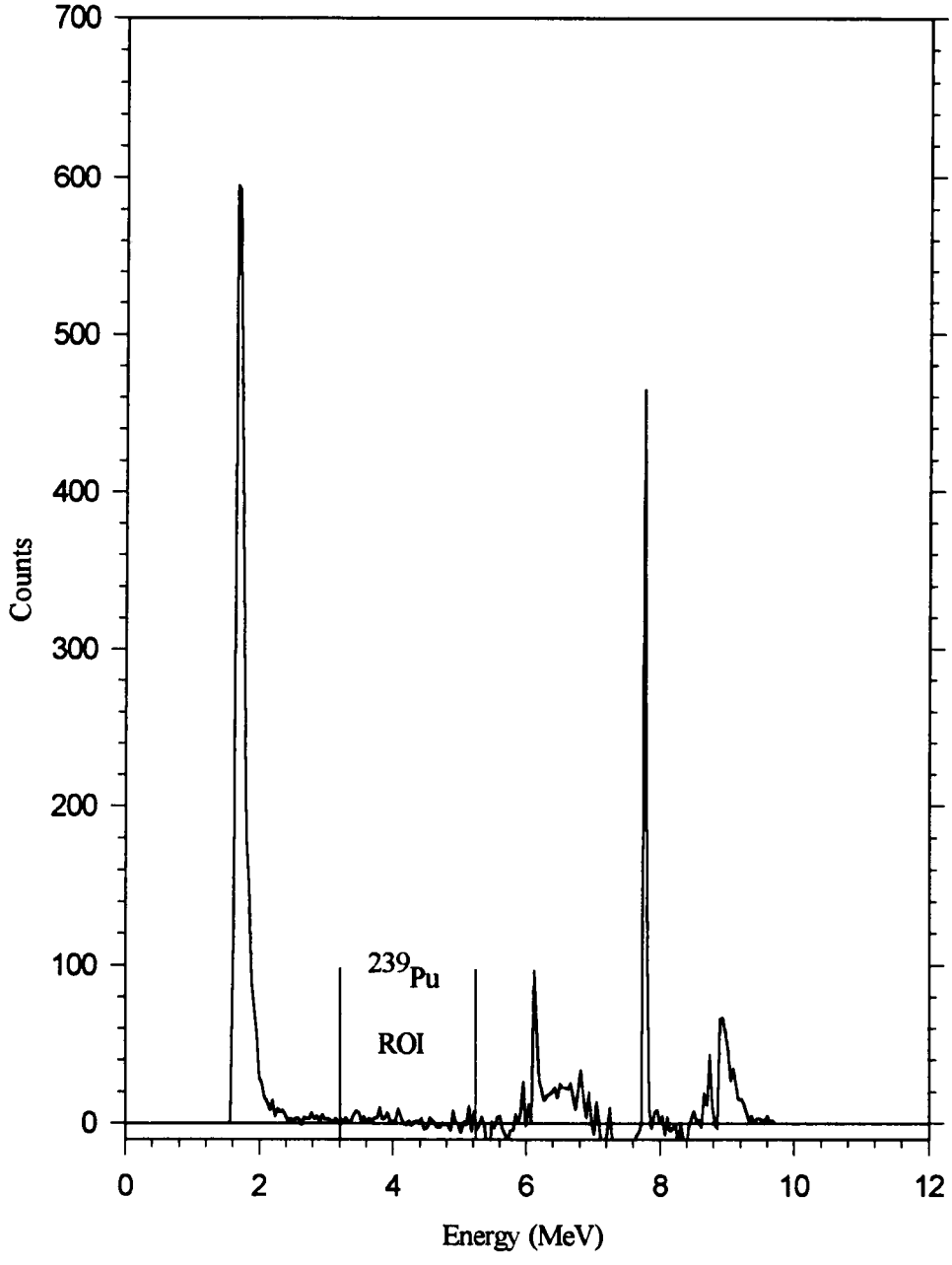


Figure 4.4.7. Activity distribution in ^{239}Pu ROI following removal of each peak using a gamma function.

curve fit are from three channels above the ^{212}Po peak to three channels above the ^{214}Po peak.

2) The second highest energy peak ^{214}Po (7.68) is fit with a gamma function and the counts are removed from each channel of the spectrum. Data defining the curve fit are from three channels above the ^{214}Po peak to three channels above the ^{218}Po/^{212}Bi peak.

3) The lowest energy peak ^{218}Po/^{212}Bi (6.0 MeV) is fit with a gamma function and the counts are removed from each channel of the spectrum. Data defining the curve fit are from three channels above the ^{218}Po/^{212}Bi peak down to the transuranic ROI.

Following removal of each peak, a straight line is fit from the channel defined by 6.05 MeV to the channel defined by 2.6 MeV. Data defining this linear least squares fit are the 10 channels above 2.6 MeV and the channels from 6.05 MeV down to the ROI. Figure 4.4.4 is a fit of the gamma function to the ^{212}Po peak and contains all the counts contributed by radon daughter α particles. Figure 4.4.5 is a fit of the gamma function to the ^{214}Po peak with the contribution from ^{212}Po removed. Figure 4.4.6 is a fit of the gamma function to the ^{218}Po/^{212}Bi peak with the contributions from both ^{212}Po and ^{214}Po removed. Figure 4.4.7 is the spectrum after each peak has been fit with a gamma function and removed from the spectrum. Figure 4.4.8 illustrates the residual counts in the ROI after applying the linear least squares fit.

Choice of data used to fit the straight line aides in minimizing the effects caused by contamination in the ROI. If all the data from 6.05 MeV to 2.6 MeV is used to fit the line, counts in the ROI from contamination significantly bias the fit. To minimize this bias, the fit uses the ten lowest energy channels and the channels above the ROI. To aide in removing biases caused by counts due to the presence of a

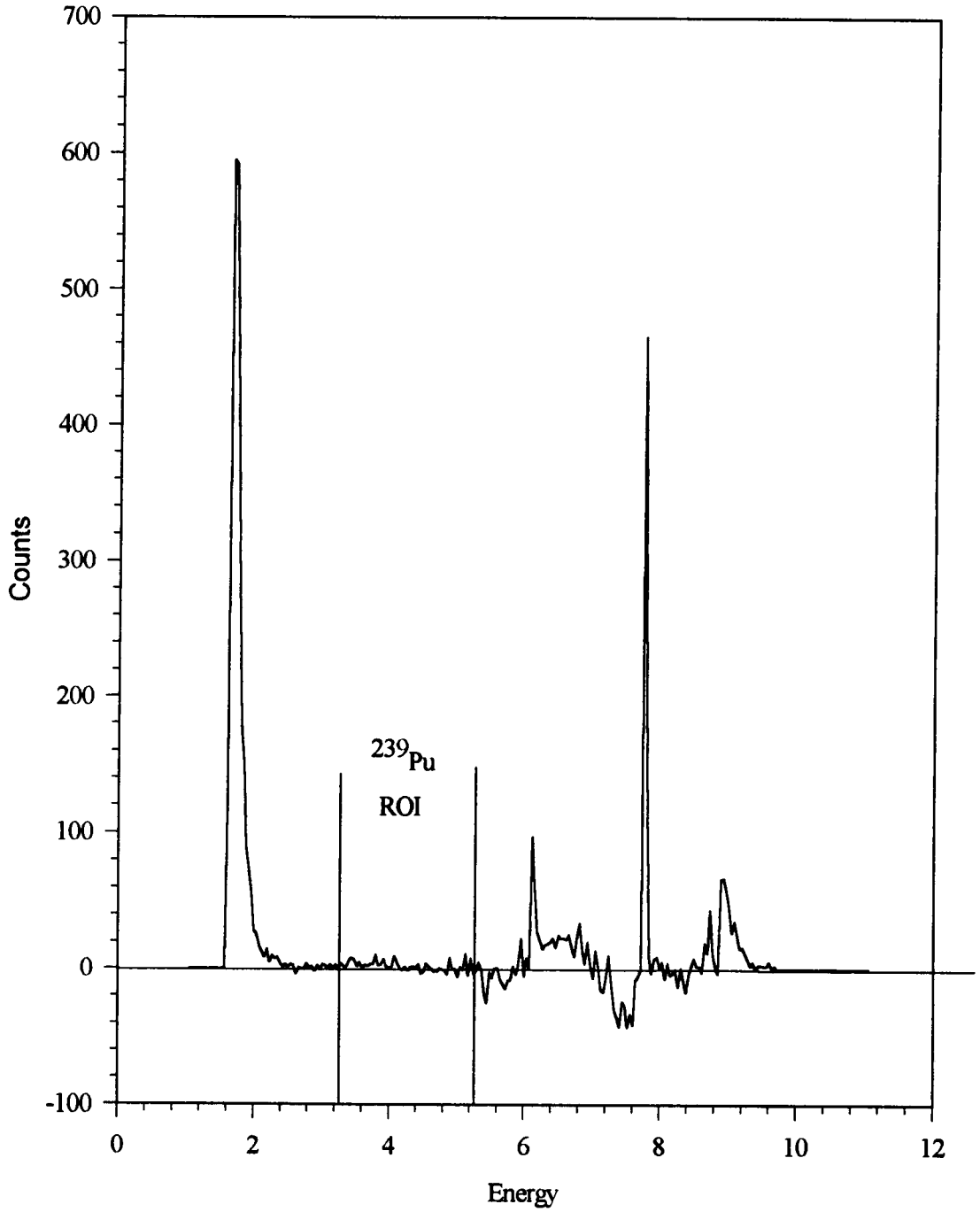


Figure 4.4.8. Activity distribution in ^{239}Pu ROI (superposition of gamma functions).

transuranic the choice of channels avoids the regions that surround the peak energy of the transuranic. Having predicted and removed the background in the ROI due to each naturally occurring radon daughter the remaining counts in the ROI are assumed to be true activity from the radionuclide of interest. The background in the ROI is represented by the sum of the integrals of each gamma function from the beginning of the ROI to the end of the ROI and by sum of counts removed by the straight line fit through the ROI. Background is thus defined as

$$BKGD = \sum_{i=Peak-50}^{i=Peak+3} \left(Y_{212\,Po} + Y_{214\,Po} + Y_{218\,Po/212\,Bi} \right) + Y_{ROI} \qquad (4.4.4)$$

where

$BKGD$ = the predicted background in the ROI,

$Peak$ = the channel representing the characteristic alpha energy of the radionuclide of interest,

$Y_{212\,Po}$ = the gamma function that predicts the counts due to ^{212}Po,

$Y_{214\,Po}$ = the gamma function that predicts the counts due to ^{214}Po,

$Y_{218\,Po/212\,Bi}$ = the gamma function that predicts the counts due to ^{218}Po and ^{212}Bi, and

Y_{ROI} = the equation that describes the straight line fit through the data following removal of each background peak.

The counts remaining in the ROI are assumed to be from contamination since the expected background has been removed. The assumed width of the region of interest of 53 channels enables direct comparison between this technique and the technique presently employed in the instrument.

4.5 Statistics Used To Evaluate Chronic Release

The sample activity is defined by

$$S = A_{ROI} - BKGD, \tag{4.5.1}$$

where

A_{ROI} = the counts in the ROI prior to background subtraction, and

$BKGD$ = Eq. 4.4.4.

The standard deviation of the counts in the region of interest is defined by

$$\sigma_{A_{ROI}} = \sqrt{2 * BGKD + S}, \tag{4.5.2}$$

where

$BKGD$ = Eq. 4.4.4, and

S = sample activity.

Each chronic release algorithm is evaluated against spectra containing only background counts and spectra containing both background counts and counts due to contamination. An airborne concentration equivalent to 8 DAC, expressed in units of pCi/L, is calculated utilizing Eq. 4.3.14 and added to each spectrum.

When there is contamination present in the spectrum, but the analysis determines that contamination is not present, type I error has occurred. When contamination is not present in the spectrum , but the analysis determines that contamination is present, type II error has occurred. The critical level ,or the lower limit of detection, is a function of the risk of making a type I or type II error. This analysis uses the same probability for both errors. The confidence level is 95%, which gives a 5% chance of deciding there is no true activity due to contamination ,when in fact there is, and it gives a 5% chance of deciding there is true activity, when in fact there is none. This lower limit of detection (LLD) or critical level is expressed as

$$\text{LLD} = \frac{(k_\alpha + k_\beta)\sigma_{A_{ROI}}}{T_c \varepsilon} \qquad (4.5.3)$$

where k_β and k_α represent the confidence level for making type I and type II errors. A confidence interval of 95% gives k_β and k_α equal to 1.96. If T_c is in units of seconds, Eq. 4.5.3 has units of Bq and the minimum detectable true activity is analogous to the critical level defined by Canberra as Eq. 4.2.13.

The method used to determine the standard deviation in the current algorithm, Eq. 4.3.11, is compared to using the method suggested by Altschuler and Pasternack. This analysis also investigates the effect on lower limits of detection and alarm levels using the two methods to determine critical levels. A full simulation is run for both the current algorithm and the representation of the spectrum as a superposition of gamma functions. These simulations allow for evaluation of the current techniques used to assess the background condition as well as the sample activity and provides a benchmark for the expected performance of this CAM sampler in similar working levels and environments.

5. RESULTS AND DISCUSSION

5.1 Results Of Working Level Determination

This section presents the results of Kawaji's technique for determining the working level of radon. The working level, defined by Eq. 4.2.20, varies from a minimum of 0.0117 to a maximum of 0.1397 with a mean of 0.0438. Figure 5.1.1 illustrates how the working level varies over. Observation one occurs at approximately 11:00 a.m. and each of the next 60 observations are sequential observations occurring in one hour increments. The second set of observations, beginning with observation 62, also begins at approximately 11:00 a.m.. Due to diurnal effects, including temperature and humidity, the concentration of radon daughters is greatest approximately 20 hours from the beginning of the analysis. After this peak value, which occurs at approximately 7:00 a.m., the concentration of radon daughters rapidly decreases. The concentration of radon daughters peaks the second day at approximately 4:00 a.m.. Although the data for the analysis only spans five days, a general conclusion from the data is that the concentration of radon daughters is greatest in the early morning hours of each day, between 2:00 a.m. and 8:00 a.m..

5.2 Results of the Acute Release Algorithm

This section analyzes the results of Canberra's method of determining an acute release. These results are based on six-hundred six minute counts which were collected consecutively for a period spanning 3.5 days. The ratios used for determining the acute release alarm settings are presented in table 5.2.1 as a mean ratio, 99% confidence interval for each mean ratio, and standard deviation for each mean ratio. Results indicate that the ratio for the ^{239}Pu ROI is almost a factor of four lower than the 2.0

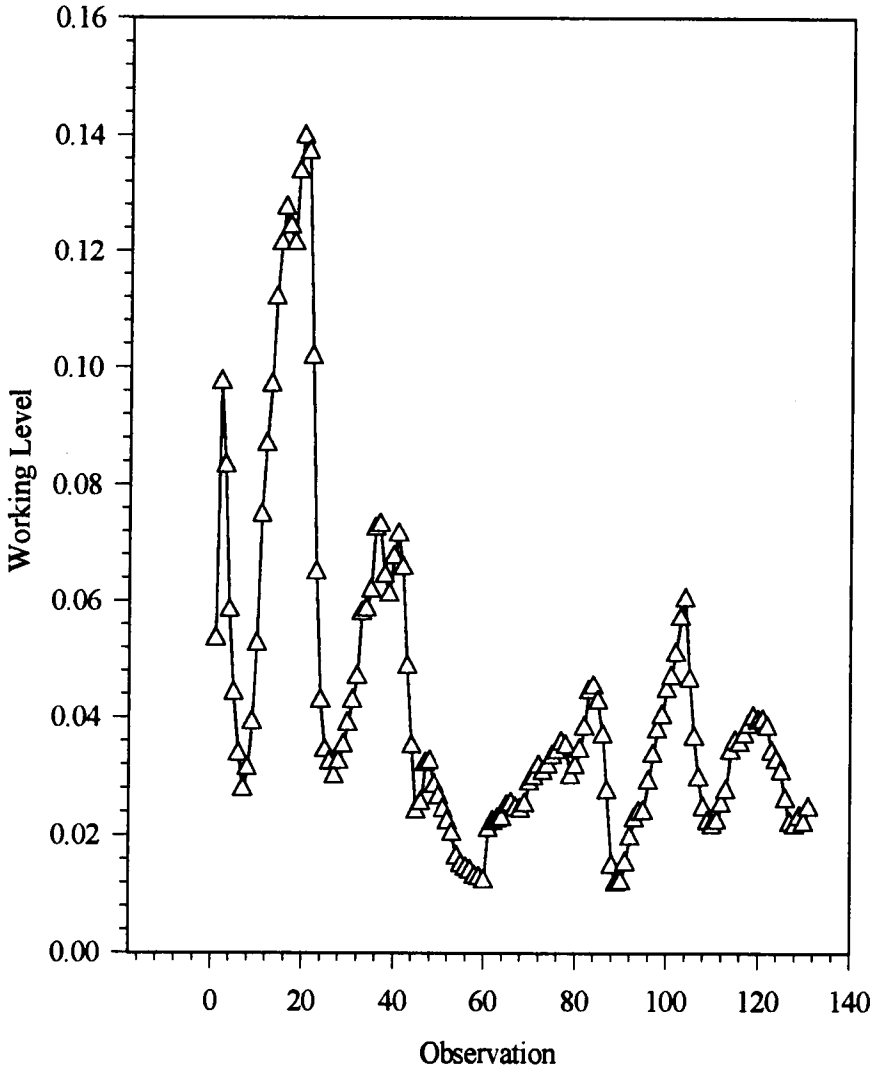


Figure 5.1.1. Working levels for each chronic release analysis.

Table 5.2.1. Mean ratio and 99% confidence limits (CL) for each transuranic.

Isotope	Mean Ratio	Lower CL	Upper CL	Standard Deviation
^{232}Th	0.1048	0.0998	0.1098	0.0473
^{238}U	0.1381	0.1323	0.1439	0.0545
^{235}U	0.2246	0.2165	0.2327	0.0768
^{234}U	0.2944	0.2847	0.3041	0.0920
^{237}Np	0.2944	0.2847	0.3041	0.0920
^{242}Pu	0.3723	0.3834	0.3834	0.1053
^{239}Pu	0.5735	0.5578	0.5892	0.1491
^{243}Am	0.7393	0.7181	0.7605	0.2014
^{232}U	0.8094	0.7868	0.8320	0.2145
^{228}Th	1.1090	1.0773	1.1407	0.3000
^{241}Am	1.4261	1.3826	1.4696	0.4125
^{238}Pu	1.4291	1.3856	1.4726	0.4127

ratio suggested by the technical documentation. With a standard deviation of 0.1470, the mean ratio for ^{239}Pu is more than 9 standard deviations lower than the suggested 2.0 ratio. These results indicate that a lower value than 2.0 for the ^{239}Pu acute release threshold is tolerable which would increase the acute release sensitivity of the instrument.

Of course, choice of ROI and width of ROI greatly impacts this evaluation, note that the width of each ROI is the same as suggested in the technical documentation with the exception of ^{232}Th and ^{238}U. These isotopes contain energies that due not allow the ROI to span 52 channels which is the equivalent of 2.0 MeV. Therefore, the lower energy for these two isotopes is 2.6 MeV.

5.3 Results of the Chronic Release Algorithms

Since the counts assigned to point X_2 ($Y_{2(av)}$) are an average of five channels (Eq. 4.3.6), point X_2 should not be assigned closer than five channels above the ^{218}Po/^{212}Bi peak. Assigning point X_2 closer than five channels above the ^{218}Po/^{212}Bi peak inflates $Y_{2(av)}$ and the resulting curve fit incorrectly represents the tail of the ^{214}Po peak. Likewise, assigning point X_3 closer than five channels above the ^{214}Po peak inflates $Y_{3(av)}$ (equation 4.3.4) and the resulting curve fit incorrectly represents the tail of the ^{218}Po peak. These considerations determined the settings for each X_n outlined in section 4.3.

Canberra's algorithm models the attenuation of radon progeny α particles with a single exponential. The algorithm outlined in section 4.4 models the attenuation of radon progeny α particles with the product of two exponentials. However, these models may incorrectly describe the true response of α particle attenuation in the spectrum. Incorrect modeling of the true α particle attenuation causes the models to

describe some regions of the spectrum more accurately than they describe other regions of the spectrum. Therefore, the results in this section graphically illustrate the residual distribution of a low energy ROI (^{232}Th) and compare this residual distribution to a high energy ROI (^{239}Pu). The ^{239}Pu ROI is chosen because the algorithm designed by Canberra is based on this ROI and the ^{232}Th ROI is chosen because it is the lowest energy transuranic studied.

Canberra's chronic release algorithm produced the histogram of residuals illustrated by Fig. 5.3.1 for the ^{239}Pu ROI. From Fig. 5.3.1 the residual distribution appears approximately normally distributed with a slight skewness and has a mean of -328.7 and standard deviation of 246.4. In comparison, describing each spectrum as a superposition of gamma functions provided the distribution of residuals given by Fig. 5.3.2. With a mean of -23.3 and a standard deviation of 143.1, the histogram of residuals for this algorithm appears more normally distributed, contains a smaller mean and standard deviation, and appears less skewed than the histogram of residuals produced by the Canberra algorithm.

Figures 5.3.3 and 5.3.4 are the residual distributions in the ^{232}Th ROI for each chronic release algorithm. Canberra's algorithm produced a residual distribution with a mean of -156.9 and a standard deviation of 109.8 (Fig. 5.3.3). Describing the spectrum as a superposition of gamma functions produced a residual distribution with a mean of 60.9 and a standard deviation of 66.8 (Fig. 5.3.4). Again, describing the spectrum as a superposition of gamma functions produced a histogram of residuals that appears more normally distributed, contains a smaller mean and standard deviation, and appears less skewed than the histogram of residuals from the Canberra algorithm. Tables 5.3.2 and 5.3.3 provide a comparison of the mean, 95% confidence interval, and

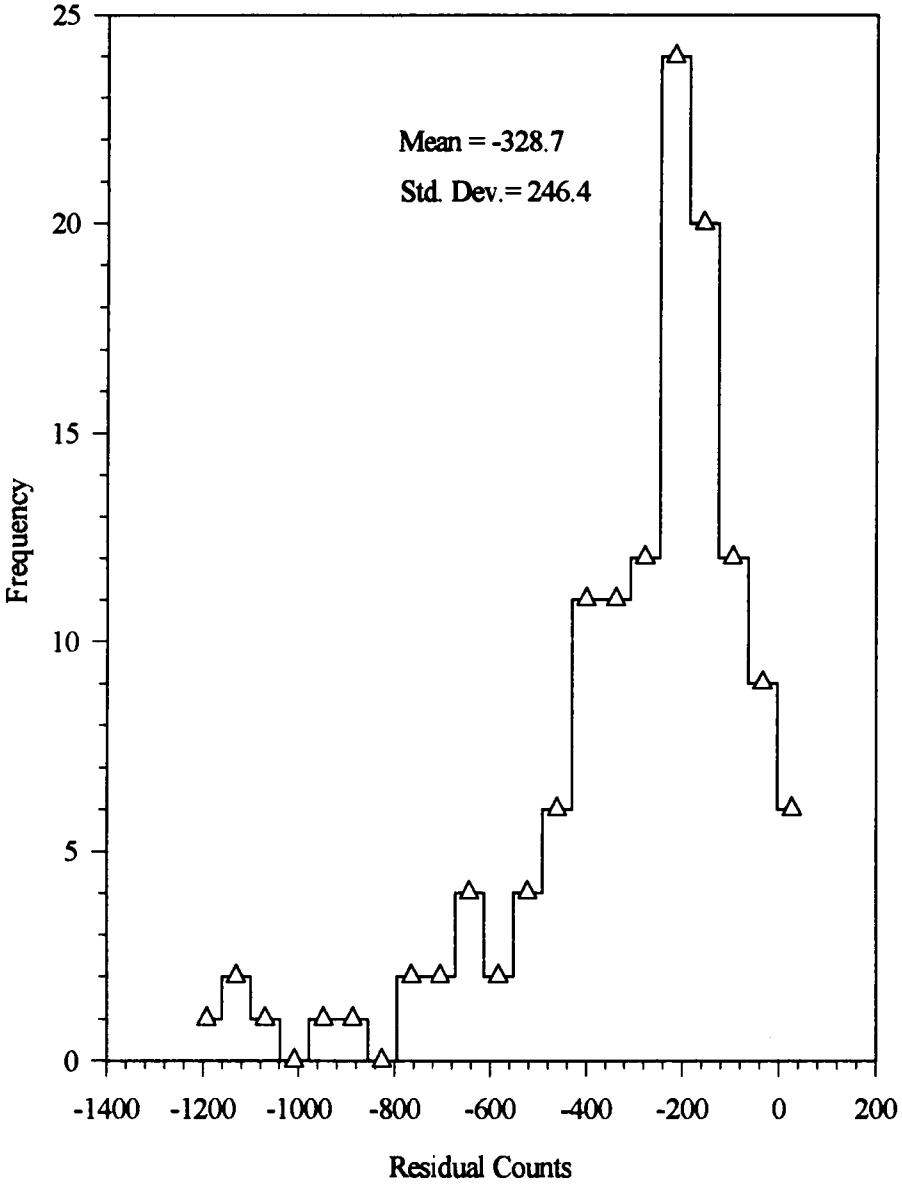


Figure 5.3.1. Residual distribution in ^{239}Pu ROI following application of Canberra's algorithm.

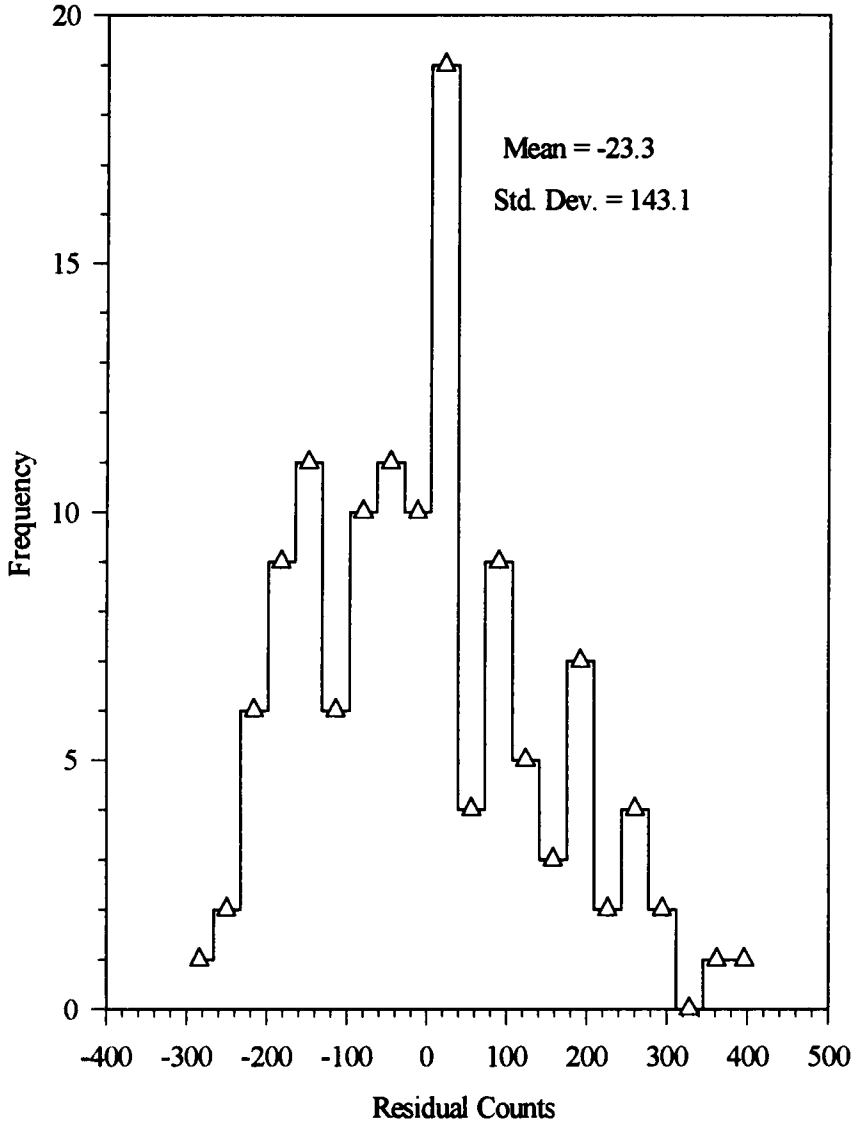


Figure 5.3.2. Residual distribution in ^{239}Pu ROI following application of gamma functions to describe each peak.

standard deviation of the predicted counts in the background spectra from the application of both chronic release algorithms to each of the twelve ROIs. When only background is present, Canberra's algorithm produced less accurate results than describing the spectrum as a superposition of gamma functions.

Canberra's chronic release algorithm produced a residual distribution with a mean of 718.5 and standard deviation of 271.6 and the second chronic release algorithm produced a residual distribution with a mean of 1331 and standard deviation of 176. Tables 5.3.4 and 5.3.5 summarize the results from both chronic release algorithms for all twelve transuranics and ROIs. The "added counts" column in these tables are the number of counts added to each spectrum to simulate a concentration of 8 DAC of the corresponding isotope for a one hour count cycle. Note that, Canberra's algorithm underestimated the amount of activity in the spectrum more than the algorithm that describes each spectrum as a superposition of gamma functions. Table 5.3.6 compares the counts predicted by each algorithm and presents the results as a percentage of the actual counts. The percentages in this table result from dividing the counts predicted by each algorithm by the added counts from tables 5.3.4 and 5.3.5. Notice that Canberra's algorithm predicts less than 75% of the counts that are due to transuranic activity in each ROI while the second chronic release algorithm predicts greater than 75% of the counts that are due to transuranic activity in each ROI.

The true measure of the precision for each algorithm is how often each produces a false alarm and how often each detects true transuranic activity. Due to the biases introduced in each algorithm by transuranic activity, both algorithms consistently underestimate the amount of activity that is present in the spectrum for a concentration equivalent to 8 DAC. Thus it is necessary to compare how each algorithm reacts to the alarm conditions defined by Eqs. 4.3.28 and 4.3.29. The critical level (L_c) defined by

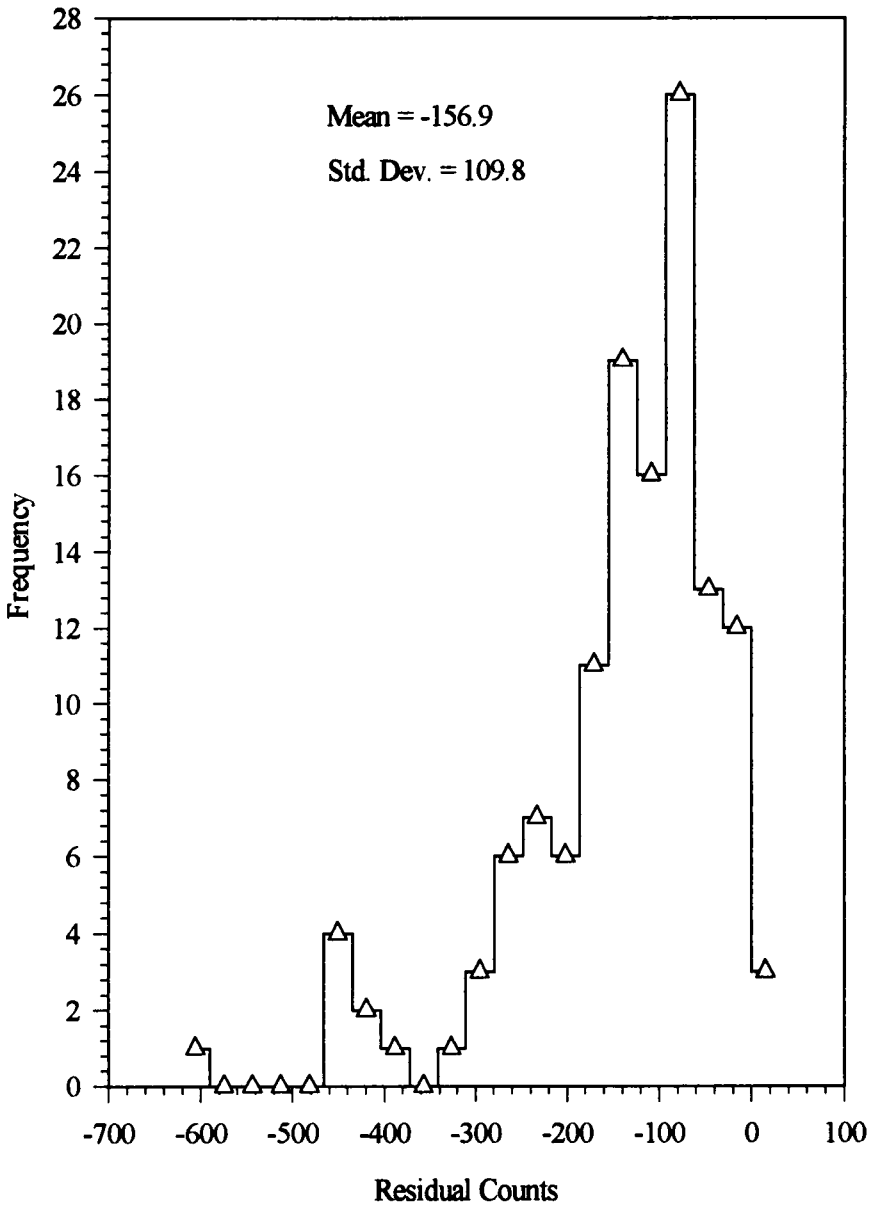


Figure 5.3.3. Residual distribution in ^{232}Th ROI following application of Canberra's algorithm.

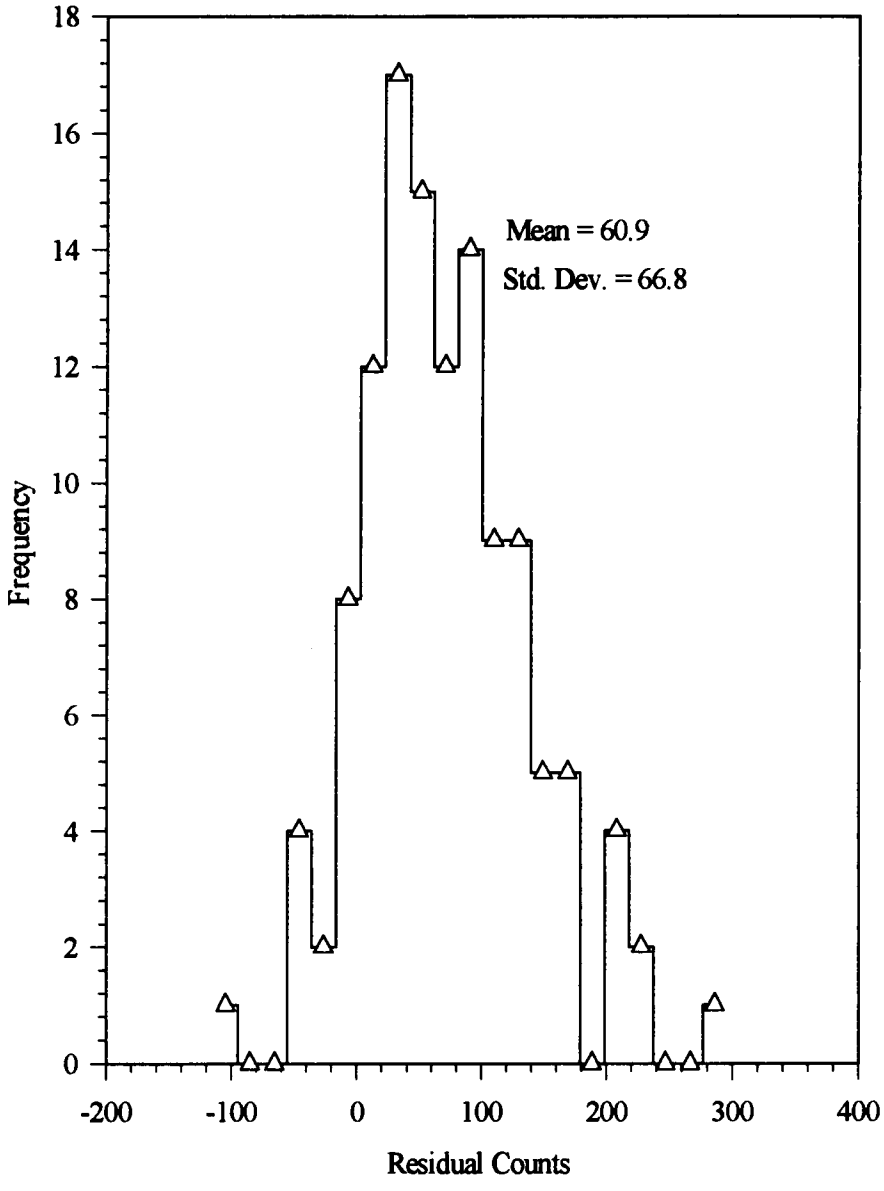


Figure 5.3.4. Residual distribution in ^{232}Th ROI following application of gamma functions to describe each peak.

Table 5.3.1. Residual mean, 95% CI, and standard deviation of the predicted counts for the spectra that contain only background counts (Canberra's chronic release algorithm).

Isotope	**Mean** *Canberra Algorithm*	**95% CI** *Canberra Algorithm*	**Std. Dev.** *Canberra Algorithm*
^{232}Th	-156.9	± 19.0	109.1
^{238}U	-199.0	± 24.0	139.1
^{235}U	-288.0	± 34.6	200.2
^{234}U	-275.9	± 35.3	204.6
^{237}Np	-275.9	± 35.3	204.6
^{242}Pu	-317.7	± 35.0	202.7
^{239}Pu	-328.7	± 42.6	246.4
^{243}Am	-343.1	± 43.0	248.5
^{232}U	-341.2	±42.5	245.8
^{228}Th	-365.5	± 47.0	271.7
^{241}Am	-397.3	± 56.0	309.3
^{238}Pu	-399.4	± 56.0	309.8

Table 5.3.2. Residual mean, 95% CI, and standard deviation of the predicted counts for spectra that contain only background counts (spectra are described by a superposition of gamma funcitons)

Isotope	**Mean** *Gamma Function*	**95% CI** *Gamma Function*	**Std. Dev.** *Gamma Function*
^{232}Th	60.89	± 11.9	66.83
^{238}U	68.02	± 12.4	80.86
^{235}U	69.01	± 19.6	106.88
^{234}U	51.75	± 22.4	117.60
^{237}Np	51.75	± 22.4	117.60
^{242}Pu	32.22	± 24.9	127.12
^{239}Pu	-16.98	± 30.6	139.13
^{243}Am	-52.86	± 34.1	151.57
^{232}U	-69.27	± 35.5	157.00
^{228}Th	-113.68	± 34.4	193.99
^{241}Am	-134.25	± 36.3	158.18
^{238}Pu	-134.25	± 36.3	158.20

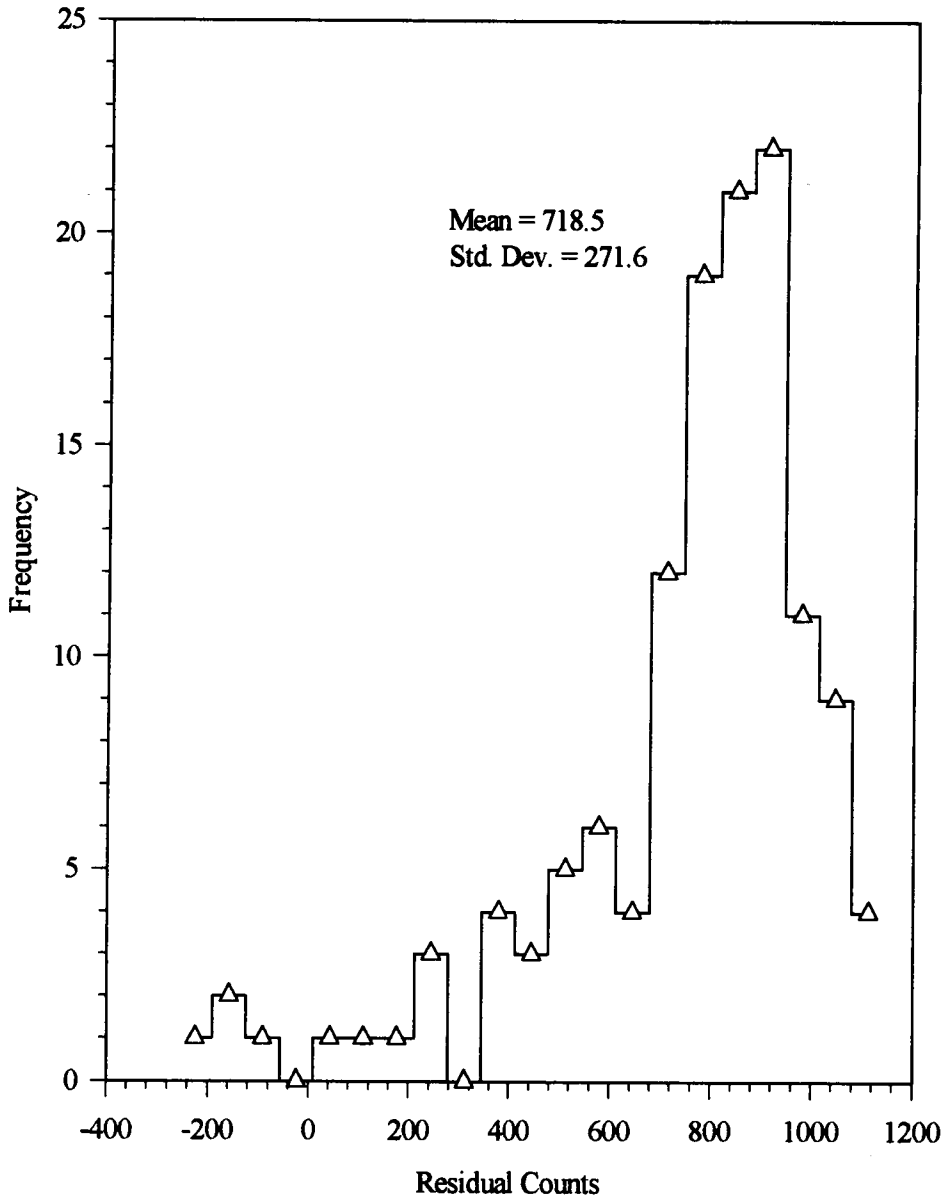


Figure 5.3.5. Residual distribution in ^{239}Pu ROI following application of Canberra's algorithm (concentration = 8 DAC of ^{239}Pu).

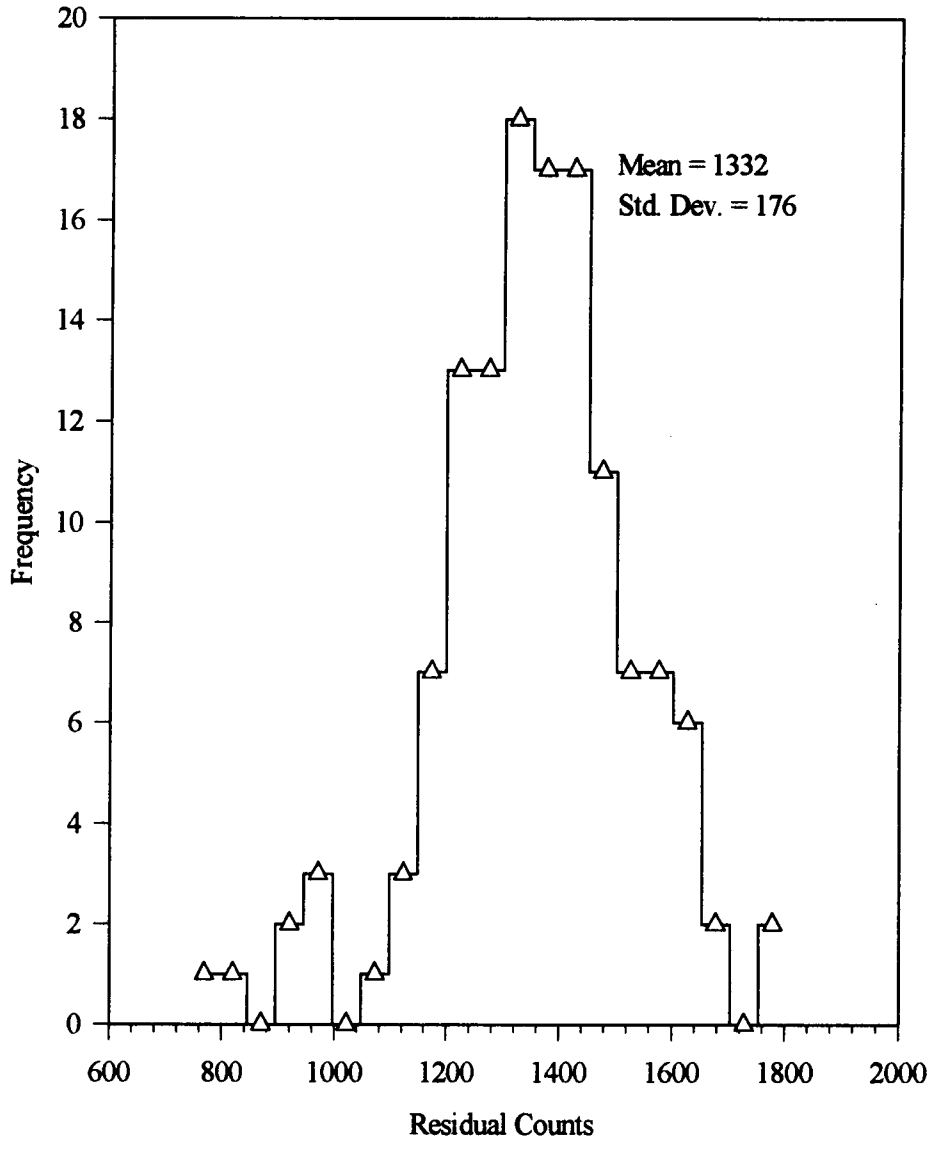


Figure 5.3.6. Residual distribution in ^{239}Pu ROI following application of algorithm that describes each background peak as a gamma function (concentration = 8 DAC of ^{239}Pu).

Table 5.3.3. Residual mean, 95 % CI, and standard deviation produced by Canberra's chronic release algorithm (concentation = 8 DAC).

Isotope	**Added Counts**	**Mean** *Canberra Algorithm*	**95 % CI** *Canberra Algorithm*	**Std. Dev.** *Canberra Algorithm*
^{232}Th	399	46.1	± 19.6	113.6
^{238}U	13968	9688.8	± 105.0	607.6
^{235}U	11968	8693.6	± 101.6	587.7
^{234}U	11968	8764.0	± 98.1	567.6
^{237}Np	1477	678.4	± 39.5	228.6
^{242}Pu	1796	852.5	± 41.6	240.6
^{239}Pu	1600	718.5	± 47.0	271.6
^{243}Am	1600	713.2	± 47.4	274.1
^{232}U	1996	998.1	± 49.0	283.6
^{228}Th	3992	2455.0	± 64.0	370.0
^{241}Am	1600	647.1	± 60.1	347.5
^{238}Pu	1796	817.3	± 58.3	337.5

Table 5.3.4. Residual mean, 95% CI, and standard deviation produced when the spectra are described as a superposition of gamma funcitons (concentration = 8 DAC).

Isotope	**Added Counts**	**Mean** *Gamma Function*	**95% CI** *Gamma Function*	**Std. Dev.** *Gamma Function*
^{232}Th	399	348.62	± 11.8	68.32
^{238}U	13968	10809	± 13.8	79.9
^{235}U	11968	9802	± 18.2	105.4
^{234}U	11968	10167	± 20.6	119.0
^{237}Np	1477	1282.9	± 22.1	127.7
^{242}Pu	1796	1569.93	± 24.9	144.05
^{239}Pu	1600	1332	± 30.6	176.8
^{243}Am	1600	1288.25	± 34.1	197.2
^{232}U	1996	1613.5	± 35.5	205.6
^{228}Th	3992	3263	± 44.5	257.3
^{241}Am	1600	1201.7	± 36.3	210.1
^{238}Pu	1796	1373.5	± 36.3	210.1

Table 5.3.5. Percentage of the actual activity that each chronic release algorithm predicts.

Isotope	Percent of added activity predicted by Canberra's algorithm	Percentage of added activity predicted by gamma functions
^{232}Th	11.6%	87.4%
^{238}U	69.4%	77.4%
^{235}U	72.6%	81.9%
^{234}U	73.2%	84.5%
^{237}Np	45.9%	86.9%
^{242}Pu	47.5%	87.4%
^{239}Pu	44.9%	83.3%
^{243}Am	44.6%	80.5%
^{232}U	50.0%	80.8%
^{228}Th	61.5%	81.7%
^{241}Am	40.4%	75.1%
^{238}Pu	45.5%	76.5%

Eq. 4.3.14 for both algorithms and are evaluated at the 95% confidence level. The standard deviation used for the critical is Eq. 4.3.13 for Canberra's algorithm and Eq. 4.5.2 for the second chronic release algorithm. All exposures are calculated using Eq. 4.3.27. Figures 5.3.7 and 5.3.8 illustrate the difference in the calculated critical levels and calculated exposures between the two algorithms. These figures contain only background counts and the ROI is ^{239}Pu. Due to the technique in which Canberra's algorithm calculates the standard deviation (Eq. 4.3.12), the critical level for their chronic release algorithm was much higher than the critical of the second chronic release algorithm.

Since both algorithms underestimate the number of counts in the spectrum due to transuranic activity, few alarms are produced when the user defined level (L_A of Eqs. 4.3.28 and 4.3.29) is set at 8 DAC-hrs and the activity added to the spectrum equals 8 DAC. Therefore, the alarm frequency was tested against three user defined levels, 8 DAC-hrs, 6 DAC-hrs, and 4 DAC-hrs. Canberra's chronic release algorithm produced 0 false alarms for L_A = 8 DAC-hrs, 0 false alarms for L_A = 6 DAC-hrs, and 1 false alarm for L_A = 4 DAC-hrs. The false alarm that occurred at the user defined level of 4 DAC-hrs was for the ^{232}Th ROI. The chronic release algorithm that describes the spectrum as a superposition of gamma functions produced 0 false alarms for L_A = 8 DAC-hrs, 0 false alarms for L_A = 6 DAC-hrs, and 5 false alarms for L_A = 4 DAC-hrs. The false alarms that occurred at the user defined level of 4 DAC-hrs was, again, from the ^{232}Th ROI. However, results between the two algorithms are quite different when a concentration equivalent to 8 DAC is added to each spectrum. Since Canberra uses two alarm criteria, Eqs 4.3.28 and 4.3.29, tables 5.3.6 and 5.3.7 present the number of alarms produced at each user defined level and the criteria that produced each alarm.

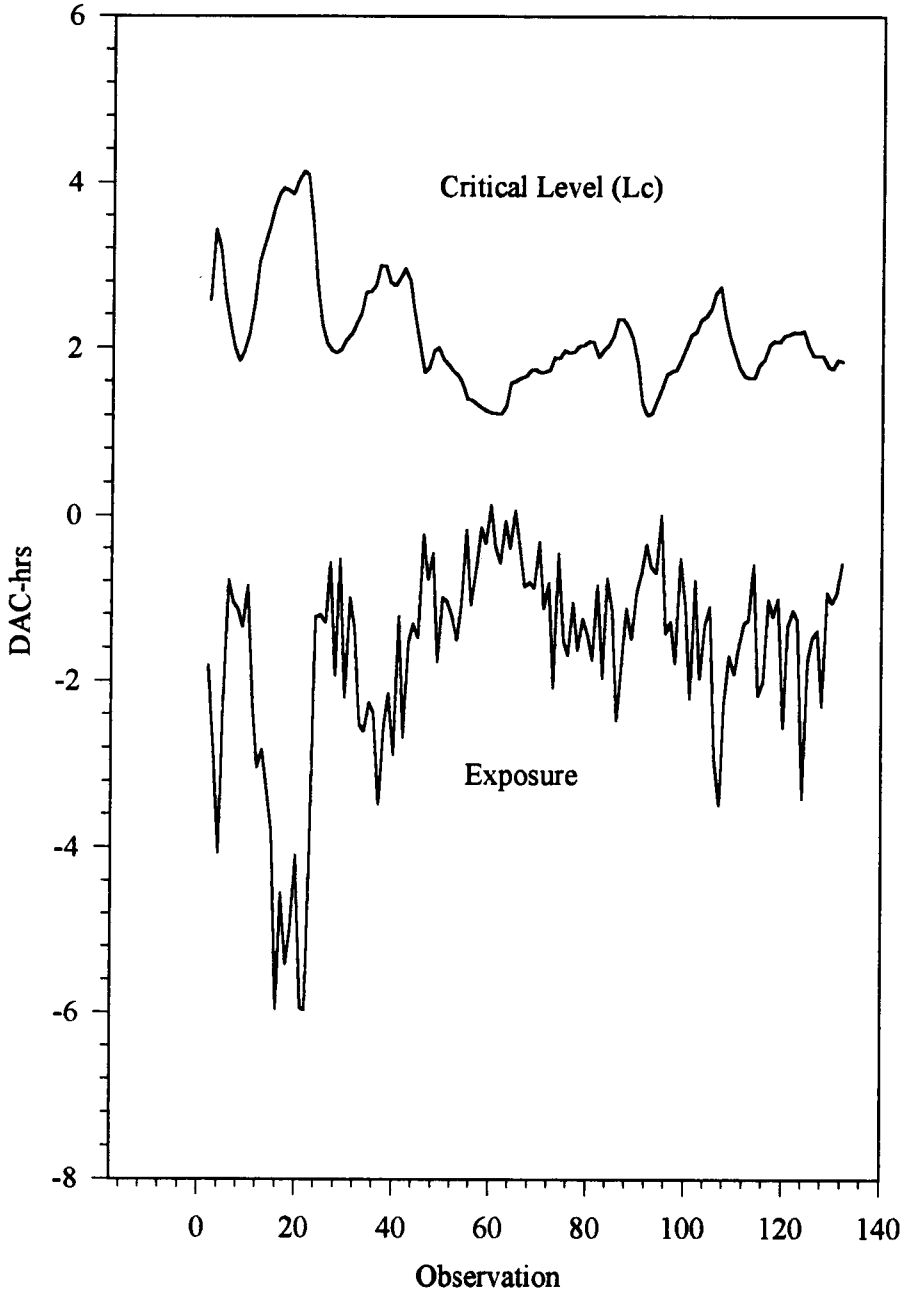


Figure 5.3.7. Critical level (L_c) and exposure produced by Canberra's algorithm (^{239}Pu ROI).

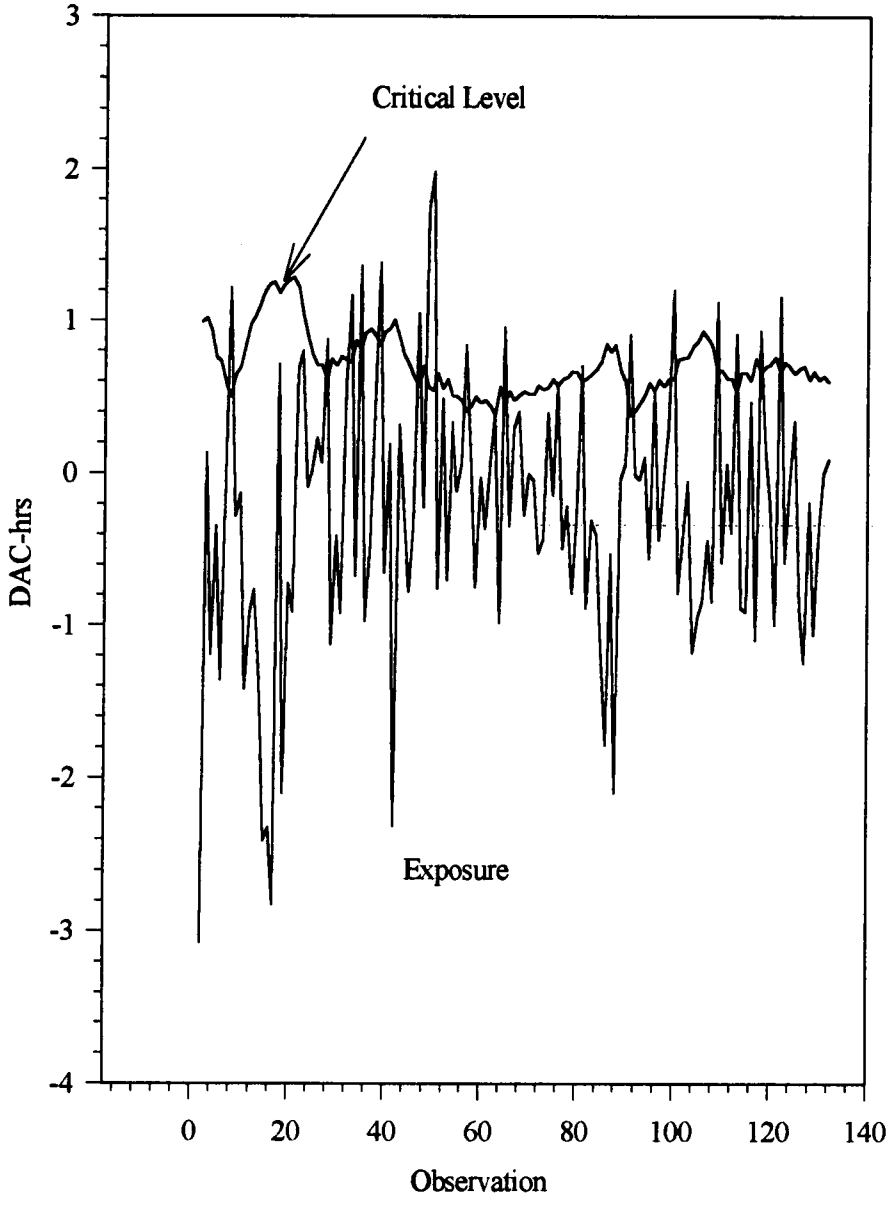


Figure 5.3.8. Critical level (L_c) and calculated exposure for the chronic release algorithm that describes the spectrum as a superposition of gamma functions (^{239}Pu ROI).

Neither algorithm produced many alarms for L_A = 8 DAC-hrs, but when L_A = 6 DAC-hrs the algorithm that describes the spectra as a superposition of gamma functions produced many more alarms than the Canberra algorithm. In fact, when L_A = 6 DAC-hrs Canberra's algorithm only alarmed for 4 transuranic ROI's, but the second algorithm alarmed for the all the transuranic ROI's. From Tables 5.3.6 and 5.3.7 it is apparent that Canberra's algorithm produced far fewer alarms than when the spectra were described as a superposition of gamma functions.

Table 5.3.6. Alarms produced by Canberra's algorithm for a concentration equal to 8 DAC.

Isotope	$L_A = 8$ Eq. 4.3.28	$L_A = 8$ Eq. 4.3.29	$L_A = 6$ Eq. 4.3.28	$L_A = 6$ Eq. 4.3.29	$L_A = 4$ Eq. 4.3.28	$L_A = 4$ Eq. 4.3.29
^{232}Th	0	30	0	84	0	97
^{238}U	0	0	12	0	131	0
^{235}U	0	0	41	0	131	0
^{234}U	0	0	49	0	131	0
^{237}Np	0	0	0	0	65	3
^{242}Pu	0	0	0	0	66	0
^{239}Pu	0	0	0	0	58	1
^{243}Am	0	0	0	0	57	2
^{232}U	0	0	0	0	77	0
^{228}Th	0	0	2	0	116	0
^{241}Am	0	0	0	0	53	0
^{238}Pu	0	0	0	0	66	0

Table 5.3.7. Alarms produced when spectra are described as a superposition of gamma functions for a concentration equal to 8 DAC.

Isotope	$L_A = 8$ Eq. 4.3.28	$L_A = 8$ Eq. 4.3.29	$L_A = 6$ Eq. 4.3.28	$L_A = 6$ Eq. 4.3.29	$L_A = 4$ Eq. 4.3.28	$L_A = 4$ Eq. 4.3.29
^{232}Th	30	0	103	0	130	0
^{238}U	0	0	131	0	131	0
^{235}U	0	0	131	0	131	0
^{234}U	0	0	131	0	131	0
^{237}Np	10	0	121	0	131	0
^{242}Pu	8	0	125	0	131	0
^{239}Pu	9	0	109	0	130	0
^{243}Am	6	0	94	0	129	0
^{232}U	2	0	101	0	130	0
^{228}Th	0	0	114	0	131	0
^{241}Am	1	0	74	0	124	0
^{238}Pu	1	0	80	0	126	0

6. CONCLUSIONS

The results of this analysis reveal several conclusions concerning the ability of this CAM sampler to detect airborne transuranics and the ability of the algorithms to detect airborne transuranics:

- Radon reduction screens are highly effective in removing fresh radon progeny, however, fresh radon progeny constitute approximately only 3% of the total indoor concentration of radon progeny.
- By attenuating fewer α particles, membrane filters produce a higher resolution energy spectrum than do cellulose filters. The Floropore 5 μm membrane filter used in this study produces a spectrum with an energy resolution great enough to differentiate between the radon progeny.
- The acute release alarm parameter suggested by the technical documentation is higher than necessary which results in a decrease in acute release alarm sensitivity.
- Both chronic release algorithms are negatively biased which results in an underestimation of transuranic activity when it is present. However, when the spectra are described as a superposition of gamma funcitons the bias is less than when using Canberra's chronic release algorithm. In fact, describing the spectra as a superposition of gamma functions more accurately predicts the activity of each transuranic than does Canberra's chronic release algorithm.
- The algorithm developed in this study uses a more acurate measure of statistical uncertainty than does Canberra's algorithm which improves the calculation of the lower limit of detection.
- The algorithm developed by this study was capable of consistently producing alarms when the concentration of any transuranic reach 8 DAC. Canberra's chronic release

algorithm was capable of producing alarms at this level of activity, but the consitency was less than when using the algorithm developed by this study.

There are many opportunities for continued work in this area including:

- Improvements to the algortihm in the form of a more sophisticated convergence routine for each parameter of the gamma function.
- A study to analyze how the algorithms perform in higher and lower background conditions than those conditions used in this study.
- A study of the effects that true transuranic activity distribution has on the capabilities of the chronic release algorithms.
- A study that correlates environmental conditions (such as temperature and humidity) with the attenuation of α particles in the spectrum.

This study has shown that this CAM sampler is capable of detecting airborne transuranics by approximating the contribution of radon progeny to the spectrum. Although the instrument is capable of alarming at the 8 DAC-hr exposure level, opportunities exist to improve the algorithms presently employed in the instrument. However, the continuous air monitoring program at Oak Ridge National Laboratory would benefit if the current air monitors were replaced with the ASM 1000.

BIBLIOGRAHY

BIBLIOGRAPHY

Altshuler, B.; Pasternack, B., 1962 "Statistical Measures of the Lower Limit of Detection of a Radioactive Counter", *Health Physics* 9, 293.

Busigin A.; van der Vooren A. W.; Phillips C. R., 1981 "The Nature of Unattached RaA (^{218}Po) Particles", *Health Physics* 40, 333.

Busigin A.; van der Vooren A. W.; Phillips C. R., 1981 "An Evaluation of Unattached Radon (And Thoron) Daughter Measurement Techniques", *Health Physics* 42, 801.

Canberra Industries, Inc. (1992). ASM 1000 Technical Documentation.

Canberra Industries, Inc. (1994). Instruments Catalog. (9th ed.).

Fry R. M., 1976, "Radon and its Hazards", *Proceedings of the NEA Specialist Meeting*, Elliot Lake, Canada, 4 - 8 Oct.

Hoover, M. D.; Newton G. J., 1993, "Evaluation Of Filter Media For Alpha `Continuous Air Monitoring: Updated Test Results".

International Commission on Radiological Protection. Lung cancer risk from indoor exposure to radon daughters, Oxford: Pergamon Press; ICRP Publication 50; Ann. of ICRP 17:1-60; 1987.

Knoll, G.F. (1989). Radiation Detection and Measurement New York: John Wiley & Sons.

Mayer, D.; Dauer, L., 1992 "Application of Systematic Error Bounds To Detection Limits for Practical Counting", *Health Physics* 65, 89.

McFarland, A.R.; Rodgers, J.C.; Ortiz, C.A.; Moore, M.E., 1992 "A Continuous Samper With Background Suppression For Monitoring Alpha-Emitting Aerosol Particles", *Health Physics* 62, 75.

Moore, M.E.; McFarland, A.R.; Rodgers, J.C., 1992 "Factors That Affect Alpha Particle Detection In Continuous Air Monitor Applications", *Health Physics* 65, 69.

Nuclear Energy Agency Group of Experts. Dosimetry aspects of exposure to radon and thoron daughter products. Paris: NEA; Report NEA/OECD; 1983.

Raabe O. G., 1968, "Measurement of the Diffusion Coefficients of RaA", *Nature* 217, 1143.

Reineking A. and Porstendorfer J., 1990 ""Unattached" Fraction of Short-Lived Rn Decay Products In Indoor and Outdoor Environments: An Improved Single-Screen Method and Results", *Health Physics* 58, 715.

Shleien, B. (1986). The Health Physics and Radiological Health Handbook. Silver Spring: Scinta.

Table Curve. Vers. 2.0. Jandel Scientific Software. 1994,

APPENDICES

APPENDIX A

Source Code Used to Simulate Canberra's Algorithms

```
//
//


#include <stdio.h>
#include <stdlib.h>
#include <conio.h>
#include <math.h>
#include <string.h>

#define distance1 42
// distance 1 is the number of channels the 6.05 peak lies below the 7.68 peak


//*********************************************************************
*****
//
//   Function Prototypes
//*********************************************************************
*****
void AddContamination(int start, int stop, float ratio[60], int k);
void fitSpectrum();
float spectrum_sum(float spectrum[256],float  low_channel);
double SolveIntercept(float x1, float y1, double b);
float peakfinder(float spectrum[256]);
float ecal(int peak);
float peak_summer(float contamination_peak, int peak, float spectrum[256]);
double SolveSlope(float x1, float x2, float y1, float y2);
float sum_counts(float high_channel, float low_channel, float spectrum[256]);
//End function prototypes
//*********************************************************************
*****
struct peakFit {
        float rROI;
        float BKGD;
        float STDV;
        };

peakFit radionuclide_fit[12];

float sum;
float valley1;
```

```
float valley2;
float valley3;
float x1;
//float *AllSpectrum[70];
double spectrum2[256];

float ratio[60]= {0.0103, 0.0269, 0.0396, 0.0467, 0.0463, 0.0420, 0.0389,
                  0.0385, 0.0337, 0.0323, 0.0296, 0.0276, 0.0264, 0.0226,
                  0.0218, 0.0239, 0.0198, 0.0191, 0.0189, 0.0187, 0.0178,
                  0.0161, 0.0152, 0.0151, 0.0128, 0.0138, 0.0146, 0.0125,
                  0.0111, 0.0114, 0.0116, 0.0102, 0.0106, 9.3492e-3,
                  8.7199e-3, 8.2704e-3, 8.9446e-3, 8.1805e-3, 7.2816e-3,
                  6.5624e-3, 7.0568e-3, 7.6411e-3, 6.5624e-3, 5.3488e-3,
                  5.0342e-3, 7.0568e-3, 6.2927e-3, 4.4049e-3, 4.9443e-3,
                  5.3488e-3, 5.0342e-3, 4.9443e-3, 4.4049e-3, 4.1352e-3,
                  4.4498e-3, 4.4948e-3, 4.3150e-3, 4.1802e-3, 3.4610e-3,
                   4.4498e-3};

float energy;
float low_energy;
float bkupspectrum[256];
float spectrum[256];
float peak;
float intercept;
float contamination_peak;

float Bismuth_peak;

int count_to_low;
main()
{


char outputfilename[40];
sprintf(outputfilename, "c:\\thesis\\code\\data.fit");
FILE *exportFILE = fopen(outputfilename, "w");

for(int i=0; i<150; i++)
{


char currentfile[40]=" ";
        sprintf(currentfile, "c:\\cam4\\cansim\\one_hour\\a1$%i", i);
```

```
FILE *fp = fopen(currentfile, "r");

        if(fp)
        {
         for(int j1=0; j1<256; j1++)
                {
                 float count;
                 fscanf(fp, "%f", &count);
                 spectrum[j1] = bkupspectrum[j1] = count;
                }
                fclose(fp);

                printf("fittingSpectrum %s  \r", currentfile);

                fitSpectrum();

                if(exportFILE)
                {
                        for(int k1=0; k1<12; k1++)
                        {
                                fprintf(exportFILE, "%f %f %f\n",
                                radionuclide_fit[k1].rROI, radionuclide_fit[k1].BKGD,
                                radionuclide_fit[k1].STDV);
                        }
                }
         }
        }
         if(fclose(exportFILE));
        }// END of MAIN;

void fitSpectrum(void)
{


                        for(int ctr=0;ctr<12;ctr++)  //MAIN counter for analysis (each
radionuclide)
        {

        radionuclide_fit[ctr].BKGD = 0;
        radionuclide_fit[ctr].rROI = 0;
        radionuclide_fit[ctr].STDV = 0;
```

```
float radionuclideEnergy[12] = {
4.01,   /* Th232 */
4.2,    /* U238 */
4.58,   /* U235 */
4.77,   /* U234 */
4.77,   /* Np237 */
4.9,    /* Pu242 */
5.16,   /* Pu239 */
5.28,   /* Am243 */
5.32,   /* U232 */
5.43,   /* Th228 */
5.49,   /* Am241 */
5.5     /* Pu238 */
};

        for(int jk = 0; jk<256; jk++)
        {
        spectrum[jk] = bkupspectrum[jk];
        }

energy = radionuclideEnergy[ctr];

peak = peakfinder(spectrum);  // peak represents the CHANNEL NUMBER
//that contains the 7.68 peak.

        intercept = ecal(peak);

        contamination_peak = (energy-intercept)/.0392;


        // contamination_peak will contain the energy channel of the
        //contamination peak

        float low_channel = contamination_peak - 50;
        if (low_channel <40) low_channel = 40;

 // ROIstart and ROIstop reflect Gamma use of recoded spectrum
 int ROIstart = low_channel;
 int ROIstop  = contamination_peak + 3 ;


//              AddContamination(ROIstart, ROIstop, ratio, ctr);
```

```
Bismuth_peak = peak-distance1;

float spectrum_end = 256;

valley3 = peak+5;  // valley3 is the 7.68/8.78 valley
valley2 = Bismuth_peak + 6;
valley1 = contamination_peak + 5;

float denominator = spectrum_sum(spectrum, low_channel);

float counts878 = sum_counts(spectrum_end-1, valley3, spectrum);
float counts768 = sum_counts(valley3-1, valley2, spectrum);
float counts605 = sum_counts(valley2-1, valley1, spectrum);

float average_valley1 = sum_counts(valley1+2, valley1-2, spectrum);
float average_valley2 = sum_counts(valley2+2, valley2-2, spectrum);
float average_valley3 = sum_counts(valley3+2, valley3-2, spectrum);

//float total_valley = average_valley1 + average_valley2 +
average_valley3;

sum=0;
        for(int ct=0;ct<5;ct++)
        {
                sum+=spectrum[low_channel-2+ct];
        }



float low_energy_average878 = (counts878/denominator)*sum/5;
float low_energy_average768 = (counts768/denominator)*sum/5;
float low_energy_average605 = (counts605/denominator)*sum/5;



        float high_energy_average878 = average_valley3/5;
        float high_energy_average768 = average_valley2/5;
        float high_energy_average605 = average_valley1/5;
```

```
double slope878 = SolveSlope(low_channel, valley3, low_energy_average878,
high_energy_average878);
double avalue878 = SolveIntercept(valley3, high_energy_average878, slope878);


double slope768 = SolveSlope(low_channel, valley2, low_energy_average768,
high_energy_average768);
double avalue768 = SolveIntercept(valley2, high_energy_average768, slope768);


double slope605 = SolveSlope(low_channel, valley1,low_energy_average605,
high_energy_average605);
double avalue605 = SolveIntercept(valley1, high_energy_average605, slope605);



        for(int k=low_channel;k<peak+5;k++)
        {
        x1 = k;
        spectrum[k] -= exp(avalue878+slope878*x1);
        }




        //counts768 =  sum_counts(valley3-1, valley2, spectrum);

        //float integral768 = counts768;


        for(k=low_channel;k<valley2;k++)
        {
        x1 = k;

        spectrum[k]-= exp(avalue768+slope768*x1);
        }

//*****************************************************************************
*********

        for(k=low_channel;k<valley1;k++)
        {
        x1 = k;
```

```
spectrum[k] -= exp(avalue605+slope605*x1);
}



//counts605 = sum_counts(valley2-1, valley1, spectrum);

//float integral605 = counts605;
float integral605 = 0;
float integral768 = 0;
float integral878 = 0;

for (int z1=low_channel; z1<valley1; z1++)
{
radionuclide_fit[ctr].BKGD += exp(avalue605+slope605*z1)+
exp(avalue768 + slope768*z1) + exp(avalue878 +slope878*z1);
radionuclide_fit[ctr].rROI += spectrum[z1];
}


for(z1=low_channel; z1<valley1; z1++)
{
integral605+= exp(avalue605 + slope605*z1);
}
for(z1=low_channel; z1<valley2; z1++)
{
integral768+= exp(avalue768 + slope768*z1);
}
for(z1 = low_channel; z1<valley3; z1++)
{
integral878 += exp(avalue878 +slope878*z1);
}

float N605 = integral605;
float N768 = integral768;
float N878 = integral878;

for(z1 = valley3; z1<256; z1++)
{
N878 += spectrum[z1];
}
for(z1 = valley2; z1< valley3; z1++)
```

```
        {
        N768 += spectrum[z1];
        }
        for(z1 = valley1; z1< valley2; z1++)
        {
        N605 += spectrum[z1];
        }
 radionuclide_fit[ctr].STDV = sqrt(radionuclide_fit[ctr].BKGD + N605 + N768 +
N878);


        }

 } // END of MAIN LOOP




//*************************************************************************
****
//
//                        Peakfinder
// function will return CHANNEL of 7.68 peak
//
//*************************************************************************
****
float peakfinder(float spectrum[256])
{

int ctr1;
float  sum1, peak, peak_counts;
sum1 =0;
ctr1=175;
peak = 169;
peak_counts =(spectrum[169]+spectrum[168]+spectrum[167]);
for(ctr1=175;ctr1>165;ctr1--)
{
sum1 = spectrum[ctr1]+spectrum[ctr1-1]+spectrum[ctr1+1];
        if(sum1>(peak_counts+(10))){
        peak = ctr1;
```

```
        peak_counts = sum1;
        }
        }
        return(peak);
        }

//
**********************************************************************
***
//
//              ECAL
//      perform energy calibration
//
//**********************************************************************
****

float ecal(int peak)
{
float axis, intercept;

        axis = peak*.0392;
        intercept = (7.68-axis);
        return(intercept);
}

//**********************************************************************
*****
//
//                                      PEAK_SUMMER
//
// function returns the number of counts from the end of the contamination
// region to the top of the 6.05 peak
//**********************************************************************
****
float peak_summer(float contamination_peak, int peak, float spectrum[256])

{
int ctr, start, finish;
float sum;
sum = 0;

start = contamination_peak +6;
finish = peak-distance1;
```

```
ctr=start;
for(ctr=start;ctr<=finish;ctr++)
{
sum = spectrum[ctr] +sum;
}
        if(sum == 0) sum = .00001;
        if(sum < 0) exit(-1);
return(sum);
}
```

```
//*********************************************************************
**********


//
**********************************************************************
*
//
//                  Function of find b coefficient of the following equation
//        ln(y) = a + b*x^2
//
//

double SolveSlope(float x1, float x2, float y1, float y2)
{

        double b;

         if(y1<=0) y1 = 1;
         if(y2<=0) y2 = 1;

         b = (log(y1) - log(y2))/((x1)-(x2));


        return(b);

}
```

```
double SolveIntercept(float x1, float y1, double b)
{
        double a;

        if(y1<=0) y1 = 1;
         a = log(y1) - b*x1 ;
        return(a);
}

//Sum counts in spectrum
float spectrum_sum(float spectrum[256],float low_channel)
        {

        float denominator = 0;
        for(int i=low_channel;i<256;i++)

        {
        denominator+=spectrum[i];
        }

        return(denominator);
        }



float sum_counts(float high_channel, float low_channel, float spectrum[256])
        {
        float sum = 0;

        for(int i=low_channel;i<=high_channel;i++)
        {
        sum+= spectrum[i];
        }

        return(sum);
        }

void AddContamination(int start, int stop, float ratio[60], int k)
{

        static int tries[12];

                float counts[12]={
```

```
                49.9,      /* Th232 */
                1746.4,          /* U238 */
                1496.9,          /* U235 */
                1496.9,          /* U234 */
                184.6,  /* Np237 */
                224.5,  /* Pu242 */
                199.6,  /* Pu239 */
                199.6,  /* Am243 */
                249.5,  /* U232 */
                499.0,  /* Th228 */
                199.6,  /* Am241 */
                224.5   /* Pu238 */
                };


        tries[k]=8;

                int j = 0;
         for(int i=start; i<stop; i++)
         {
         spectrum[i] += counts[k]*tries[k]*ratio[j];
         j++;
         }
}
```

Appendix B

Source Code That Represent Each Spectrum as a Superposition of Gamma Functions

```
#include <stdio.h>
#include <math.h>
#include <stdlib.h>
#include <string.h>


struct peakFit {
        int start;
        int stop;

        float rROI;
        float BKGD;
        float r;
        float a; // peak height
        float b; // peak channel
        float c; // full width half max
        float d; // suggested by TBLCURVE
};



int cSteps = 100;
int dSteps = 100;
float cStep = (30-6)/(float)cSteps;
float dStep = (1.1 - 1.0001)/(float)dSteps;

struct radionuclideDependency {
        float rROI;
        float r6MeV, a6MeV, b6MeV, c6MeV, d6MeV;
};



// function prototypes
void AddContamination(int start, int stop, float ratio[60], int k);

void fitnuclide(peakFit *fit);
void fitSpectrum(void);

void Gamma(peakFit *fit, float cValue, float dValue, float y[256]);
void GammaF(peakFit *fit, int start, int stop, float y[256]);

float peakfinder(float spectrum[256]);
```

```
void straightLine(peakFit *fit, int ROIstart, float data[256], float y[256]);



float channelwidth = .0392;   // defined by Canberra
float endgamma[256];
float spectrum[256];          // Canberra ASM1000 raw data, 10MeV/256
float rspectrum[256];         // gamma fit uses recoded spectrum
float CCrspectrum[256];

float Fspectrum[16][256];     // GammaFunction evaluation
float Dspectrum[12][256];     // Difference  rspectrum - (Po212+Po214+Bi600)


float Po214_768;              // channel number
float Po212_878;              // channel number

float ratio[60]= {0.0103, 0.0269, 0.0396, 0.0467, 0.0463, 0.0420, 0.0389,
                  0.0385, 0.0337, 0.0323, 0.0296, 0.0276, 0.0264, 0.0226,
                  0.0218, 0.0239, 0.0198, 0.0191, 0.0189, 0.0187, 0.0178,
                  0.0161, 0.0152, 0.0151, 0.0128, 0.0138, 0.0146, 0.0125,
                  0.0111, 0.0114, 0.0116, 0.0102, 0.0106, 9.3492e-3,
                  8.7199e-3, 8.2704e-3, 8.9446e-3, 8.1805e-3, 7.2816e-3,
                  6.5624e-3, 7.0568e-3, 7.6411e-3, 6.5624e-3, 5.3488e-3,
                  5.0342e-3, 7.0568e-3, 6.2927e-3, 4.4049e-3, 4.9443e-3,
                  5.3488e-3, 5.0342e-3, 4.9443e-3, 4.4049e-3, 4.1352e-3,
                  4.4498e-3, 4.4948e-3, 4.3150e-3, 4.1802e-3, 3.4610e-3,
                  4.4498e-3};

peakFit Po212fit;
peakFit Po214fit;
peakFit Bi212fit;
peakFit radionuclide_fit[12];


main()
{

// input files                  output file "curvefit"
//                              ROI    6MeV     7.68MeV   8.78MeV
//                              resid  r,a,b,c,d r,a,b,c,d r,a,b,c,d
// a1$0          time 0
```

```
// a1$1          time 0+1hr
// a1$2          time 1+1hr
// .
// .
// .
// a1$150


        char outputfilename[40];
                sprintf(outputfilename,
//                      "f:\\borlandc\\projects\\canberra\\data\\spectrum.fit");
                        "c:\\cam4\\results3\\conline2.fit");

        FILE *exportFILE = fopen(outputfilename, "w");



        for (int i=0; i <150 ; i++)
        {
                char currentfile[40] = " ";
//                      sprintf(currentfile, "a:\\data\\a1$%i", i);
                        sprintf(currentfile,
//                      "f:\\borlandc\\projects\\canberra\\data\\a1$%i", i);
                        "c:\\cam4\\cansim\\a1$%i", i);

                FILE *fp=fopen(currentfile, "r");

                if (fp)
                {
                 for (int j=0; j < 256; j++)
                 {
                        float count;
                        fscanf(fp, "%f", &count);
                        spectrum[j] = rspectrum[255-j] = CCrspectrum[255-j] = count;

                 }

                 fclose(fp);

                 printf("fittingSpectrum %s   \r", currentfile);
                 fitSpectrum();
```

```
                if (exportFILE)
                {
//                fprintf(exportFILE, "%s\r\n", tname);

                    fprintf(exportFILE, "%f %f %f %f %f %f\n",
                    Po212fit.r, Po212fit.BKGD, Po212fit.a, Po212fit.b, Po212fit.c,
Po212fit.d);

                    fprintf(exportFILE, "%f %f %f %f %f %f\n",
                    Po214fit.r, Po214fit.BKGD, Po214fit.a, Po214fit.b, Po214fit.c,
Po214fit.d);


                    for (int k=0; k < 12; k++)
                    {
                        fprintf(exportFILE, "%f %f %f %f %f %f\n",
                    radionuclide_fit[k].rROI, radionuclide_fit[k].BKGD,
                    radionuclide_fit[k].a, radionuclide_fit[k].b,
                    radionuclide_fit[k].c, radionuclide_fit[k].d);
                  }
                 }
               }
        }
        if (fclose(exportFILE))
          ; //fclose error
}


void fitSpectrum(void)
{
        //each spectrum is processed 14 times

        Po214_768 = peakfinder(spectrum);
        Po212_878 = Po214_768 + 28;

        // channels for Gamma evaluation using recoded spectrum, rspectrum
        Po212fit.start = 255 - 225;
        Po212fit.stop = 255 - (Po214_768 + 3);

        Po212fit.BKGD = 0;
        Po212fit.r = 1e10; // seek a better fit
        Po212fit.a = spectrum[Po212_878];
        Po212fit.b = Po212_878;
```

```
fitnuclide(&Po212fit);

GammaF(&Po212fit, 0, 256, &(Fspectrum[0][0]));

                for(int j=0; j<256; j++)
                {
                rspectrum[j] = rspectrum[j]- Fspectrum[0][j];
                }

Po214fit.start = 255 - (Po214_768 + 3);
Po214fit.stop = 255 - (Po214_768 - 39);

Po214fit.BKGD = 0;
Po214fit.r = 1e10; // seek a better fit
Po214fit.a = rspectrum[255 - Po214_768];
Po214fit.b = Po214_768;

fitnuclide(&Po214fit);
GammaF(&Po214fit, 0, 256, &(Fspectrum[1][0]));

                for(j=0; j<256; j++)
                {
                rspectrum[j] = rspectrum[j] - Fspectrum[1][j];
                CCrspectrum[j] = rspectrum[j];
                }
float Bi212_600 = Po214_768 - 42;

Bi212fit.start = 255-Bi212_600;
Bi212fit.stop  = 255-40;

Bi212fit.BKGD = 0;
Bi212fit.r = 1e10;
Bi212fit.a = rspectrum[255-Bi212_600];
Bi212fit.b = Bi212_600;


float radionuclideEnergy[12] = {
        4.01,   /* Th232 */
        4.2,    /* U238 */
        4.58,   /* U235 */
        4.77,   /* U234 */
        4.77,   /* Np237 */
```

```
        4.9,    /* Pu242 */
        5.16,   /* Pu239 */
        5.28,   /* Am243 */
        5.32,   /* U232 */
        5.43,   /* Th228 */
        5.49,   /* Am241 */
        5.5     /* Pu238 */
        };


for (int k=0; k < 12; k++)
{
 float contamination_peak =
        Po214_768 - ((7.68 - radionuclideEnergy[k]) / channelwidth);

 radionuclide_fit[k].start = Bi212fit.start;
 radionuclide_fit[k].stop  = Bi212fit.stop;


 Po212fit.rROI = 0;
 Po214fit.rROI = 0;
 radionuclide_fit[k].BKGD = 0;
 radionuclide_fit[k].rROI = 0;
 radionuclide_fit[k].r = 1e10; // seek a better fit
 radionuclide_fit[k].a = Bi212fit.a;
 radionuclide_fit[k].b = Bi212fit.b;
 radionuclide_fit[k].c = Bi212fit.c;
 radionuclide_fit[k].d = Bi212fit.d;

        float low_channel = contamination_peak - 49;
        if (low_channel <40) low_channel = 40;

 // ROIstart and ROIstop reflect Gamma use of recoded spectrum
 int ROIstart = 255 - ( contamination_peak + 3 );
 int ROIstop  = 255 - low_channel;

                                        //reset rspectrum
                                        for(int r = 0; r <256; r++)
                                        {
                                        rspectrum[r] = CCrspectrum[r];
                                        }
```

```
        AddContamination(ROIstart, ROIstop, ratio, k);


        fitnuclide(&radionuclide_fit[k]);

        GammaF(&radionuclide_fit[k],0,256, &(Fspectrum[2][0]));

                for(j=0; j<256; j++)
                {
                endgamma[j] = rspectrum[j]-Fspectrum[2][j];
                }


        straightLine(&Bi212fit, ROIstart, endgamma, &(Fspectrum[3][0]));

                for(j=0; j<256; j++)
                {
                endgamma[j]= endgamma[j] - Fspectrum[3][j];
                }


        // Difference defined as, rspectrum - (Po212+Po214+Bi600)
        for (int i=ROIstart; i < ROIstop; i++)
        {
                float difference = endgamma[i];

                Dspectrum[k][i] = difference;
                radionuclide_fit[k].rROI += difference;
                radionuclide_fit[k].BKGD += Fspectrum[0][i] + Fspectrum[1][i]
                                        + Fspectrum[2][i] +Fspectrum[3][i];
        }



        printf("Nuclide %i processed                    \r", k+1);
      }
}


void fitnuclide(peakFit *fit )
{
      int start = fit->start;
      int stop  = fit->stop;
```

```
        float cValue = 6;
        for (int c=0; c < cSteps; c++)
        {
         float dValue = 1.0001;
         for (int d=0; d < dSteps; d++)
         {
          float y[256];

                Gamma(fit, cValue, dValue, y);
          float residual = 0;
          for (int i = start; i < stop; i++)
          {
                        float r = CCrspectrum[i] - y[i], rABS = r < 0 ? -r : r;
                         residual += rABS;
          }

          if (residual < fit->r)
          {
           fit->r = residual;
           fit->c = cValue;
           fit->d = dValue;

//          printf("Gamma fit r %f a %f b %f c %f d %f\n",
//                        fit->r, fit->a, fit->b, fit->c, fit->d);
          }

          dValue += dStep;
         }
         cValue += cStep;

//       printf("cValue %f %i\r", cValue, c);
        }
}



void Gamma(peakFit *fit, float cValue, float dValue, float y[256])
{
        float a = fit->a;
        float b = 255 - fit->b;
        float c = cValue;
```

```
        float d = dValue;

        int start = fit->start;
        int stop  = fit->stop;

        // clarity of evaluation
        // p part
        // t term
/*
        for (int x = start; x < stop; x++)
        {
         float p1 = x-b;
         float p2 = d-1;

         double t1 = a*exp(-p1/c);
         double t2 = ((p1 / c) + p2) / p2;

         if (t2 < 0)
          y[x] = 0;

         else
         {
          double t3 = pow(t2, p2);
          y[x] = t1*t3;
         }
*/
        // speed of evaluation
        float p2 = d-1;
        for (int x = start; x < stop; x++)
        {
         float p1 = x-b;
         double t2 = ((p1 / c) + p2) / p2;

         if (t2 < 0)
          y[x] = 0;

         else
         {
          double t1 = a*exp(-p1/c);
          double t3 = pow(t2, p2);
          y[x] = t1*t3;
         }
```

```
        }
}


void GammaF(peakFit *fit, int start, int stop, float y[256])
{
        for (int i=0; i < start; i++)
          y[i] = 0;

        float a = fit->a;
        float b = 255 - fit->b;
        float c = fit->c;
        float d = fit->d;

        // speed of evaluation
        float p2 = d-1;
        for (int x = start; x < stop; x++)
        {
         float p1 = x-b;
         double t2 = ((p1 / c) + p2) / p2;

         if (t2 < 0)
           y[x] = 0;

         else
         {
          double t1 = a*exp(-p1/c);
          double t3 = pow(t2, p2);
          y[x] = t1*t3;
         }

        }}


//*************************************************************************
****
//
//                        Peakfinder
// function will return CHANNEL of 7.68 peak
//
//*************************************************************************
****
```

```
float peakfinder(float spectrum[256])
{
/*
        float sum1=0, peak=169, peak_counts;

        peak_counts =(spectrum[169]+spectrum[168]+spectrum[167]);

        for (int ctr1=175;ctr1>165;ctr1--)
        {
         sum1 = spectrum[ctr1]+spectrum[ctr1-1]+spectrum[ctr1+1];
         if ( sum1 > (peak_counts+10) )
         {
          peak = ctr1;
          peak_counts = sum1;
         }
        }
*/
        int max = 0;
        float channel = 0;
        for (int c=50; c < 256; c++)
        {
         if (spectrum[c] > max)
         {
          max = spectrum[c];
          channel = c;
         }
        }
        return(channel);
}

void straightLine(peakFit *fit,int ROIstart, float data[256], float y[256])
{
float start = fit -> start;
float stop = fit -> stop;

float sumX = 0;
float sumY = 0;
float sumXY= 0;
float sumXX = 0;
float TotalPoints = 0;

        for (int i = start; i <= ROIstart ; i++)
        {
```

```
        sumX += i;
        sumY += data[i];
        sumXY += i*data[i];
        sumXX += i*i;
        TotalPoints++;
        }

        for(i = stop - 10; i < stop; i++)
        {
        sumX += i;
        sumY += data[i];
        sumXY += i*data[i];
        sumXX += i*i;
        TotalPoints++;
        }


float b = (TotalPoints*sumXY-sumX*sumY)/(TotalPoints*sumXX-sumX);

float a = (sumY-b*sumX)/TotalPoints;

for(i = 0 ; i < 256; i++)
 {
        if(i < start || i >= stop) y[i] = 0;
        if( i >=start && i < stop) y[i] = a + b*i;


 }

}

void AddContamination(int start, int stop, float ratio[60], int k)
{

        static int tries[12];

                float counts[12]={

                49.9,     /* Th232 */
                1746.4,         /* U238 */
                1496.9,         /* U235 */
                1496.9,         /* U234 */
                184.6,  /* Np237 */
```

```
                224.5,  /* Pu242 */
                199.6,  /* Pu239 */
                199.6,  /* Am243 */
                249.5,  /* U232 */
                499.0,  /* Th228 */
                199.6,  /* Am241 */
                224.5   /* Pu238 */
                };



        tries[k] = 0;

                int j = 0;
         for(int i=start; i<stop; i++)
         {
         rspectrum[i] += counts[k]*tries[k]*ratio[j];
         j++;
         }
}
```

Appendix C

DAC Factors

DAC Values For Each Radionucldie

Isotope	Energy (MeV)	DAC Factor (Bq/m3)	DAC Factor (mCi/cm3)
232Th	4.01	.02	5.41E-13
238U	4.2	.7	1.89E-11
235U	4.58	.6	1.62E-11
234U	4.77	.6	1.62E-11
237Np	4.77	.074	2.00E-12
242Pu	4.9	.09	2.43E-12
239Pu	5.16	.08	2.16E-12
243Am	5.28	.08	2.16E-12
232U	5.32	.1	2.70E-12
228Th	5.43	.2	5.40E-12
241Am	5.49	.08	2.16E-12
238Pu	5.5	.09	2.43E-12

VITA

David French was born in Knoxville, Tennessee on April 21, 1967. He attended the public school system of Knoxville, Tennessee, where he graduated from Central High School in June, 1985. He entered The University of Tennessee, Knoxville, Tennessee during June of 1985. He graduated from The University of Tennessee in May of 1990 with a degree in Electrical and Computer Engineering. After working for a year and six months, he entered the Master's program in Nuclear Engineering in August of 1992 and received the degree in May of 1995.

He is presently working with the Instrumentation and Controls Division of Oak Ridge National Laboratory. His work in the Instrumentation and Controls Division includes testing of radiation detection instruments and designing circuitry for radiation detection instruments.